

12-2011

## APPLICATIONS OF EPHB4 RECEPTOR SPECIFIC PEPTIDES IN TARGETED CANCER IMAGING AND THERAPY

Miao Huang

Follow this and additional works at: [https://digitalcommons.library.tmc.edu/utgsbs\\_dissertations](https://digitalcommons.library.tmc.edu/utgsbs_dissertations)

 Part of the [Medicine and Health Sciences Commons](#)

---

### Recommended Citation

Huang, Miao, "APPLICATIONS OF EPHB4 RECEPTOR SPECIFIC PEPTIDES IN TARGETED CANCER IMAGING AND THERAPY" (2011). *The University of Texas MD Anderson Cancer Center UTHealth Graduate School of Biomedical Sciences Dissertations and Theses (Open Access)*. 198.  
[https://digitalcommons.library.tmc.edu/utgsbs\\_dissertations/198](https://digitalcommons.library.tmc.edu/utgsbs_dissertations/198)

This Dissertation (PhD) is brought to you for free and open access by the The University of Texas MD Anderson Cancer Center UTHealth Graduate School of Biomedical Sciences at DigitalCommons@TMC. It has been accepted for inclusion in The University of Texas MD Anderson Cancer Center UTHealth Graduate School of Biomedical Sciences Dissertations and Theses (Open Access) by an authorized administrator of DigitalCommons@TMC. For more information, please contact [digitalcommons@library.tmc.edu](mailto:digitalcommons@library.tmc.edu).

APPLICATIONS OF EPHB4 RECEPTOR SPECIFIC PEPTIDES IN TARGETED CANCER  
IMAGING AND THERAPY

by

*Miao Huang M.S.*

APPROVED:

---

Chun Li

---

[Diana Chow]

---

[Zhen Fan]

---

[Dawid Schellingerhout]

---

[Jason Stafford]

---

APPROVED:

---

Dean, The University of Texas  
Graduate School of Biomedical Sciences at Houston

APPLICATIONS OF EPHB4 RECEPTOR SPECIFIC PEPTIDES IN TARGETED CANCER  
IMAGING AND THERAPY

A

DISSERTATION

Presented to the Faculty of  
The University of Texas  
Health Science Center at Houston  
and  
The University of Texas  
M. D. Anderson Cancer Center  
Graduate School of Biomedical Sciences  
in Partial Fulfillment

of the Requirements

for the Degree of

DOCTOR OF PHILOSOPHY

by

*Miao Huang M.S.*

Houston, Texas

*December, 2011*

## ACKNOWLEDGEMENTS

I would like to thank my Ph.D. mentor Dr. Chun Li for giving me the opportunity to study under his supervision and work on the development of EphB4 specific peptide for in vivo imaging EphB4 positive tumors and photothermal therapy of tumors in vivo when conjugated with hollow gold nanoshells. I have successfully finished my Ph.D. project under his guidance and learned many important scientific skills from him, which are very useful for my future career. Thank you very much Dr. Li, I will forever appreciate.

I would also like to show my deep appreciation to Dr. Diana Chow, Dr. Zhen Fan, Dr. Jason Stafford and Dr. Dawid Schellingerhout for suggestions and support on my graduate project in the past five years. I thank Ms. Xiaoxia Wen, Dr. Chiyi Xiong, Dr. Rui zhang, Mr. Qian Huang, Dr. Min Zhou and Dr. Wei Lu for all the assistance in animal and histological studies of my project. Many appreciations go to the special, friendly members of Dr. Li's laboratory including Dr. Marites P Melancon, Dr. Geng Ku, Dr. Jian You, Dr. Jun Zhao, and all former lab members. Thank you for any help you have provided. I would also like to thank all the committee members during my Ph.D. studies.

Finally, I would like to extend my deepest appreciation to my beloved family, my parents and my friends. Thank you very much for your support in my life. Also, I can never fail to thank my wife, Xueqing Wang, for her support all the way through my Ph.D. studies.



## Applications of EphB4 receptor specific peptides in targeted cancer imaging and therapy

Publication No. \_\_\_\_\_

Miao Huang, M.S.

Supervisory Professor: Chun Li, Ph.D.

EphB4 receptors, a member of the largest family of receptor tyrosine kinases, are found over-expressed in a variety of tumors cells including glioma cells as well as angiogenic blood vessels. Noninvasive imaging of EphB4 could potentially increase early detection rates, monitor response to therapy directed against EphB4, and improve patient outcomes. Targeted delivery of EphB4 receptor specific peptide conjugated hollow gold nanoshells (HAuNS) into tumors has great potential in cancer imaging and photothermal therapy. In this study, we developed an EphB4 specific peptide named TNYL-RAW and labeled with radioisotope  $^{64}\text{Cu}$  and Cy5.5 dye. We also conjugate this specific peptide with hollow gold nanoshells (HAuNS) to evaluate targeted photothermal therapy of cancers. In vitro,  $^{64}\text{Cu}$ -DOTA-TNYL- RAW specifically bind to CT26 and PC-3M cells but not to A549 cells. In vivo, Small-animal PET/CT clearly showed the significant uptake of  $^{64}\text{Cu}$ -DOTA-TNYL-RAW in CT26 and PC-3M tumors but not in A549 tumors. Furthermore,  $\mu\text{PET/CT}$  and near-infrared optical imaging clearly showed the uptake of the dual labeled TNYL-RAW peptide in both U251 and U87 tumors in the brains of nude mice. In U251 tumors, Cy5.5-labeled peptide can bind to EphB4-expressing tumor blood vessels and tumors cells. But in U87 models, dual labeled peptide only could bind to tumor associated blood vessels. Also, Irradiation of PC-3M and CT-26 cell treated with TNYL-PEG-HAuNS nanopartilces with near-infrared (NIR)

laser resulted in selective destruction of these cells in vitro. EphB4 targeted TNYL-PEG-HAuNS showed more photothermal killing effect on CT26 tumor model than PEG-HAuNS did. In summary, tumors with overexpression of EphB4 receptors can be noninvasively visualized by micro PET/CT with  $^{64}\text{Cu}$  labeled or dual labeled TNYL-RAW peptide. Targeted delivery of TNYL-RAW conjugated HANs into tumors can greatly improve the treatment effect of photothermal therapy. The information acquired with this study should be advantageous in improving diagnostics and future applications in photothermal ablation therapy in clinical.

## TABLE OF CONTENTS

### PAGE

Approval sheet-----	i
Title Page-----	ii
ACKNOWLEDGEMENTS-----	iii
ABSTRACT -----	iv
TABLE OF CONTENTS -----	vi
FIGURES -----	x
TABLES -----	xiv
INTRODUCTION-----	1
1. Ephrin receptors-----	1
1.1 Ephrin receptor families-----	1
1.2 Biology functions of Ephrin receptor families-----	2
1.3 Develop EphB4 Specific peptides for molecular imaging -----	4
2. Multimodel Imaging-----	6
2.1 Nuclear Imaging -----	6
2.2 Optical Imaging -----	8
2.3 Importance of Multimodal Imaging-----	9
3. Hollow gold nanoshells-----	10
4. Photothermal therapy-----	11
5. Significance-----	13
MATERIALS AND METHODS-----	15
1. Reagents-----	15

2. General Procedures for the peptide synthesis-----	16
3. Synthesis of H AuNS -----	17
4. Conjugation of TNYL-PEG-SATA to H AuNS -----	18
5. Photothermal Effect of different H AuNS solutions -----	19
6. In vitro Photothermal Ablation of Tumor cells -----	19
7. Radiolableing-----	20
8. Immobilization of EphB4 receptor to sensor chip -----	22
9. Surface Plasmon Resonance (SPR) Assay of Receptor Binding Affinity ---	22
10. Stable transfection of Luciferase gene into U251 cells (U251-Luc)-----	23
11. Fluorescence and Darkfield microscopy -----	23
12. Cell binding -----	25
13. Animal Models-----	26
14. Small-Animal PET/CT-----	27
15. Micro-PET imaging -----	29
16. Near Infrared (NIR) Optical Imaging -----	30
17. In Vivo Biodistribution studies-----	30
18. Autoradiography and Optical Imaging -----	32
19. H&E staining and Immunohistochemical Analysis -----	32
20. Photothermal Ablation of Cancer Cells with TNYL-PEG-H AuNS in Vivo-	33
21. Statistical Analysis -----	34
<b>RESULTS</b> -----	35
1. Synthesize and evaluate <sup>64</sup> Cu-labeled TNYL-RAW peptides for PET imaging of EphB4 receptors in prostate and colon cancer xenograft models-----	35

1.1 Chemistry, Radiochemistry, and Stability -----	35
1.2 Binding Affinity of TNYL-RAW and DOTA-TNYL-RAW-DOTA, <sup>Nat</sup> Cu- DOTA-TNYL-RAW and scramble peptides -----	38
1.3 Fluorescence Microscopy-----	41
1.4 In vitro radioisotope binding assay -----	43
1.5 Small animal Micro PET/CT -----	44
1.6 In vivo biodistribution-----	47
1.7 Immunofluorescence study on tumor sections -----	49
2. Evaluate <sup>64</sup> Cu- and Cy5.5-labeled TNYL-RAW peptides for dual PET/optical imaging of EphB4 receptors in orthotopic glioma models-----	50
2.1 synthetic scheme of peptide Cy5.5-TNYL-RAW and Cy5.5-TNYL-RAW- DOTA -----	51
2.2 Binding Affinity of Cy5.5-TNYL-RAW and Cy5.5-TNYL-RAW-DOTA --	52
2.3 Detection of brain tumor growth by luciferase imaging-----	54
2.4 Optical Imaging of U251 and U87 tumors in the brain -----	58
2.5 Ex vivo analysis of the fluorescence signal intensities of dissected tissues -	60
2.6 Nuclear Imaging of tumors in the brain-----	64
2.7 Immunohistochemistry -----	61
3. To develop and evaluate EphB4 specific peptide conjugated H AuNS for photothermal ablation therapy of colon and ovarian cancer in vitro and vivo-- -----	65
3.1 Synthesis and Characterization of TNYL-PEG-H AuNS-----	65
3.2 Fluorescence and dark field microscope-----	67

3.3 In vitro radioisotope binding assay-----	69
3.4 In vitro photothermal ablation of cancer cells -----	70
3.5 Micro-PET Imaging-----	74
3.6 In vivo biodistribution -----	75
3.7 In Vivo Photothermal Therapy -----	76
4. Preliminary study to evaluate EphB4 specific peptide conjugated HAuNS for photothermal ablation therapy of ovarian cancer in vitro and vivo -----	78
4.1 Expression of EphB4 receptors on Hey A8-Luc -----	78
4.2 In vitro photothermal ablation of Hey-A8 cancer cells -----	79
4.3 Detection of Hey-A8 tumor growth by luciferase imaging -----	81
4.4 In vivo biodistribution on intraperitoneal Hey-A8 ovarian tumor model ----	82
4.5 In Vivo Photothermal Therapy-----	83
<b>DISCUSSION</b> -----	85
<b>CONCLUSION</b> -----	99
<b>REFERENCES</b> -----	101
<b>VITA</b> -----	117

FIGURES	PAGE
Figure 1A. Structure of $^{64}\text{Cu}$ -DOTA-TNYL-RAW and $^{\text{nat}}\text{Cu}$ -DOTA-TNYL-RAW peptides -----	36
Figure 1B. Reaction scheme for the synthesis of $^{\text{nat}}\text{Cu}/^{64}\text{Cu}$ -DOTA-TNYL-RAW -----	36
Figure 1C. Electrospray ionization mass spectrometry spectrum of $^{\text{nat}}\text{Cu}$ -DOTA-TNYL-RAW-----	37
Figure 1D. Radio-HPLC chromatogram of $^{64}\text{Cu}$ -DOTA-TNYL-RAW and $^{\text{nat}}\text{Cu}$ -DOTA-TNYL-RAW -----	38
Figure 2A. Sensogram of successful coating of EphB4 receptor on CM-5 sensor chip--	39
Figure 2B. Mechanism of coupling of EphB4 ligand to the surface of CM5 sensor chip-----	39
Figure 2C. SPR sensorgrams of TNYL-RAW and DOTA-TNYL-RAW-DOTA, $^{\text{Nat}}\text{Cu}$ -DOTA-TNYL-RAW and scramble peptides -----	40
Figure 3A. The structure details of FITC-TNYL-RAW-----	42
Figure 3B. Fluorescence photomicrographs of PC-3M cells treated with FITC-TNYL-RAW or scrambled peptide FITC-sc-TNYL-RAW and blocking study-----	42
Figure 4A. Uptake of $^{64}\text{Cu}$ -DOTA-TNYL-RAW in EphB4-positive PC-3M cells -----	43
Figure 4B. Uptake of $^{64}\text{Cu}$ -DOTA-TNYL-RAW in EphB4-positive CT-26 cell-----	44
Figure 5A. Representative small-animal PET/CT images of mice bearing CT26, PC-3M, and A549 tumors after tail vein injection of $^{64}\text{Cu}$ -DOTA-TNYL-RAW ----	46
Figure 5B. Representative micro PET/CT images showing blocking of $^{64}\text{Cu}$ -DOTA-TNYL-RAW uptake in CT26 tumors at 4 h and in PC-3M tumors at 24 h after co injection of $^{64}\text{Cu}$ -DOTA-TNYL-RAW with cold TNYL-RAW ----	47

Figure 6A. Biodistribution of $^{64}\text{Cu}$ -DOTA-TNYL-RAW in mice bearing PC-3M and A549 tumors at 24 h after injection -----	48
Figure 6B. Biodistribution of $^{64}\text{Cu}$ -DOTA-TNYL-RAW in mice bearing CT-26 tumors at 4 h after injection -----	49
Figure 6C. Tumor-to-muscle-uptake ratio in mice bearing CT-26 or PC-3M tumors (blocking study) -----	49
Figure 7. Immunofluorescence analysis of EphB4 expression in CT26, PC-3M, and A549 tumor sections excised after the imaging studies -----	50
Figure 8A. Synthetic scheme of peptide Cy5.5-TNYL-RAW and Cy5.5-TNYL-RAW-DOTA-----	50
Figure 8B. Structure details of Cy5.5-TNYL-RAW-----	52
Figure 8C. Structure details of and Cy5.5-TNYL-RAWK-DOTA-----	52
Figure 9. SPR sensorgrams of DOTA-TNYL-RAW, Cy5.5-TNYL-RAW, Cy5.5-TNYL-RAW-DOTA and Cy5.5-scrambled peptide -----	53
Figure 10. Representative Lucifase images of U251 and U87 glioblastoma on orthotopic mice -----	55
Figure 11A. Representative Cy5.5 optical images of U251 and U87 glioblastoma on orthotopic mice -----	56
Figure 11B. Representative near-infrared (NIR) fluorescence optical images of U87 after tail vein injection of Cy5.5-TNYLRAW-DOTA or Cy5.5-scramble -----	57
Figure 12A. Representative near-infrared (NIR) fluorescence optical images of various tissues obtained from the mouse at the end of the imaging sessions -----	59



Figure 12B. Biodistribution at 24h after i.v. injection of different peptides, obtained using the fluorescence intensity measurement method -----	60
Figure 13A. Micro PET/CT images of mice bearing a U87 after intravenous administration of $^{64}\text{Cu}$ -labeled Cy5.5-TNYL-RAW-DOTA -----	61
Figure 13B. Micro PET/CT images of mice bearing a U251 after intravenous administration of $^{64}\text{Cu}$ -labeled Cy5.5-TNYL-RAW-DOTA -----	62
Figure 13C. Compared tumor voxel intensity / normal brain voxel intensity between $^{64}\text{Cu}$ -labeled Cy5.5-TNYL-RAW-DOTA and blocking group -----	63
Figure 13D. Representative autoradiograph, fluorescence and H&E staining images of same excised brain tissue containing U251 tumors -----	64
Figure 14. Fluorescence microscopy of mice brains including implanted U87 or U251 tumors excised after imaging studies -----	65
Figure 15A. Structure details of TNYL-PEG-SATA-----	66
Figure 16B Reaction scheme for the conjugation of TNYL-PEG-SATA to H AuNS ---	66
Figure 15B. The resonance absorbance of these different H AuNS particles -----	67
Figure 16. Fluorescence microphotographs (dark field) and radioactive uptake study of EphB4-positive PC-3M and CT-26 cancer cells after incubation with TNYL-PEG-H AuNS or PEG-H AuNS -----	68
Figure 17. Radioactive uptake study of cells incubated with $^{64}\text{Cu}$ labeled TNYL-PEG-H AuNS or PEG-H AuNS-----	69
Figure 18. Heating of aqueous TNYL-PEG-H AuNS, PEG-H AuNS or H AuNS solutions exposed to NIR light-----	71
Figure 19. CT-26 cells viability after various treatments-----	72

Figure 20. PC-3M cells viability after various treatments-----	73
Figure 21. Micro PET imaging of mice bearing a CT-26 tumor after intravenous injection of $^{64}\text{Cu}$ labeled TNYL-PEG-HAuNS or TNYL-HAuNS-----	74
Figure 22. In vivo biodistribution and tumor uptake of $^{64}\text{Cu}$ labeled TNYL-PEG-HAuNS or PEG-HAuNS in mice bearing a CT-26 tumor-----	75
Figure 23. Representative microphotographs of tumors removed 24 h after NIR laser treatment-----	77
Figure 24. Bar graph of the necrotic area as a percentage of the tumor-----	78
Figure 25. Fluorescence photomicrographs of HeyA8-Luc cells-----	79
Figure 26. Hey A8-Luc cells viability after various treatments-----	80
Figure 27. Representative Lucifase images of Hey-A8 tumor on intraperitoneal nude mice model -----	81
Figure 28. In vivo biodistribution and tumor uptake of $^{64}\text{Cu}$ labeled TNYL-PEG-HAuNS or PEG-HAuNS in mice bearing Hey-A8-Luc (intraperitoneal) tumor-----	82
Figure 29. Representative microphotographs of tumor and intestine removed 24 h after NIR laser treatment-----	83

<b>TABLES</b>	<b>PAGE</b>
Table 1. Association, Dissociation Rates and $K_D$ of different TNYL-RAW peptides and derivatives -----	41
Table 2. Summary of summary of the different uptake of $^{64}\text{Cu}$ -DOTA-TNYL-RAW in CT26, PC-3M and A549 tumors at different time points-----	47
Table 3. Association, Dissociation Rates and $K_D$ of different TNYL-RAW peptides and derivatives -----	54

## **INTRODUCTION**

### **1. Ephrin receptors**

#### **1.1 Ephrin receptor families**

A tyrosine kinase (erythropoietin-producing human hepatocellular carcinoma receptor, Eph receptor) was first discovered by Hirai *et al* (Science) in 1987. In a screening for novel oncogenic tyrosine kinase, Hirai cloned a new gene from a carcinoma cell line that was named EphA1 later. They also found that this novel receptor tyrosine kinase is up-regulated in tumor versus normal tissues. Ectopic overexpression this kinase can cause the oncogenic transformation of NIH3T3 fibroblasts (1, 2), which suggested the oncogenic function of Eph gene. Later, the corresponding ligand (ephrin A1) of Eph A1 receptor was also identified from cancer cell lines. Eph receptors comprise the largest family of vertebrate receptor tyrosine kinases (3). It is now known that there are 9 Eph A and 5 Eph B receptors which promiscuously bind to 5 glycosylphosphatidylinositol (GPI)-linked ephrin-A ligands and GPI-linked 3 ephrin-B ligands respectively (4). But Eph A4 and Eph B2 receptors can also bind to ephrin-B or ephrin A5 ligands respectively. EphB4 receptor preferentially binds to ephrin B2 ligand.

The signal transduction between Ephrin receptors and ephrin ligands is bidirectional. Tyrosine kinase activity determined forwarding signal is amplified and propagated in the receptor expressing cells and Src family kinase determined reversed signal is propagated in ephrin ligand expressing cells. However, the ephrin ligand-dependent but tyrosine kinase independent signaling pathway can also be found at some conditions (5-7). The activation of most receptor tyrosine kinases depends on the dimerization of receptors once ligand-receptor complex formed. But the activation of Ephrin receptor-ephrin

ligand complex is different from the classic activation way of receptor tyrosine kinases (8). Multimerization of ephrin ligand molecules on cellular membranes plays an important role in Ephrin/Eph function (9, 10). The signaling pathway of Eph/ephrin complex is well understood in the development process of nervous system such as in axon plasticity and patterning, which can be explained by repulsive mechanism. The Ephrin receptor expressed axons can migrate away from cells that express ephrin ligand based on this repulsive mechanism (10). There are lots of signal transduction pathways and downstream molecules involved in the Eph/ephrin receptor signaling axis, such as JAK/ STAT (11) and AKT/PI3K pathways (12).

## **1.2 Biology functions of Ephrin receptor families**

Ephrin receptors play an important role in numbers of biological processes in normal development such as axon guidance, cell migration, cell morphology, cell adhesion, invasion, angiogenesis and limb development (13, 14). The signal through Eph receptors can influence the cell migration, adhesion and invasion by modifying the structures of actin cytoskeleton and affecting the activities of intercellular adhesion molecules and integrins (4, 15). Eph receptors are also involved in some specialized cell function such as insulin secretion, immune function and bone remodeling (15).

A lot of evidence has been accumulated to demonstrate that Eph/ephrin axis plays significant roles in the development of vasculature. The distinct expression pattern of Eph B4 receptor and its ligand ephrin B2 on arterial and venous endothelial cells suggest that developing capillary networks may not be uniform structures (16). The essential requirement for tumor growth and survival is the formation of new blood vessels and capillaries from pre-existing vasculature networks (angiogenesis). Studies have implied

that up-regulation and dysregulation of Eph/ephrin axis signaling pathway involved in the new blood vessels formation during the process of the tumor invasion (1, 17, 18)

Lots of studies have shown that the expression level of Ephrin receptors and ephrin ligands is correlated with the cancer progression, invasion, metastasis and the survival rate of patients (17-27). For example, EphA2 receptor has been found overexpressed in numbers of cancers and its expression level is correlated with the progression of cancer and poor prognosis of cancer patients (17-21). Also, among all the cancer types, the expression of EphA2 receptor is preferable in the breast and prostate cancers with a basal phenotype (22, 23). Studies have shown that up-regulation of Eph A2, A7, A10 and ligands such as ephrin A2 and B3 is involved in the breast cancer invasion and metastasis (24). Up-regulated expression level of Eph receptors and their ephrin ligands is correlated with the progression of malignant melanoma (25) Eph A1 not only can promote the proliferation of melanoma cancer cells and enhance the cancer cell growth, it also can increase the angiogenesis in advanced melanomas (26). Ectopic overexpression of Eph A2 can promote progression of benign prostatic epithelial cells into more aggressive phenotype (27).

EphB4 receptors play important roles in a variety of biologic processes, including cell aggregation and migration, neural development, embryogenesis and angiogenesis, and limb development (13, 28-31). Overexpression of EphB4 receptor, an important member of Ephrin family, has been observed in numerous tumor types, including breast prostate, bladder, lung, colon, ovarian, and gastric cancers (4, 32-36). Endogenous ligand, ephrin-B2, can specifically bind to its corresponding receptor EphB4 to promote progression and metastasis of various cancers and induce angiogenesis in more advanced

cancers. The effect of promotion of tumorigenesis and angiogenesis is mediated through the signaling interaction between EphB4 and ephrin B2 ligand. It is interesting to notice that some forwarding EphB4 signaling pathway may exhibit the inhibit effect on tumor cell proliferation.(37) Xia *et al.* demonstrated that EphB4 is up-regulated in prostate cancer cells and the induction of expression of EphB4 in prostate tumors may undergo the transcriptional regulatory effect of pro-survival signaling molecules or through the amplification of gene encode EphB4 receptor (38). Furthermore, inhibition of expression and oncogenic activity of EphB4 can reduce the survival, migration and invasion of prostate cancer cells. Another paper also showed that increased EphB4 activity and expression in prostate cancer patients are correlated with the higher grade disease which suggested that the expression level of EpHB4 indicate the malignancy of the disease (39). In colon cancer, increased expression of the EphB4 gene has been found to play an important role in the development of unique tumor phenotype (40). It has been also found that EphB4 receptors are expressed at high levels in both tumor cells and blood vessels in high-grade gliomas (41).

### **1.3 Develop EphB4 Specific peptides for molecular imaging**

As above mentioned, EphB4 is overexpressed in various cancer types including prostate, colon and brain tumors (38-41). So it is intriguing to develop a new molecular imaging probes targeted for EphB4 receptors. But up to now, there is no peptide based imaging probes being developed to detect EphB4 receptors in different tumors.

The most important thing for molecular imaging is to find a proper molecular target to differentiate tumors from normal tissues. There are lots of pathologically abnormal processes in cancer that allow us to make molecular imaging probes to target these

processes for *in vivo* detection and functional characterization of tumors. Over the past years, a lot of radiolabeled peptides used as nuclear imaging agents have been developed for *in vivo* visualization of solid tumors with overexpressed receptors. For example, radiolabeled neuropeptide receptors ligands are suitable molecular targeting probes for *in vivo* visualization of tumors with overexpression of corresponding receptors by positron emission tomography (PET) or single photon emission computed tomography (SPECT) (42,43). In clinic, small radiolabeled somatostatin peptidyl analogs (molecular weight ~1.5 kDa) have been successfully developed for detection and visualization of neuroendocrine tumors with overexpression of somatostatin receptors (42, 43). Currently, cyclic Arg-Gly-Asp peptide which binds to integrin  $\alpha_v\beta_3$  receptors used for nuclear imaging is under clinical investigation (44). Lots of other peptide-based imaging agents, such as substance P (45), melanocyte-stimulating hormone analog (46), calcitonin (47), atrial natriuretic peptide (48), bombesin/gastrin-releasing peptide, cholecystokinin, glucagonlike peptide-1, and neuropeptide-Y, have also been identified and developed for *in vivo* molecular imaging of solid tumors (49). But very few peptides have been characterized for noninvasive detection and imaging of prostate cancer, colon cancer and gliomas (49).

Using phage display approach, several 12-mer peptides which specifically bind to corresponding Ephrin receptors have been identified by Koolpe *et al* in 2005 (50). Among those peptides, an Ephrin B4 receptor specific peptide (Thr-Asn-Tyr-Leu-Phe-Ser-Pro-Asn-Gly-Pro-Ile-Ala, TNYL peptide) has been identified from initial screening. To optimize this TNYL peptide, the original TNYL peptide has been modified by adding a tripeptide moiety (RAW) at the carboxyl terminus based on the information from the



sequence alignment. The final product, Thr-Asn-Tyr-Leu-Phe-Ser-Pro-Asn-Gly-Pro-Ile-Ala-Arg-Ala-Trp (TNYLFSPNGPIARAW, TNYL-RAW) was shown to be a strong antagonist of EphB4 receptor. This modified peptide inhibited binding of ephrin B2, a natural EphB4 binding ligand, to immobilized Eph4 receptor with  $IC_{50}$  around 15 nM compared with 150  $\mu$ M for TNYL peptide (50). In Koolpe's study, the biotinylated TNYL peptide was conjugated to streptavidin-coated quantum dots nanoparticles Qdot 655 quantum dots (Quantum Dot Corp.) to confirm the targeting effect of this peptide. From his study, it has clearly showed that this TNYL conjugated quantum dots can specifically bind to COS cells with ectopic expression of Eph B4 receptors or cells with endogenous expression of EphB4 (50). Because TNYL-RAW peptide has extremely high binding affinity for EphB4 receptors, we tried to investigate whether this peptide can be used as molecular imaging agents to noninvasively detect and visualize up-regulated EphB4 receptors in various tumor models. Furthermore, we conjugated this peptide to hollow gold nanoshells (HAuNS) to study the effect of photothermal therapy on colon and ovarian cancer model

## **2 Multimodal Imaging**

### **2.1 Nuclear Imaging**

The first time using of radioactive tracers in the living system was to study the transport of radioactive lead in plants was done by Hevesy and Paneth in 1923. In 1935, Hevesy and Chiewitz used radiotracer (P-32) to study the distribution of radioactive P-32 in rats. Later, Anger invented the first scintigraphic imaging instrument named gamma camera in 1956. At the same time, positron imaging was developed too. Now, both imaging modalities become standard methods in nuclear medicine field. The most

radioisotopes used in the clinical settings are  $^{99m}\text{Tc}$  in single photon imaging (SPCET) and  $^{18}\text{F}$  in positron imaging (PET). Now, PET and SPECT techniques have become the standard imaging diagnosis processes for the patients with different diseases. The underlying mechanism in nuclear medicine is to use the radiotracers to detect the metabolism, biochemical, physiological and pathophysiology process in patients. These two imaging modalities can be used alone or combined together to study various biological activities in human body such as metabolite rate, binding capacity and transport rate. Also they can be used to monitor and detect the expression of enzymes, receptors, and transporter as well as their corresponding endogenous analogue such as ions, hormones, and enzyme substrates (51-53). Compared with other imaging modalities, nuclear imaging has more advantages, such as more sensitive, deep penetration into the tissues, and quantitative analysis and process of the image data. But there is no perfect single imaging technique. Nuclear imaging can detect abnormal physiology, biochemical or metabolic changes in patients but they may provide less accurate location and anatomy structure of the human body due to the weak spatial resolution of nuclear imaging. To provide more accurate anatomy location and structure information of the patients, multimodality imaging devices such as PET/CT, SPECT/CT, and PET/MRI are developed and become more popular in clinical practice. These combinations of imaging techniques can provide precise 3-dimensional images of biological and anatomical information in patients. Nuclear imaging may require long acquisition time of imaging due to the low photon counts. Also, it doesn't provide sufficient resolution details in real time because of the short and finite half-life of the radiotracer used (54, 55). Then optical imaging can be an alternative imaging technique.

## 2.2 Optical Imaging

Optical imaging is a rapidly developing field and attracts lot of interest recently. Biomedical optical imaging techniques can be used in various clinical diagnosis and molecular biology and substantially affect the outcomes of treatment and prevention of cancer (56). Optical imaging techniques such as fluorescence and bioluminescence molecular imaging have lots of advantages compared with traditional imaging techniques. First, they can provide high spatial resolution images to reflect both functional and structural changes at nano or even femtomolar sensitivity (57). Secondly, these techniques are non-invasive, non-radiation, portable and low cost. Third, the results of optical imaging can be obtained almost in real time. Fourth, these techniques can provide valuable information in both microscopic and macroscopic scales and widely applied in almost all biomedical fields. Last but not the least, quantitative analysis of optical imaging results can be useful for objective diagnosis and patient follow-up.(58-63). Furthermore, these techniques have already been tested in various initial clinical situations. For example, it is promising to use hemoglobin and deoxyhemoglobin as a biomarker to monitor effective neo-adjuvant chemotherapy in breast cancer patients by diffuse optical spectroscopy (64, 65).

The major limitations of further application of optical imaging techniques in clinical settings are the penetration depth due to the strong scattering of optical radiation in tissues and strong auto-fluorescence due to the absorbance of the photons by the thick and opaque tissues. The acquired signal can be obscured by above reasons. However, recent progress in NIR (near infrared region, 650-900 nm) optical techniques exhibits promising *in vivo* application of optical imaging techniques. First, the detection depth of

NIR has been pushed to a few centimeters. Second, NIR molecular imaging technique shows lower light absorbance and reduced auto-fluorescence of normal tissues, which makes it more suitable for *in vivo* application (66-70). In our studies, we labeled our EphB4 specific peptide TNYL-RAW with NIR fluorophores (Cyanine 5.5 also called Cy5.5) for *in vivo* optical molecular imaging in glioblastoma orthotopic nude mice models. Cy5.5 is a fluorescent dye emitting photons in the NIR spectrum and one of the members of synthetic cyanine dye family. This dye is water-soluble, and has an absorbance maximum of 675 nm and an emission maximum of 694 nm.

### **2.3 Importance of Multimodal Imaging**

Today, various imaging techniques are available for differential diagnosis and evaluation of severity of diseases as well as monitoring the therapeutic response of the patients to medical treatments. Among all of these imaging modalities, such as positron emission tomography (PET), single photon emission computed tomography (SPECT), optical imaging, computed tomography (CT), ultrasound (71) and magnetic resonance imaging (MRI), none of them can be used alone to provide sufficient comprehensive information necessary for the diagnosis of various disease of patients. Multimodality imaging can provide structure and functional information of the disease by two ways. One is that images are acquired at different times and then different images are fused together by digital imaging processing technique (asynchronous way). Another way (synchronous way) is that images are acquired simultaneously and merged automatically. It is difficult to fuse images using asynchronous way due to the two different scans acquired at separated machines. The best solution to solve the inconsistency of the space and time is achieved by using synchronous image acquisition.

Currently, lots of multimodality techniques (SPECT/CT, PET/CT, and PET/MR) are available in diagnostic imaging fields. The most common techniques among these are combinations of high detection sensitivity techniques such as PET and SPECT with CT, MRI, and ultrasound that have high spatial resolution. The first prototype of CT-SPECT thoracic images of patients was obtained in 1962 (45). Since the commercial introduction of SPECT/CT and PET/CT in 1998, the development and use of these instruments grows exponentially. Up to now, there are almost no sales of standalone PET machines and all PET sales are as part of multimodality systems (72).

As we all known, no single imaging modality is perfect. In current study we combined the optical imaging technique, one of the most widely used imaging techniques in preclinical molecular imaging with nuclear imaging PET/CT, which is the most effective clinical imaging modality.

### **3 Hollow gold nanoshell**

Optical phenomenon named surface plasmon resonance (SPR) is an important characteristic of Au and silver (Ag) containing nanostructures. When these nanomaterials are exposed to light, the conduction-band electrons in the metal containing nanostructures will collectively oscillate at a resonance frequency relative to the lattice of positive ions. Then the nanostructures will absorb the incident light at this resonance frequency. The resonance of the solid spherical nanoparticles is about at 400 nm for Ag and around 520 nm for Au. The variable peak wavelength of absorbance relatively depends on the size or the embedding medium of the nanoparticles. We can tune the peak wavelength of SPR from visible to near infrared (NIR) region by changing the size, shape, and structure of the nanoparticles. The novel Au containing

nanoparticles termed hollow gold nanospheres (HAuNS) have the unique characteristics such as small size (30-60 nm), spherical shape, hollow interior, and strong and tunable (520-950 nm) absorption band at NIR region (73, 74).

Using cobalt (Co) NPs as sacrificial templates to synthesize of HAuNSs with tunable interior cavity sizes was first reported by Liang's group (75). Due to the higher reduction potential of the  $\text{AuCl}_4^-/\text{Au}$  redox pair (0.935 V vs the standard hydrogen electrode [SHE]) compared with that of the  $\text{Co}^{2+}/\text{Co}$  redox couple (-0.377 V vs SHE), the  $\text{Au}^{3+}\text{Cl}_4^-$  can be easily reduced to Au (0) atoms once the Co nanoparticles are added into chloroauric acid solution. The reaction equation is as this:  $3\text{Co} + 2\text{AuCl}_4^- = 2\text{Au} + 3\text{Co}^{2+} + 8\text{Cl}^-$ . The size of the final HAuNS product is controlled by the initial size of the Co nanoparticles template because the reduced Au atoms are mostly confined to the vicinity of the outer surface of the Co template. The stability of HAuNS is maintained by coating polyethylene glycol (PEG) on the surface of the shells. Coating HAuNS with higher molecular-weight (5kDa) makes HAuNS much more stable than coating with lower molecular weight (2kDa) PEG does. Also HAuNS coated with thioctic-acid-anchored PEG containing two thiol groups are more stable in aqueous solution than HAuNS coated with monothiol-anchored PEG.

#### **4 Photothermal therapy**

Photothermal therapy is a therapeutic method in which photothermal agent is introduced to produce heat after the laser energy delivered to the targeted tumors. The heat produced by this photothermal effect is far beyond the threshold temperature (~330K) which can cause irreversible cell death and kill the tumor cells (76). This therapy modality has attracted a lot of attentions recently because it has lots of advantages over the traditional cancer therapies such as fewer side effect, less

accumulated toxic effect with repeatedly laser treatments and boosted efficacy of the chemotherapy and radiotherapy when combined with photothermal therapy (76-79). Nanoparticles with unique optical properties such as gold nanoshells, nanorods, nanocages, and hollow nanospheres (80-86) can significantly enhance the efficiency of photothermal therapy by integrating these light-absorbing materials into the target tissue to mediate the selective photothermal effects. H AuNS have the unique characteristics such as small size (30-60 nm), spherical shape, hollow interior, and strong and tunable (520-950 nm) absorption band (73, 74), which have the great opportunity to convert optical energy into thermal energy for thermal ablation of tumor cells. It is possible to deliver thermal energy to the deeper tissue because the SPR absorption peak of H AuNS is the easily tunable in the NIR region. Due to the convenient modification of the surface of the H AuNS, specific molecular targeting molecules with SH-terminal can be easily conjugated to the Au surface of H AuNSs through covalent bonds. Lots of different specific targeting molecules such as antibodies, peptides, and low molecular-weight compounds have been conjugated to the surface of the H AuNS (73, 87). After modification with the specific homing molecules, the H AuNS can be used in targeting photothermal therapies *in vitro* and *in vivo*. Loo *et al.* (84) and Lowery (88) demonstrated targeted photothermal killing of human breast cancer cells *in vitro* when irradiated with an NIR laser (820 nm) at 35 W/cm<sup>2</sup> for 7 min but no effect on the dermal fibroblast which don't overexpress HER2 receptors on their surface by using HER2 (human epidermal growth factor receptor 2) specific antibody conjugated nanoshells (89). It is well known that one of the most important factors for the cellular uptake of nanoparticles is the size of the nanostructures. Nanoparticles larger than 100 nm are

difficult for uptake into the cells and may interfere with the normal function of the cells. The small particle size (smaller than 20 nm) may be difficult for cells to retain the nanoparticles. For *in vivo* targeting of nanoparticles into tumor tissues, the particle size is also a critical factor. It was demonstrated that the smaller size of gold nanoparticles (20-40nm) coated with PEG has longer blood circulation time than larger gold nanoparticles (80 nm). Also with the smaller size, gold nanoparticles has better chance of extravasating from tumor-associated blood vessel into the extra-vascular fluid space and passively diffused into the tumor tissues. Taken together, the idea size of the particle for photothermal therapy *in vitro* and *vivo* is between 20 nm and 80 nm. The size of the HAuNS we used in this study is around 40 nm. Previous study in our lab demonstrated the selective killing EGFR over-expression of cancer cells A431 *in vitro* by introducing C225 antibody (targeting EGF receptors) conjugated HAuNS into the tumor cells (73). This killing effect is mediated through EGFR demonstrated by blocking or non-conjugated PEG coated HAuNS control studies. Wei *et al.* (85) conjugated HAuNS with a small molecular-weight peptide, [Nle<sup>4</sup>, D-Phe<sup>7</sup>]  $\alpha$ -melanocyte-stimulating hormone (NDP-MSH) for successfully targeted photothermal therapy of melanoma *in vitro* and *vivo* studies. Our lab previously reported using EphB4 receptor specific TNYL-RAW peptide or peptide conjugated polymeric micellar nanoparticles to detect of EphB4 expression in cancer (90, 91). Therefore, targeting of EphB4 has great potential in cancer imaging and therapy.



## Specific Aims and Significance

Early detection of cancer and monitoring the treatment response of cancer patients by molecular imaging methods are important components of the differential diagnosis of cancer patients and prediction of prognosis of patients. It is desirable to have an imaging method to accurately detect and monitor EphB4 status in cancer patients. Photothermal therapy is a novel cancer treatment strategy that kills cancer cells by producing heat after the laser energy delivered to the targeted tumors. Introduction of H AuNS into local tumor tissues can enhance the photothermal therapy effect. EphB4 is a good targeting molecule for specific delivery of H AuNS to tumor tissues.

Therefore, the major purpose in my study is: first, to develop a novel targeting peptide molecules dual-labeled by Cy5.5 optical dyes and  $^{64}\text{Cu}$  nuclear isotopes for early detection of tumors with the overexpression of Eph B4 receptors *in vivo*; Second, synthesis and evaluation of photothermal killing effect of EphB4 specific peptide conjugated H AuNS on the tumor cells *in vitro and vivo*. Using this novel imaging agent, it allows us to do whole-body scan to visualize and locate tumor by nuclear imaging (PET/CT) and followed by fluorescence imaging guided biopsies to define precisely extent and region of local tumors. It is first time here to show that EphB4-specific peptide could be used as a non-invasive molecular imaging agent for PET/CT or/and optical imaging of tumors owing to its ability to bind to EphB4-expressing angiogenic blood vessels and or to EphB4-expressing tumors. We believe that translation of this discovery from basic science to clinical situation may improve the differential diagnosis of cancer patients and affect the outcome of the prognosis of the patients. Conjugation of EphB4 specific peptide onto the H AuNS can enhance the delivery H AuNS to local

tumor tissues with overexpression of Eph B4 and mediate specific killing effects on tumor cells by photothermal therapy. We hope that our nanoparticles which conjugated specific homing molecules can combine imaging and therapeutic functions together for cancer diagnosis and treatments in future clinical medicine.

## **MATERIALS AND METHODS**

### **1. Reagents**

All amino acid derivatives and coupling reagents were purchased from Novabiochem (San Diego, CA), Bachem (Torrance, CA), and Chem-Impex International (Wood Dale, IL). All other chemicals were purchased from Sigma-Aldrich (St. Louis, MO). DOTA-TA was synthesized in our lab.  $^{64}\text{CuCl}_2$  solution was bought from University of Wisconsin (Madison, WI). PC-3M cells were gift from Dr. Fiedler (UT MD Anderson Cancer Center, TX). CT-26 and A549 cells were purchased from American Type Culture Collection (Manassas, VA). U87 cells stably transfected with the luciferase gene (U87-Luc) were gift from Dr. Gelovani (UT MD Anderson Cancer Center, TX). U251 cells were gift from Dr. Shuyun Huang (UT MD Anderson Cancer Center, TX). Hey A8 stably transfected with the luciferase gene (HEY A8-Luc) were gift from Dr. Anil Sood (UT MD Anderson Cancer Center, TX). RPMI-1640, DMEM/F12 and MEM medium were obtained from Gibco (Carlsbad, CA). Calcein AM, Eth-D1 and DAPI were purchased from Invitrogen (Carlsbad, CA). PD-10 columns were purchased from Amersham-Pharmacia Biotech (Piscataway, NJ). Protein assay kit was purchased from Bio-rad (Hercules, CA) D-Luciferin was purchased from Biosynth Chemistry & Biology (Staad, Switzerland). Rat anti-mouse CD31 antibody was purchased from Millipore (Billerica, MA). Recombinant EphB4/Fc chimera, phycoerythrin-conjugated rat

antihuman EphB4 monoclonal antibody, and rabbit anti-EphB4 antibody were purchased from Santa Cruz Biotechnology (Santa Cruz, CA). Goat anti-rabbit antibody conjugated with near-infrared dye was purchased from Li-COR. DOTA was obtained from Macrocyclics. The Biacore sensor chip CM5, amine coupling kit, HBSEP running buffer (0.01 M 4-(2-hydroxyethyl)-1-piperazineethanesulfonic acid [HEPES], pH 7.4; 0.15 M NaCl; 3 mM ethylenediaminetetraacetic acid [EDTA]; and 0.005% [v/v] surfactant P20 solution), and regeneration buffer were purchased from Biacore, Inc.

## **2. General Procedures for the peptide synthesis**

Solid phase syntheses of peptide were performed on the automatic peptide synthesizer Prelude (PTI, Tucson, AZ) using Rink resin (Novabiochem).  $5 \times 1.5$  mL of dimethylformamide (DMF)/methylene chloride ( $\text{CH}_2\text{Cl}_2$ ) was used to wash the resin (0.05 – 0.1 g).  $3 \times 1.5$  mL of 20% piperidine/DMF was used to remove fluorenylmethyloxycarbonyl (Fmoc) groups for 5 min each. Three-fold excesses of Fmoc-amino acids, diisopropylcarbodiimide (DIC), and HOBt (1-hydroxybenzotriazole) were used in 3 mL of DMF/ $\text{CH}_2\text{Cl}_2$  for coupling procedure. This procedure was repeated once. Resins were washed with  $3 \times 3$  mL of DMF/ $\text{CH}_2\text{Cl}_2$  after coupling and deprotection steps. Resins were washed with  $3 \times 3$  mL of  $\text{CH}_2\text{Cl}_2$  and treated with trifluoroacetic acid (TFA): triisopropylsilane:  $\text{H}_2\text{O}$  (95:2.5:2.5) for 15 min each once the procedure of peptide chain elongation was finished. The combined filtrates sat at room temperature for 1-2 hr, and the volumes were reduced in a vacuum. Peptides were precipitated in ice-cold ethyl ether, washed 2 times with ethyl ether and collected by centrifugation. After drying, peptides were purified by reverse-phase high-performance

liquid chromatography (RP-HPLC) on an Agilent 1200 system (C-18, Vydac, 10 × 250 mm, 10 μm; Santa Clara, CA).

Solution phase reaction was used to synthesize DOTA and fluorescein isothiocyanate (FITC)-coupled TNYL-RAW (Figure 3A) peptides followed by HPLC purification. For conjugation of Cy5.5 or/and DOTA to TNYL-RAW peptides, a solution of Cy5.5-NHS (1eq) and peptide TNYL-RAW or DOTA-NHS (1eq) and peptide TNYL-RAWK (Figure 8A) in dimethylformamide and DIPEA (10/1) were stirred at room temperature overnight. A lysine group was introduced to the peptide sequence before simultaneous conjugation of Cy5.5 and DOTA to the peptide due to the C-terminal amide group in original peptide sequence. Before introduction of lysine group, a glycine linker amino acid was added at c-terminal to minimize the effect on binding affinity of peptide after modification of sequence. After the solvent was removed under vacuum, the residual was purified by reverse-phase HPLC, eluted with a 0.01-M solution of NH<sub>4</sub>OAc in water and acetonitrile, and lyophilized. The peptides were identified by high-resolution electrospray ionization mass spectrometry (HRMS-ESI) spectra acquired in the positive ion mode. This was done on an Agilent 1100 Series LC/MSD TOF instrument equipped with a Vydac C18 column (4.6 x 250 mm, 7 μm, 300 Å) (Anaheim). For synthesis of PEG-TNYL-SATA (Figure 15A) peptide, the peptide and heterodifunctional poly (ethylene glycol) (PEG) precursor, *N*-hydroxysuccinimidyl-PEG-*S*-acetylthioacetate (NHS-PEG-SATA; molecular weight 5,000, figure 15A) was conjugated together, through peptide's α-amine group of threonine residue and activated ester in NHS-PEG-SATA. The sulfhydryl group on the other terminus of TNYL-PEG-SATA was released by treatment with 0.05 M hydroxylamine in PBS.

### **3. Synthesis of HAuNS**

HAuNS were synthesized according to the method of Schwartzberg et al. with minor modifications (70). Briefly, 2500  $\mu$ L of sodium borohydride (1 M) was added into 1000 mL of deoxygenated aqueous solution of sodium citrate (2.8 mM) and cobalt chloride (0.4 mM) to synthesize cobalt template nanoparticles. The clear and slightly pink solution turned brown after adding sodium borohydride, which indicated reduction of Co (II) and the formation of cobalt nanoparticles. The solution was left to stay at room temperature for 45 min under constant gas flow of argon until complete hydrolysis of the sodium borohydride. In a different vial, bubbling with argon gas was used to deoxygenate 600 mL chloroauric acid (0.04 mM) solution. Then, 800 mL of cobalt nanoparticle solution was transferred to the chloroauric acid solution under argon protection and magnetic stirring. Gold ions were immediately reduced by cobalt onto the surface of cobalt nanoparticles while at mean time cobalt was oxidized to cobalt oxide. Any remaining cobalt core was further oxidized by air, resulting in the final formation of HAuNS.

### **4. Conjugation of TNYL-PEG-SATA to HAuNS**

The reaction scheme of conjugation of TNYL-PEG-SATA to the surface of HAuNS is shown in Figure 15B. Briefly, TNYL-PEG-SATA (1mg/mL, 200  $\mu$ L) solution was treated with hydroxylamine (50mmol/L, 50 $\mu$ L) in total volume of 500 $\mu$ L PBS containing 10mM of EDTA (pH 7.0) before conjugation to HAuNS. The reaction mixture was stirred at room temperature for about 2 h. Then the product (TNYL-PEG-SH) was purified by passing through a PD-10 column (Amersham-Pharmacia Biotech, Uppsala, Sweden) and eluted with PBS (pH 7.4). Therefore, the purified TNYL-PEG-SH

was added into H AuNS ( $2 \times 10^{12}$  particles/mL) solution and stirred at room temperature for about 6 hours. Then PEG-SH (5 mg/mL, 0.4 mL) was added into mixture and allowed to react overnight at room temperature. The final product (TNYL-PEG-H AuNS) was purified by centrifuging at 8,000 rpm for 15 minutes and the pellet was resuspended with PBS. This process was repeated twice to remove excess peptide and free PEG-SH molecules. The purified TNYL-PEG-H AuNS was sent to the core facility in Baylor College of medicine to do the amino acid analysis. PEG-SH was conjugated to H AuNS similarly to above procedure to give PEG-H AuNS, which was used as a nonspecific control.

## **5. Photothermal Effect of different H AuNS solutions**

The photothermal effect of H AuNS solutions was measured as previously described. Briefly, the laser was a continuous wave GCSLX-05-1600m-1 fiber-coupled diode laser (Newport model 840-C). A 5-m 600- $\mu$ m core BioTex LCM-001 optical fiber was used to transfer laser light from the laser unit to the target. The laser spot size of the lens mounting at the output could be changed by changing the distance from the output to the target. The output power was separately calibrated by a handheld optical power meter (Newport model 840-C) and was found to be 1 W for a spot diameter of 3.5 mm (8 W/cm<sup>2</sup>) and a 2-amp supply current. NIR laser light (808 nm) was delivered through a quartz cuvette containing the nanoshells (100  $\mu$ L) to heat H AuNS and its derivatives. A thermocouple was inserted into the solution perpendicular to the path of the laser light to measure the temperature changes mediated by NIR laser light. The temperature was measured over a period of 15 min.

## **6. In vitro Photothermal Ablation of Tumor cells**

PC-3M, CT-26 and Hey A8-Luc cells were seeded onto a 96-well plate with a density of  $1 \times 10^5$  cells per well one day before the experiment. Cells were washed three times with culture medium without phenol red and FBS. The following groups were used: NIR laser alone, TNYL-PEG-HAuNS plus laser, PEG-HAuNS plus laser, TNYL-PEG-HAuNS with excess TNYL-PEG peptide (blocking group) plus laser. For treated with HAuNS, cells were incubated with PEG-HAuNS or TNYL-PEG-HAuNS ( $100 \mu\text{L}$ ,  $2 \times 10^{11}$  particles/mL) at  $37^\circ\text{C}$  for 2 hours. For blocking group, cells were co-incubated with TNYL-PEG-HAuNS with excess amount of TNYL-PEG peptide. After incubation, cells were washed three times with PBS to remove nonspecific binding of or unbound HAuNS. Cells were re-cultured in DMEM/F12 medium without phenol red supplemented with 10%FBS. Then cells were irradiated with near IR-region laser light centered at 808nm at an output power  $40 \text{ W/cm}^2$  for 5 min (15PLUS laser, Diomed) and incubated at  $37^\circ\text{C}$  for additional 24 h. The diode laser was coupled to a 1-m, 2-mm core fiber, which delivered a circular laser beam of 2mm in diameter to cover the central area of the microplate well. Power calibration was done automatically. Cells were washed three times with HBSS (Hank's balanced salt solution) and stained with calcein AM (green color) for detection of viable cells and Eth-D1 (red color) for detection of dead cells 24 h after the laser treatment. Cells were visualized under the Zeiss Axio Observer.Z1 fluorescence microscope (Carl Zeiss MicroImaging GmbH, Germany).

## **7. Radiolabeling**

For Radiolabeling of DOTA-TNYL-RAW and peptides,  $^{64}\text{CuCl}_2$  (74–148 MBq [ $2\text{--}4 \text{ mCi}$ ]) in 0.1 M sodium acetate (pH 5.2) was added to  $10 \mu\text{g}$  aqueous solution of DOTA-TNYL-RAW or Cy5.5-TNYL-RAW-DOTA. The reaction mixture was incubated at

70°C for 1 h. The progress of the reaction was monitored by reversed-phase high-performance liquid chromatography (RP-HPLC) with a radiodetector. EDTA was added into the solution to terminate the reaction. The  $^{64}\text{Cu}$ -labeled peptide was further purified by RP-HPLC on an Agilent 1100 system (C-18, Vydac; 4.6  $\times$  250 mm, 10 mm) and eluted at a linear gradient of 10%–90% acetonitrile in a 0.1% aqueous trifluoroacetic acid solution over 35 min at a flow rate of 1.0 mL/min.  $^{64}\text{Cu}$ -DOTA-TNYL-RAW and  $^{64}\text{Cu}$ -DOTA-TNYL-RAW-Cy5.5 peptides were collected in 1- to 2-mL fractions. The solvent was then removed, reconstituted in saline and passed through a 0.22-mm filter for using in the animal experiments. Natural copper chloride ( $^{\text{nat}}\text{CuCl}_2$ ) was used to synthesize  $^{\text{nat}}\text{Cu}$ -DOTA-TNYL-RAW under identical conditions. High-resolution electrospray ionization mass spectrometry was used to confirm the identity of  $^{\text{nat}}\text{Cu}$ -DOTA-TNYL-RAW.  $^{64}\text{Cu}$ -DOTA-TNYL-RAW was co-injected with  $^{\text{nat}}\text{Cu}$ -DOTA-TNYL-RAW into the HPLC system, which was equipped with both ultraviolet and radiodetectors to confirm its identity.

For conjugation of  $^{64}\text{Cu}$  to nanoparticles, DOTA-TA (1 mg/mL, 10  $\mu\text{L}$ ) was mixed with 1 mL aqueous solution of H AuNS ( $4 \times 10^{12}$  particles/mL) for 4 h at room temperature. The following conjugation of TNYL-PEG-SH and/or PEG-SH to AuNS, and purification was the same as above described. For radiolabeling, aliquots of TNYL-PEG-H AuNS-DOTA) or PEG-H AuNS-DOTA ( $4 \times 10^{12}$  particles/mL, 0.5 mL) in 0.1 mol/L sodium acetate solution (pH 5.5) were mixed with an aqueous solution of  $^{64}\text{CuCl}_2$  (~2 mCi) for 30 min. The radiolabeled nanoparticles were then purified by centrifugation at 8,000 rpm for 5 min and washed three times with PBS. The radiolabeling efficiency



and the stability of labeled nanoparticles were analyzed using instant thin layer chromatography (ITLC).

### **8. Immobilization of EphB4 receptor to sensor chip**

10 mM sodium acetate buffer at pH 4.5 was used to dilute the stock solution (100 µg/ml, in PBS) of EphB4/Fc into three different concentrations of solutions (25, 12.5, and 6.25 µg/ml). The diluted solution was immobilized to a CM5 sensor chip using the amine coupling reaction following manufacturer-provided procedures (BIAcore). Briefly, the surfaces of the chips in flow cells (FC)-1, -2, -3, and -4 were activated by exposing them to a mixture of 200 mM N-ethyl-N'-dimethylaminopropyl carbodiimide (EDC) and 50 mM N-hydroxysuccinimide (NHS) for 7 min. FC-1 was used as a reference surface and deactivated by directly injecting of 1 M ethanolamine at pH 8.5 for 7 min. The other three flow cells were injected with 25 µg/ml, 12.5 µg/ml, and 6.25 µg/ml EphB4/Fc solutions respectively and followed by injection of 1 M ethanolamine to block the remaining activated ester groups on the surface. Before injection of samples, the chip was allowed to stabilize for at least 2 h in HBSEP running buffer. The sensogram of immobilized EphB4 on CM-5 sensor chips were shown in figure 2A. The mechanism of coupling of EphB4 receptor to CM5 sensor chip is shown in figure 2B.

### **9. Surface Plasmon Resonance (SPR) Assay of Receptor Binding Affinity**

Binding assays were performed at 25°C in HBSEP running buffer. The peptides were diluted in HBSEP buffer, filtered, degassed, and injected at concentrations between 1.6 nM and 800 nM at a flow rate of 30 µl/min. The injection time of peptides into the HBSEP buffer was 4 min, followed by a 4-min dissociation period. After each binding cycle, the chips were regenerated using a 1-min pulse of 10 mM glycine (pH 2.2). Each

cycle consisted of a 1-min waiting period to allow monitoring of the baseline binding stability for subtraction of bulk effects caused by changes in the compositions of buffer or nonspecific binding. Because we performed double referencing, all samples were additionally injected onto an uncoated reference surface, including a sample of the running buffer, which was also tested on the EphB4/Fc coated flow cell. Data were evaluated with BIAevaluation software (version 3.0, BIACORE), applying a simple 1:1 binding mass transfer model. The obtained sensorgrams were fitted globally over the whole range of injected concentrations for both the association and dissociation phases. Equilibrium dissociation constants were then calculated from the rate constants ( $K_D = k_{off}/k_{on}$ ) (90).

#### **10. Stable transfection of Luciferase gene into U251 cells (U251-Luc)**

U251 cells were seeded in the 6-well plates ( $5 \times 10^5$  cells/well) and incubated overnight at 37°C in a humidified incubator in an atmosphere of 5% CO<sub>2</sub> 24h before the experiment. 2ml DMEM/F12 medium (without FBS) with 50ul Cignal™ Lenti Positive Control (luc) viral particles (8µg/mL polybrene) were added into the well after culture medium was removed. The plates were gently swirled to mix the solution. 6 - 8 hours later, the viral supernatant (from the first infection) from the wells was removed and the cells were re-infected with 2mL of fresh supernatant (with polybrene 8µg/ml). The next day, viral supernatant was removed and DMEM/F12 with 10% FBS was added back to the cells. 72 hours after incubation, the cells were sub-cultured into 100mm dishes and the puromycin (1µg/ml) was added into cells to select the cells expressing luciferase. After 1 week selection, luciferase activity of the selected positive cells was tested by Xenogen IVIS-200 Optical in Vivo Imaging System (Caliper Life Sciences).

## 11. Fluorescence and Darkfield microscopy

For peptide binding study, PC-3M, CT26, or A549 cells were seeded ( $1 \times 10^5$ /well) in Lab-Tek II-chambered slides (Nalge Nunc International) supplemented with DMEM/F12 medium plus 10% FBS 24h before the experiment. The cells were incubated with 100  $\mu$ L of phenol-free DMEM/F12 culture medium with addition of 10  $\mu$ M FITC-TNYL-RAW or scrambled FITC-scTNYL-RAW (AGPFNTYLRINAWSP) for 20 min at room temperature. For the blocking experiment, 10  $\mu$ M FITC-TNYL-RAW and 1 mM TNYL-RAW were simultaneously added to the cells and incubated for half an hour at 37°C. For detection of EphB4 expression, cells were fixed with 4% paraformaldehyde for 20 min and washed 3 times with PBS, then incubated with 50  $\mu$ L of phycoerythrin-conjugated rat anti-human EphB4 monoclonal antibody (R&D Systems) or rabbit anti-human EphB4 polyclonal antibody (1:100 dilution) in PBS at 4°C overnight. For polyclonal antibody, goat anti-rabbit antibody conjugated with Alexa flour 488 was used as secondary antibody (1:500 dilutions). The cell nuclei were counterstained with DAPI. After washing with PBS, the slides were mounted and visualized under an Axiovert Z.1 fluorescent microscope (Zeiss).

For nanoparticles binding study, PC-3M and CT-26 Cells were seeded at density of  $2 \times 10^5$  per well in 24 wells plate with coverslip in each well 24 h before experiment. The culture medium was removed and cells were washed with HBSS twice. Then the culture medium without FBS was added back into the cells.  $2 \times 10^{11}$  particles/mL of PEG-HAuNS or TNYL-PEG-HAuNS were added into each well and incubated for 2 hours at 37 °C. For blocking group, excess amount of free TNYL-PEG peptide (1 mg) was added with TNYL-PEG-HAuNS into cells as a control. After incubation, cells were washed with

cold PBS 3 times and counterstained with 4, 6-diamidino-2-phenylindole (DAPI; Sigma, Saint Louis, MO). Then the cells were fixed in 4% paraformaldehyde solution in 20 min at room temperature and washed with PBS 3 times. Cells on coverslip were mounted with mounting medium (Dako, CA) onto slides. The slides were examined under a fluorescence microscope with a dark-field condense to determine the binding of TNYL-PEG-HAuNS particles to tumor cells. Cells without adding nanoparticles were used as background control.

## **12. Cell binding**

For peptide uptake study, CT26, PC-3M, and A549 cells were grown in 6-cm Petri dishes as described before (25). The culture medium was replaced with 2 mL DMEM/F12 culture medium without FBS containing  $^{64}\text{Cu}$ -DOTA-TNYL-RAW (~1.48 MBq/mL [ $\sim 20\mu\text{Ci/mL}$ ], 100 nM). Cells were incubated with radiolabeled peptides at room temperature for 30, 60, or 120 min. For the blocking experiment,  $^{64}\text{Cu}$ -DOTA-TNYL-RAW peptide (~1.48 MBq/mL [ $\sim 40\mu\text{Ci/mL}$ ], 100 nM) was co-incubated with TNYL-RAW (10  $\mu\text{M}$ ) under the same conditions. Thereafter, the monolayer of cells were scraped and transferred into 5-mL tubes. The tubes were briefly stirred at a vortex mixer, and 100  $\mu\text{L}$  of the cell suspension were transferred into a micro-centrifuge tube containing 500  $\mu\text{L}$  of a 75:25 mixture of silicon oil (density, 1.05; Sigma-Aldrich) and mineral oil (density, 0.872; Acros). The mixture was centrifuged at 14,000 rpm for 5 min. After the tubes were snap-frozen in liquid nitrogen, the bottom tips containing the cell pellet were cut off. The cell pellets and supernatants were counted by a Packard Cobra Quantum g-counter (GMI) separately. The protein content in a 100- $\mu\text{L}$  of cell suspension was quantified using the Bio-Rad protein assay kit according to the

manufacturer's protocol. The radioactivity in the cell pellets and medium was counted, and the data were expressed as activity ratios of the cell pellet to the medium ([counts/min/mg of protein in pellet]/[counts/min/mg of medium]). The experiments were performed in pentaplicate.

For Nanoparticles uptake study, PC3-M and CT-26 cells were seeded on 6 cm petri dish at  $1 \times 10^6$  densities in MEM or RPMI-1640 (Gibco, Carlsbad, CA) supplemented with 10% fetal bovine serum and antibiotics (100 units/mL penicillin, 0.1mg/mL streptomycin, Biochrom AG, Holliston, MA). Cells were allowed to grow at 37°C in a humidified atmosphere with 5% CO<sub>2</sub> overnight. On the experiment day, cell culture medium was replaced with 2mL of fresh medium without FBS containing  $2 \times 10^{11}$  particles/mL <sup>64</sup>Cu-TNYL-PEG-HAuNS or <sup>64</sup>Cu-PEG-HAuNS (~2.0 MBq/mL) and cells were incubated for 2 h. After incubation, the supernatant were removed and the cells were washed with cold PBS for three times to remove non-specific binding of particles. The cells were then trypsinized and resuspended in culture medium. The cell suspension (100 µL) and the supernatants (100 µL) were counted with a gamma counter (Perkin-Elmer, Waltham, Massachusetts). The protein concentration of 100 µl cells was quantified in s separate experiment using the Bio-Rad protein assay kit according to the manufacture's protocol. Activity of the cell suspensions to supernatant ([cpm/µg of protein in cells]/ [cpm/µg of medium] were calculated and plotted against time. The experiments were performed in pentaplicate.

### **13. Animal Models**

All animal studies were performed under the guidelines and approval of the MDACC Institutional Animal Care and Use Committee. Athymic nude mice (4–6 wk old, both

sexes) were obtained from Harlan Laboratories. For mice subcutaneous tumor model, CT26, PC-3M, and A549 cells were grown in DMEM/F12 supplemented with 10% FBS, penicillin (100 IU/mL), and streptomycin (100 mg/mL) (Invitrogen) at 37 °C in a humidified atmosphere with 5% CO<sub>2</sub>. The cells were harvested by trypsinization. After centrifugation of the cell suspension at 5,000 rpm for 5 min, the culture medium was aspirated and the cell pellet was resuspended in PBS for subcutaneous injection in the right front leg of each mouse. When the size of tumor reached around 1 cm in diameter, small-animal PET/CT and biodistribution analysis were performed.

For orthotopic tumor model, Male nude mice (8-10 weeks old; Charles River Laboratories) were used for the imaging experiments. Human glioblastoma U87 cells ( $1 \times 10^6$ ) or U251 ( $3 \times 10^6$ ) stably transfected with the luciferase gene (U87-TGL) were implanted in the brain of nude mice (1 mm right to and 2.5 mm behind the bregma, and 3 mm of depth) with a small animal stereotaxic device (David Kopf Instruments). The mice were received intravenous injection of D-luciferin (4 mg/kg, Biosynth Chemistry & Biology, Staad, Switzerland) 10 days after tumor inoculation. For ovarian cancer Hey-A8 tumor model, 1 million tumor cells were intraperitoneally injected into nude mice. Tumor burden as measured by luciferase activity was measured by using Xenogen IVIS-200 Optical in Vivo Imaging System (Caliper Life Sciences) for bioluminescence imaging (BLI). The bioluminescence signal generated in mice was imaged and quantified using the LIVINGIMAGE V.2.11 software and IGOR image analysis software (V.4.02 A, WaveMetrics). Region of interest (ROI) was manually selected and signal intensity expressed in terms of number of photons/sec.

#### **14. Small-Animal PET/CT**

Mice bearing PC-3M tumors (n=4 EphB4-positive), CT26 tumors (n =4; EphB4-positive), or A549 tumors (n=4; EphB4-negative) were imaged with small-animal PET/CT at various times after intravenous injection of 7.4 MBq (200  $\mu$ Ci) of  $^{64}\text{Cu}$ -DOTA-TNYLRAW (0.5–1 $\mu$ g). For the blocking group, the tumor-bearing mice (n=2) were co-injected with 7.4 MBq (200  $\mu$ Ci) of  $^{64}\text{Cu}$ - DOTA-TNYL-RAW and cold TNYL-RAW peptide at a concentration of 50  $\mu$ g/mouse. Images were acquired using an Inveon PET/CT system (Siemens). The spatial resolution of the PET system is approximately 1.4 mm. Tumor-bearing mice were anesthetized with isoflurane (2% in oxygen) and placed prone. The CT parameters were as follows: x-ray voltage, 80 kVp; anode current, 500 mA; and exposure time of each of the 360 rotational steps, 300–350 ms. Images were acquired at 1, 4, and 24 h after intravenous administration of  $^{64}\text{Cu}$ -DOTA-TNYL-RAW. Images were reconstructed using the 2-dimensional ordered-subsets expectation maximization algorithm. PET and CT image fusion and image analysis were performed using Inveon Research Workplace (Siemens Preclinical Solutions). In order to calculate tumor voxel intensity, an irregular 3-dimensional region of interest (ROI) was manually drawn to cover the whole tumor on CT and then copied to the corresponding PET images. A circular ROI was drawn on the muscle of the legs. An ROI was also drawn on a standard (radiotracer solution containing 1% of the injection dose) placed along with the animals. The mean activities within the ROI of the tumor and muscle were calculated in an IRW workstation (Siemens).

Mice bearing U251 tumors (n=4) were imaged with small-animal PET/CT at various times after intravenous injection of 7.4 MBq (200  $\mu$ Ci) of  $^{64}\text{Cu}$ -Cy5.5-TNYLRAW-DOTA (0.5–1  $\mu$ g). For the blocking experiment, the U251 tumor-bearing mice (n =3)

were coinjected with 7.4 MBq (200  $\mu$ Ci) of  $^{64}\text{Cu}$ -Cy5.5-TNYL-RAW-DOTA and cold Cy5.5-TNYL-RAW-DOTA peptide at a dose of 50  $\mu\text{g}/\text{mouse}$ . Images were acquired using an Inveon PET/CT system (Siemens). Tumor-bearing mice were anesthetized with isoflurane (2% in oxygen) and placed prone. The CT parameters were as follows: x-ray voltage, 80 kVp; anode current, 500 mA; and exposure time of each of the 360 rotational steps, 300–350 ms. Images were acquired at 1 and 24 h after intravenous administration of  $^{64}\text{Cu}$ -Cy5.5-TNYL-RAW-DOTA. Images were reconstructed using the 2-dimensional ordered-subsets expectation maximization algorithm. PET and CT image fusion and image analysis were performed using Inveon Research Workplace (Siemens Preclinical Solutions). For tumor voxel intensity calculation, an irregular 3-dimensional region of interest (ROI) was manually drawn corresponding to PET images. A circular ROI was drawn on the normal brain part. An ROI was also drawn on a standard (radiotracer solution containing 1% of the injection dose) placed along with the animals. The mean activities within the ROI of the tumor and normal brain were calculated in an IRW workstation (Siemens).

## **15. Micro-PET imaging**

CT-26 tumors were grown subcutaneously in the right thigh of the female nude mice (20–25 g; Harlan Sprague Dawley, Indianapolis, IN) by injection of  $1 \times 10^6$  tumor cells suspended in PBS. One week after inoculation, when tumor reached approximately 8–10 mm in diameter, mice were divided into 2 groups ( $n=3$ ). Mice (group 1) were intravenously injected  $^{64}\text{Cu}$ -TNYL-PEG-HAuNS and mice (group 2) were injected with  $^{64}\text{Cu}$ -PEG-HAuNS ( $1 \times 10^{11}$  particles/mouse, 200  $\mu\text{Ci}/\text{mouse}$ ; 0.2 mL). The mice were anesthetized with 2% isoflurane and placed in the prone position, and micro-PET



imaging was acquired at 1 h, 6 h, and 24 h after injection of the radiolabeled nanoparticles using an R4 microPET unit (Siemens Medical Solutions USA, Inc.), which has an approximate resolution of 2 mm in each axial direction. Mice were maintained under anesthesia with 1%–2% isoflurane, and a heating lamp was used to maintain their body temperature during acquisition. Small-animal PET images were reconstructed with the ordered-subsets expectation maximization algorithm using 16 subsets and 4 iterations.

## **16. Near Infrared (NIR) Optical Imaging**

Mice bearing U87 tumors (n =4) or U251 tumors (n=4) were imaged with Xenogen IVIS-200 Optical in Vivo Imaging System (Caliper Life Sciences) at various times after intravenous injection of 10 $\mu$ g of  $^{64}\text{Cu}$ -Cy5.5-TNYL-RAW-DOTA or  $^{64}\text{Cu}$ -Cy5.5-scramble peptide. Cy5.5 fluorescence filter set (excitation 615-665 nm, emission 695-770 nm, background 580-610 nm) was applied. After mice were sacrificed, the fluorescence signal of different organs and tumors were analyzed by Living Imaging LIVINGIMAGE V.2.11 software and IGOR image analysis software (V.4.02 A, WaveMetrics). Region of interest (ROI) was manually selected and signal intensity expressed in terms of number of photons/sec.

## **17. In Vivo Biodistribution studies**

For nude mice subcutaneous tumor models, nude mice bearing PC-3M, CT26, and A549 xenografts (n =4/group) were injected with 0.74 MBq (20  $\mu$ Ci, 50 ng) of  $^{64}\text{Cu}$ -DOTA-TNYL-RAW peptide to evaluate the biodistribution of the radiotracer. For the blocking experiment, the tumor-bearing mice (n=4) were coinjected with 0.74 MBq (20  $\mu$ Ci) of  $^{64}\text{Cu}$ -DOTA-TNYL-RAW and 200-fold cold TNYL-RAW peptide. The animals

were sacrificed at 4 and 24 h after injection. The organs of interest were excised and weighed and their radioactivity was counted by an automatic g-counter (GMI). The stomach and intestines were not emptied before radioactivity measurements. The percentage of injected dose per gram of tissue (%ID/g) was calculated by dividing the %ID organ by the weight of the organ. Values were expressed as mean $\pm$ SD.

Mice bearing CT-26 tumors were prepared as described previously. When the tumor reached 4-6 mm in diameter, the mice were randomly assigned into 2 groups (n=6). Mice (group 1) were intravenously injected  $^{64}\text{Cu}$ -TNYL-PEG-HAuNS and mice (group 2) were intravenously injected with  $^{64}\text{Cu}$ -PEG-HAuNS ( $1 \times 10^{11}$  particles/mouse, 20  $\mu\text{Ci}$ /mouse; 0.2 mL). Mice were killed by  $\text{CO}_2$  overexposure 24 h after injection of radiolabeled nanoparticles. Blood, heart, liver, spleen, kidney, lung, stomach, intestine, muscle, bone, brain, and tumor tissues were removed and weighed, and the radioactivity was measured with a gamma counter (Perkin-Elmer, Waltham, Massachusetts). Uptakes of  $^{64}\text{Cu}$ -labeled HAuNS in various organs were expressed as percentages of injected dose per gram of tissue (%ID/g).

For HEY A8-Luc intraperitoneal model,  $1 \times 10^6$  cells were intraperitoneally injected into mice. Tumor burden on mice was monitored by bioluminance activity. After tumor reached to 0.2 to 1cm, the he mice were randomly assigned into 2 groups (n=6). Mice (group 1) were intravenously injected  $^{64}\text{Cu}$ -TNYL-PEG-HAuNS and mice (group 2) were intravenously injected with  $^{64}\text{Cu}$ -PEG-HAuNS ( $1 \times 10^{11}$  particles/mouse, 20  $\mu\text{Ci}$ /mouse; 0.2 mL). Mice were killed by  $\text{CO}_2$  overexposure 24 h after injection of radiolabeled nanoparticles. Blood, heart, liver, spleen, kidney, lung, stomach, intestine, muscle, bone, brain, and tumor tissues were removed and weighed, and the radioactivity

was measured with a gamma counter (Perkin-Elmer, Waltham, Massachusetts). Uptakes of  $^{64}\text{Cu}$ -labeled HANs in various organs were expressed as percentages of injected dose per gram of tissue (%ID/g).

## **18. Autoradiography and Optical Imaging**

Mice brains containing U251 tumors were harvested at the end of the imaging session were snap-frozen and sectioned into 4- $\mu\text{m}$  sections. The sections were photographed and exposed onto BAS-SR 2025 Fuji phosphorus films. The film was scanned with a FLA5100 Multifunctional Imaging System (Fujifilm Medical Systems USA, Stamford, CT). After autoradiography study, optical images of the sections were acquired by scanning at 800 nm using an Odyssey infrared imaging system (LI-COR Biosciences, Lincoln, NE).

## **19. H&E staining and Immunohistochemical Analysis**

For nude mice subcutaneous tumor models, after the small-animal PET/CT studies were completed, the mice were sacrificed and the tumors were excised, snap-frozen, and cut into 4- $\mu\text{m}$  sections. For immunohistochemical analysis, frozen tumor sections were fixed in 4% paraformaldehyde solution for 20 min at room temperature and washed with PBS 3 times. Tumor sections were blocked with 10% goat serum for 30 min at room temperature, and the slides were then incubated with rabbit anti-EphB4 antibody (U-200, 1:100 dilution) in PBS at 4°C overnight. After incubation with primary antibody, slides were washed with PBS 3 times and incubated with secondary goat antirabbit antibody conjugated with Alexa Fluor 488 (1:500 dilution; Invitrogen). Slides were washed again in PBS and counterstained with DAPI. Microphotographs were taken under a Zeiss Axiovert Z.1 fluorescence microscope with the same conditions and displayed at the

same scale to make sure that the relative brightness observed in the images reflected the difference in EphB4 expression level.

After the small-animal PET/CT and near infrared optical studies were completed, the mice were sacrificed and tumors in mice brains were excised, snap-frozen and cut into 4-mm sections. For immunohistochemical analysis, frozen tumor sections were fixed in 4% paraformaldehyde solution for 20 min at room temperature and washed with PBS 3 times. Tumor sections were blocked with 10% goat serum for 30 min at room temperature, and the slides were then incubated with rabbit anti-EphB4 antibody (U-200, Santa Cruz Biotech, CA, 1:100 dilution) and rat anti-mouse CD31 (Millipore, Billerica, MA, 1:50 dilution) in PBS at 4°C overnight. After incubation with primary antibody, slides were washed with PBS 3 times and incubated with secondary goat anti-rabbit antibody conjugated with Alexa Fluor 488 (1:500 dilution; Invitrogen) and donkey anti-rat antibody conjugated with Alexa Fluor 594 (1:500 dilution; Invitrogen). Slides were washed again in PBS and counterstained with DAPI. Frozen blocks were sent to the core histology facility in MD Anderson Cancer Center for H&E staining. Microphotographs were taken and visualized by a Zeiss AxioCam MRc5 color camera.

## **20. Photothermal Ablation of Cancer Cells with TNYL-PEG-HAuNS in Vivo**

Nude mice were inoculated subcutaneously with  $1 \times 10^6$  CT-26 cells in the right side of the rear legs 10 days before the experiment. When tumor growth reached 7-10 mm in diameter, mice were randomly assigned into 4 groups (n=5). Mice (group 1) were intravenously injected with TNYL-PEG-HAuNS ( $2 \times 10^{12}$  per mouse, 200  $\mu$ L); Mice (group 2) were injected with PEG-HAuNS ( $2 \times 10^{12}$  per mouse, 200  $\mu$ L); Mice (group 3) were injected saline as control; Mice (group 4) were not received any treatment. The

tumors from groups 1, 2, 3 were irradiated with NIR laser at  $3\text{W}/\text{cm}^2$  for 3 minutes 24 h after injection of nanoparticles. The mice were killed 24 h after the laser treatment, then the tumor was removed and cryosectioned into  $5\text{-}\mu\text{m}$  sections for H&E staining. The slides were visualized under a Zeiss Axio Observer.Z1 fluorescence microscope. The images were taken using a Zeiss AxioCam MRc5 color camera.

Nude mice were inoculated with  $1 \times 10^6$  Hey-A8-Luc cells intraperitoneally 14 days before experiments. Tumor growth was monitored by luciferase activity. Mice were randomly assigned into 3 groups. Mice (group 1) were injected with PEG-HAuNS ( $2 \times 10^{12}$  per mouse,  $200\text{ }\mu\text{L}$ ). Mice (group 2) were injected saline as control. Mice (group 3) were not received any treatment. The abdomens of mice bearing tumors were cut and open, and then tumors were exposed. Because tumors grown in mice belly as multiple nodules, so some nodules were used as internal control. 24 h after injection of nanoparticles, the tumors from groups 1 and 2 were irradiated with NIR laser at  $2\text{W}/\text{cm}^2$  for 3 minutes. The mice were killed 24 h after the laser treatment, and then the tumors and normal tissue around the tumors treated with laser were removed and cryosectioned into  $5\text{-}\mu\text{m}$  sections for H&E staining. The slides were visualized under a Zeiss Axio Observer.Z1 fluorescence microscope. The images were taken using a Zeiss AxioCam MRc5 color camera.

## **21. Statistical Analysis**

Statistical analysis was performed with GraphPad Prism v4.0 software (La Jolla, CA). Unless otherwise stated, group comparisons were made using standard ANOVA methods. Groups with  $P < 0.05$  were considered statistically significant.

## **RESULTS**

# **1. Synthesize and evaluate $^{64}\text{Cu}$ -labeled TNYL-RAW peptides for PET imaging of EphB4 receptors in prostate and colon cancer xenograft models**

## **1.1 Chemistry, Radiochemistry, and Stability**

Figure 1A shows the structure of  $^{\text{nat}}\text{Cu}/^{64}\text{Cu}$ -DOTA-TNYL-RAW. The reaction scheme for the synthesis of  $^{\text{nat}}\text{Cu}/^{64}\text{Cu}$ -DOTA-TNYL-RAW is shown in Figure 1B. TNYL-RAW, DOTA-TNYL-RAW or FITC-TNYL-RAW was eluted as a single peak with a retention time of 13.8 min,  $m/z = 1,705.7764$  for  $[\text{M}+\text{H}]^+$  ( $\text{C}_{80}\text{H}_{117}\text{N}_{22}\text{O}_{20}$ , calculated  $[\text{M}+\text{H}]^+$ : 1,705.8814); 12.6 min,  $m/z = 2,092.0554$  for  $[\text{M}+\text{H}]^+$  ( $\text{C}_{96}\text{H}_{143}\text{N}_{26}\text{O}_{27}$ , calculated  $[\text{M}+\text{H}]^+$ : 2,092.0616) and 15.6 min,  $m/z = 2,094.9003$  for  $[\text{M}+\text{H}]^+$  ( $\text{C}_{101}\text{H}_{128}\text{N}_{23}\text{O}_{25}\text{S}$ , calculated  $[\text{M}+\text{H}]^+$ : 2,094.9172) respectively. The formation of the  $^{\text{nat}}\text{Cu}$  (II)-labeled complex  $^{\text{nat}}\text{Cu}$ -DOTA-TNYL-RAW was confirmed by mass spectrometry (Figure 1C), with  $m/z = 1,076.9957$  for  $[\text{M}+\text{Cu}]^{2+}$  ( $\text{C}_{96}\text{H}_{143}\text{CuN}_{26}\text{O}_{27}$ , calculated  $[\text{M}+\text{Cu}]^{2+}$ : 1,076.9917).  $^{\text{nat}}\text{Cu}$ -DOTA-TNYL-RAW (ultraviolet detector) and  $^{64}\text{Cu}$ -DOTA-TNYL-RAW (radiodetector) had almost identical retention times (12.5 and 12.6 min, respectively) under the similar HPLC condition (Figure 1D.) The radiochemical purity of  $^{64}\text{Cu}$ -DOTA-TNYL-RAW (the ratio of the main product peak to all peaks) was determined by HPLC to be more than 95%. The specific activity of  $^{64}\text{Cu}$ -DOTA-TNYL-RAW used in the *in vitro* and *in vivo* experiments was typically 7.4–14.8 MBq/nmol (0.2–0.4 Ci/mmol) at the end of synthesis. The stability of  $^{64}\text{Cu}$ -DOTA-TNYL-RAW was checked in culture medium (DMEM with 10%FBS) for up to 24 h at 37 °C. Around 30% of the  $^{64}\text{Cu}$ -DOTA-TNYL-RAW was degraded after 2 h of incubation in culture medium at 37°C.

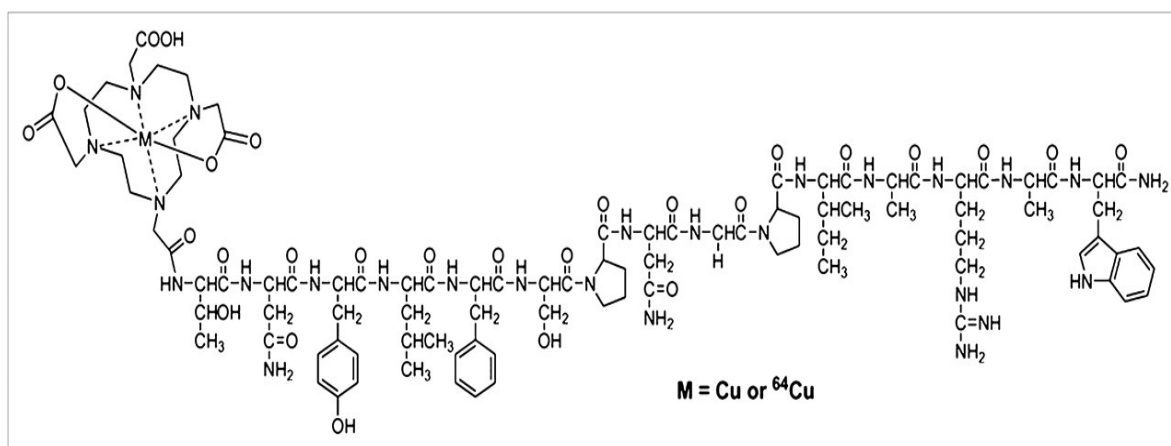


**Figure 1A.** Structure of  $^{64}\text{Cu}$ -DOTA-TNYL-RAW and  $^{\text{nat}}\text{Cu}$ -DOTA-TNYL-RAW peptides (peptide sequence: TNYLRFSPNGPIARAW) (Reprinted with permission of (90))

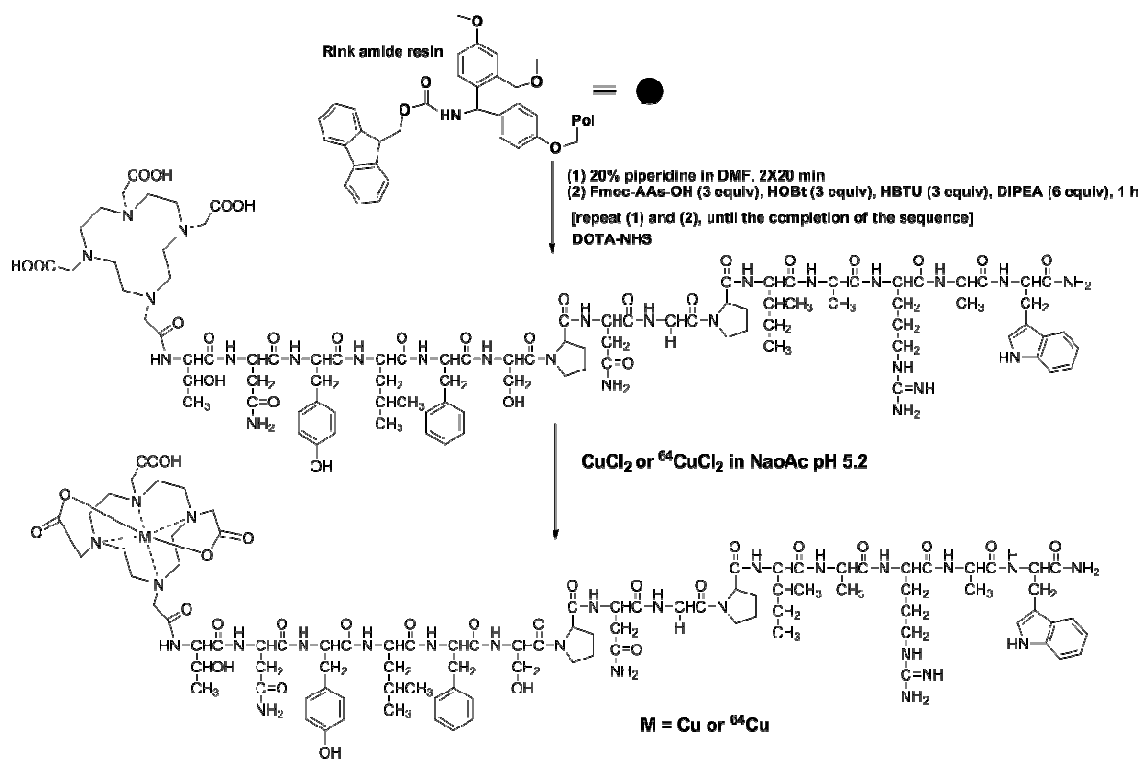


**Fig 1B.** Reaction scheme of synthesis of  $^{64}\text{Cu}/^{\text{nat}}\text{Cu}$ -DOTA-TNYL-RAW

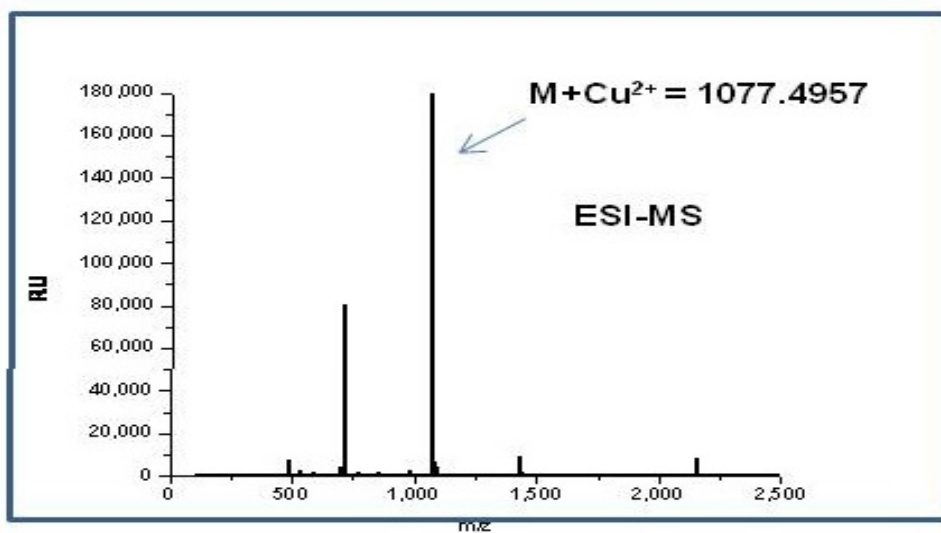


**Figure 1C.** Electrospray ionization mass spectrometry spectrum of <sup>nat</sup>Cu-DOTA-TNYL-RAW (Reprinted with permission of (90))



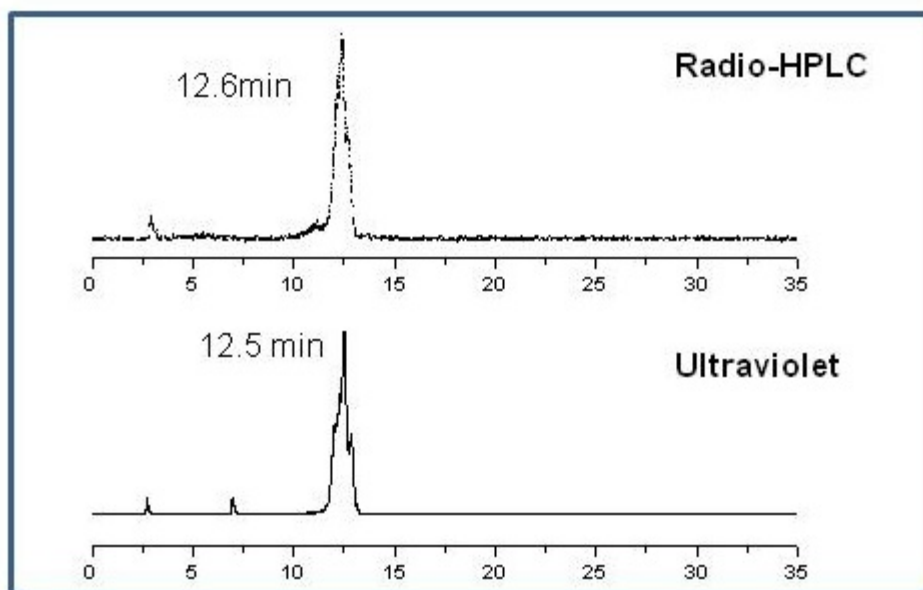
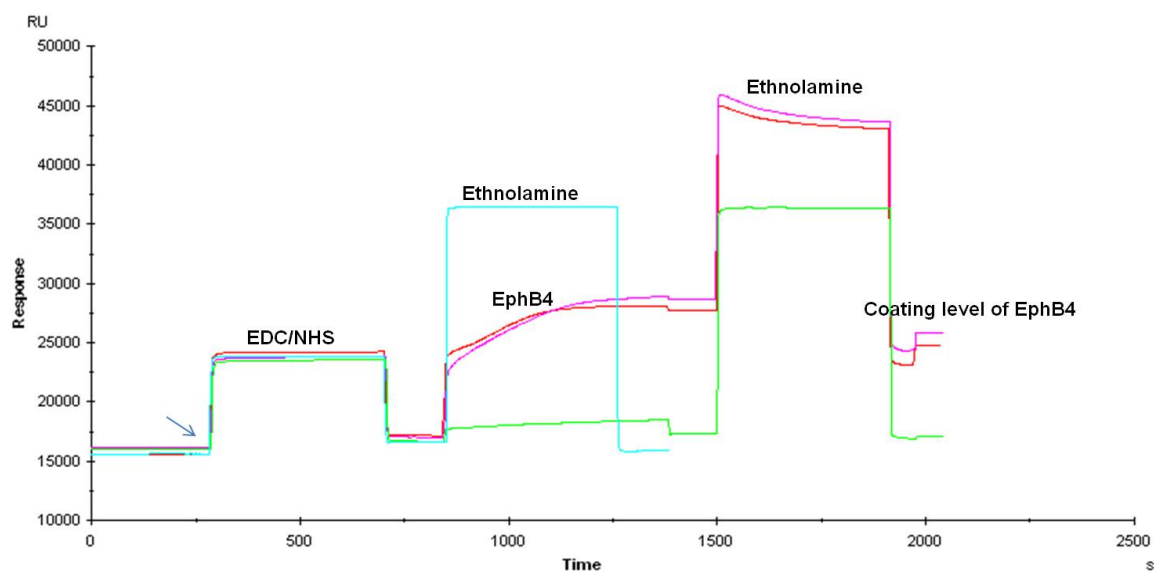


**Figure 1D.** Radio-HPLC chromatogram of  $^{64}\text{Cu}$ -DOTA-TNYL-RAW ( $t_R = 12.6$  min) compared with chromatogram of  $^{\text{nat}}\text{Cu}$ -DOTA-TNYL-RAW ( $t_R = 12.5$  min) with UV detection at 210 nm. (Reprinted with permission of (90))

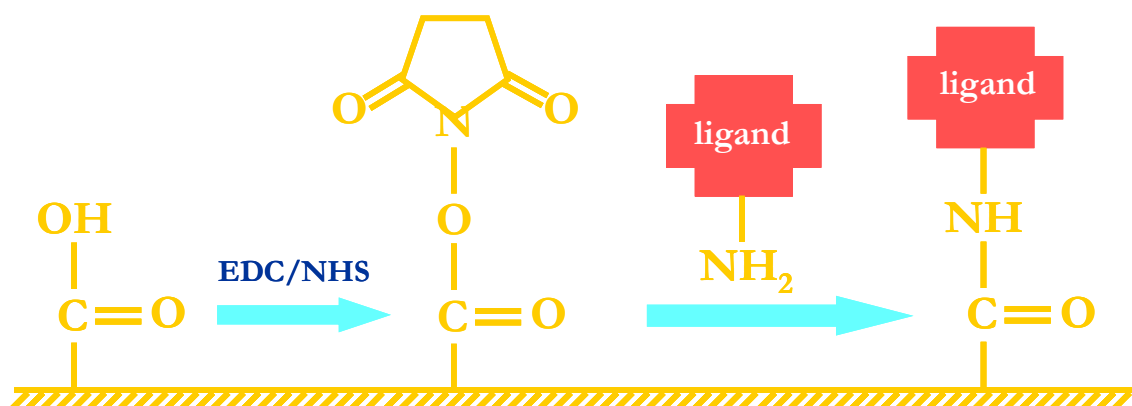
## 1.2 Binding Affinity of TNYL-RAW and DOTA-TNYL-RAW-DOTA, $^{\text{Nat}}\text{Cu}$ -DOTA-TNYL-RAW and scramble peptides

Figure 2A shows the sensogram of successful coating of EphB4 receptor on CM-5 sensor chip. Figure 2B shows the mechanism of coupling of EphB4 ligand to the surface of the CM5 sensor chip. Figure 2C shows representative sensorgrams obtained from SPR analyses of TNYL-RAW and DOTA-TNYL-RAW,  $^{\text{Nat}}\text{Cu}$ -DOTA-TNYL-RAW and scramble peptides with fitting curves obtained using a global 1:1 mass transfer model. The corresponding binding kinetics and affinity data are summarized in Table 1. TNYL-RAW had a  $K_D$  of 3.06 nM. Conjugation of DOTA to the N terminus of the peptides decrease the binding affinity, the  $K_D$  value of the TNYL-RAW increased to 23.3 nM. Interestingly, chelation of  $\text{Cu}^{2+}$  to the DOTA-TNYL-RAW restored the binding affinity of peptides, with the  $K_D$  value back to around 1.98 nM. Because we didn't see response

of scramble peptide to EphB4 receptor on SPR assay (Figure 2B), there was no detectable binding ability of scramble peptides to the coated receptors.



**Figure 2A.** Sensogram of successful coating of EphB4 receptor on CM-5 sensor chip/ EDC/NHS was used to activation of chip. Ethanolamine was used to saturate unbound site on the sensor chip.



**Figure 2B.** Mechanism of coupling of EphB4 ligand to the surface of CM5 sensor chip

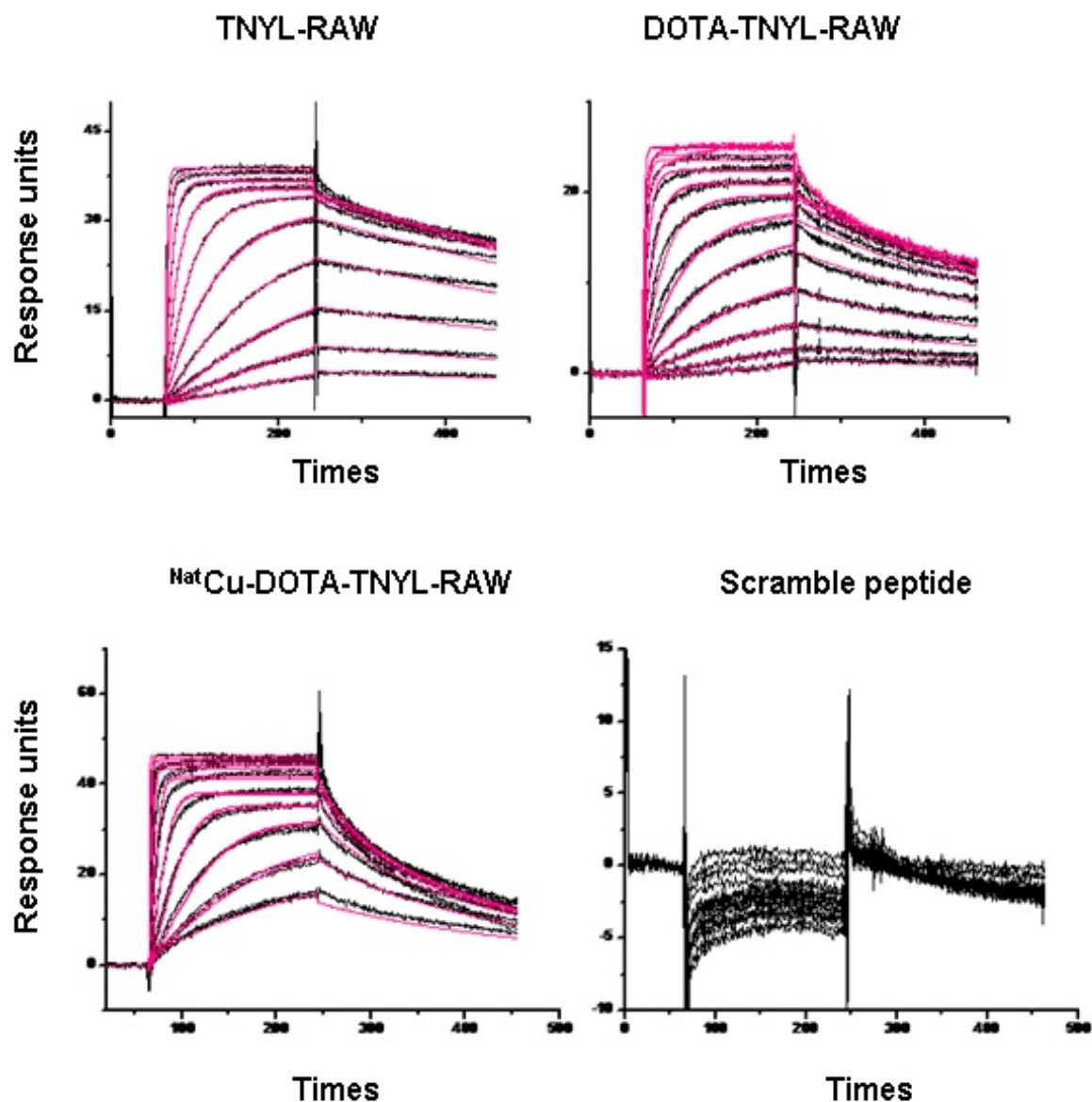


**Figure 2C.** SPR sensorgrams of TNYL-RAW and DOTA-TNYL-RAW-DOTA,  $^{Nat}\text{Cu}$ -DOTA-TNYL-RAW and scramble peptides on sensor chips coated with EphB4. Peptides were injected as ten 2-fold-concentration series from 1.6 to 800 nM and were analyzed in duplicate binding cycles. Datasets (shown in black) are overlaid with curves fit to 1:1 mass transfer interaction model (red lines). Vertical axes in response units represent binding of each peptide to immobilized EphB4. (Reprinted with permission of (90))

Analyte	$k_{on}$ [M <sup>-1</sup> s <sup>-1</sup> ]	$k_{off}$ [s <sup>-1</sup> ]	$K_D$ [M]	$\chi^2$
TNYL-RAW	$4.26 \times 10^5$	$1.3 \times 10^{-3}$	$3.06 \times 10^{-9}$	0.155
DOTA-TNYL-RAW	$1.10 \times 10^5$	$2.56 \times 10^{-3}$	$2.33 \times 10^{-8}$	0.281
<sup>Nat</sup> Cu-DOTATNYL-RAW	$6.89 \times 10^6$	$1.31 \times 10^{-2}$	$1.89 \times 10^{-9}$	1.86

**Table 1.** Association, Dissociation Rates and  $K_D$  of different TNYL-RAW peptides and derivatives interacting with immobilized EphB4 receptors obtained from SPR Analysis.

### 1.3 Fluorescence microscope

Previous papers have shown that the EphB4 receptors are overexpressed in prostate and colon cancer cells (38, 40). Immunofluorescence study confirmed the positive expression of EphB4 receptor on the surface of CT-26 and PC-3M cells after stained with phycoerythrinconjugated rat antihuman EphB4 monoclonal antibody, but not on the surface of EphB4-negative A549 cells (Fig3B). The structure details of FITC-TNYL-RAW peptides were shown in Fig 3A. FITC-TNYL-RAW peptides (green color) strongly bind to the surface of PC-3M and CT-26 cells, but not on the EphB4-negative A549 cells. The specific binding of FITC-TNYL-RAW peptides to the CT-26 and PC-3M cells were confirmed by the blocking or scramble peptide binding study which showed that the binding of these FITC labeled peptides was efficiently blocked by co-incubation with excess amount of TNYL-RAW peptides and there was no detectable binding of FITC labeled scramble peptides binding to those EphB4 positive peptides.

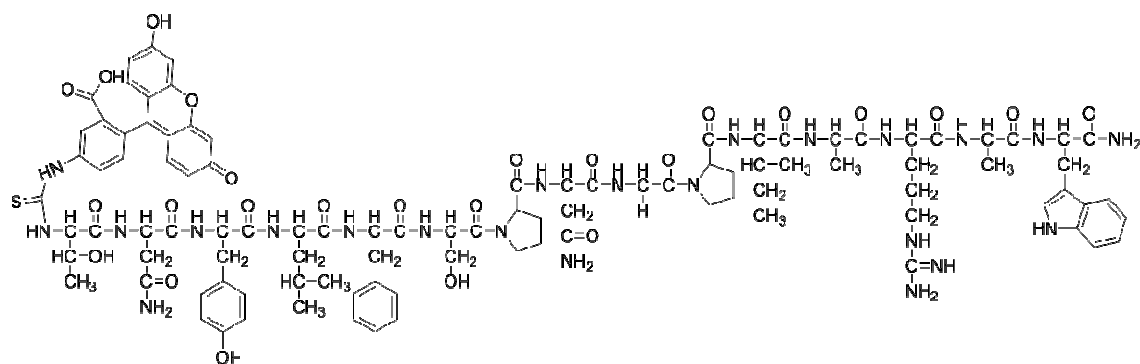


**Fig 3A** The structure details of FITC-TNYL-RAW

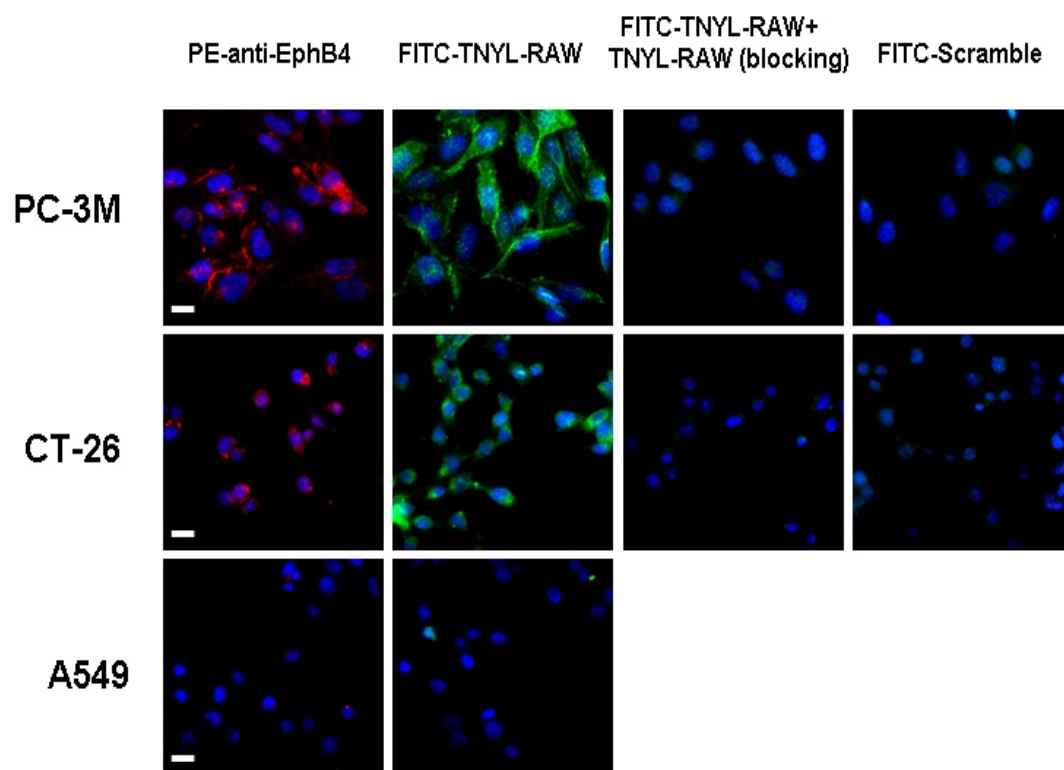


**Figure 3B.** Fluorescence photomicrographs of PC-3M cells treated with FITC-TNYL-RAW (10  $\mu$ M, green) or scrambled peptide FITC-sc-TNYL-RAW (10 $\mu$ M, green) for 20 min at room temperature. Cells were also stained with phycoerythrin-conjugated anti-EphB4 antibody (red) for expression of EphB4 receptors. For blocking experiment, FITC-TNYL-RAW (10  $\mu$ M) was coincubated with TNYL-RAW (1mM). Cell nuclei were counterstained with DAPI (blue). Bar =20  $\mu$ m. (Reprinted with permission of (90))

#### 1.4 In vitro radioisotope binding assay

$^{64}\text{Cu}$ -DOTA-TNYL-RAW peptides were highly uptake by CT-26 and PC3-M cells. The uptake of radiolabeled peptides of these cells was increased with time from 30min to 2 hours. The specific binding of these peptides can be efficiently blocked by adding excess amount of cold peptide TNYL-RAW and the total binding was decreased by around 10 fold at all time points (Figure 4A and 4B).

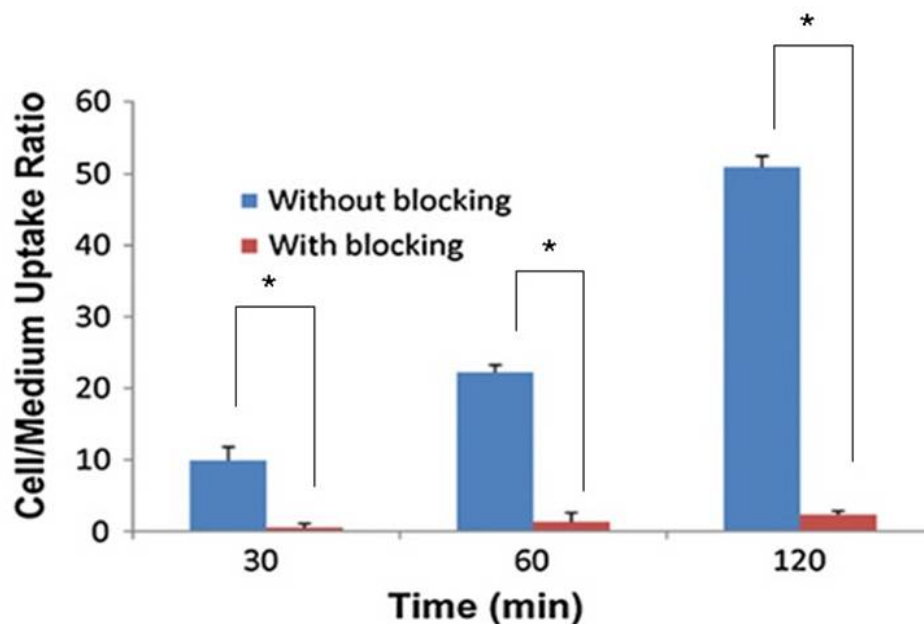


**Figure 4A.** Uptake of  $^{64}\text{Cu}$ -DOTA-TNYL-RAW in EphB4-positive PC-3M cells. Cell-to medium uptake ratio is expressed as (counts/ min/mg of protein in pellet)/(counts/min/mg of medium).  $^{64}\text{Cu}$ -DOTA-TNYL-RAW showed increased uptake over time in PC-3M cells. \* Indicates the p value <0.005. (Reprinted with permission of (90))

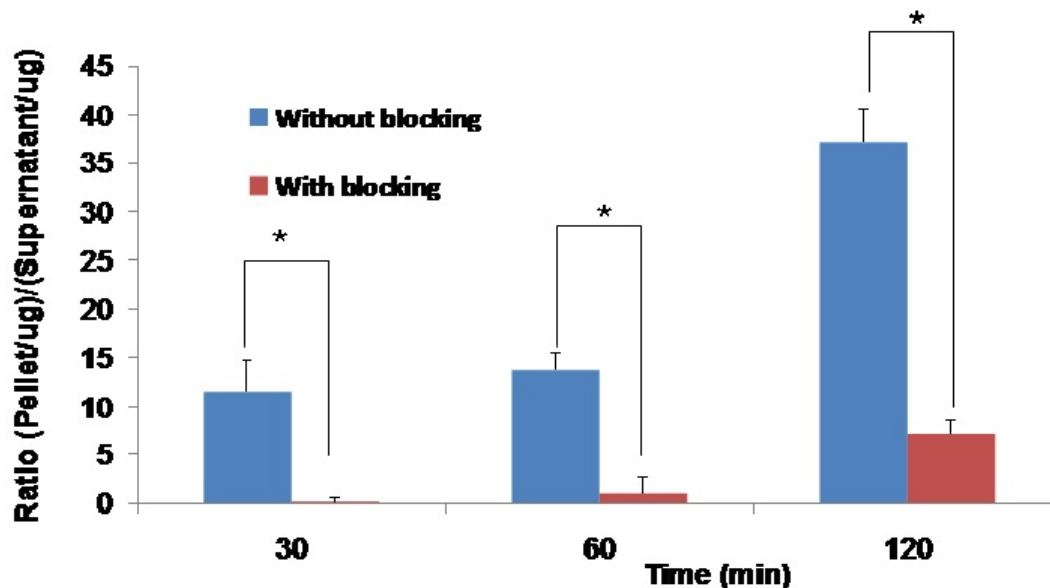


**Figure 4B.** Uptake of  $^{64}\text{Cu}$ -DOTA-TNYL-RAW in EphB4-positive CT-26 cells. Cell-to medium uptake ratio is expressed as (counts/ min/mg of protein in pellet)/(counts/min/mg of medium).  $^{64}\text{Cu}$ -DOTA-TNYL-RAW showed increased uptake over time in PC-3M cells. \* Indicates the p value <0.005. (Reprinted with permission of (90))

### 1.5 Small animal Micro PET/CT

Figure 5A showed the micro PET/CT results of nude mice bearing tumors after tail vein injection of  $^{64}\text{Cu}$ -DOTA-TNYL-RAW. CT-26 tumors were clearly visualized at 1h and 4 h after injection of  $^{64}\text{Cu}$  labeled TNYL-RAW peptides. But for PC-3M tumors, the highest uptake of  $^{64}\text{Cu}$ -DOTA-TNYL-RAW time point was 24 h after injection of radiolabeled peptides. There was very low uptake of  $^{64}\text{Cu}$ -DOTA-TNYL-RAW in EphB4 negative A549 cells. According to the ROI calculations described in the above methods, the uptake of  $^{64}\text{Cu}$ -DOTA-TNYL-RAW in CT26 tumors was rapid, from 1.3 %ID/g at 1h post injection to 2.6 %ID/g at 4 h post injection, respectively. But the level of tumor radioactivity in CT26 tumor was barely detectable at 24 h after injection of radio tracer (Fig. 5A). The uptake values of  $^{64}\text{Cu}$ -DOTA-TNYL-RAW in PC-3M tumors were 1.4, 3.2, and 3.6 %ID/g at 1, 4, and 24 h after injection, respectively. The

For EphB4-negative A549 tumors, the uptake of  $^{64}\text{Cu}$ -DOTA-TNYL-RAW was at the level of 1.7, 1.5, and 1.2 %ID/g at 1, 4, and 24 h after intravenous injection of radiotracer. The summary of the different uptake of  $^{64}\text{Cu}$ -DOTA-TNYL-RAW in CT26, PC-3M and A549 tumors at different time points was shown in table 2. We found that the time point of highest uptake value of radio tracer is different in CT26 (4h post injection) and PC-3M (24h post injection) tumors *in vivo* based on our micro PET/CT results, so we chose different time points to do blocking study for CT26 (4h post injection) and PC-3M (24h post injection) tumors. Uptake of  $^{64}\text{Cu}$ -DOTA-TNYL-RAW in CT26 tumors was blocked by co-injection of excess amount of cold TNYL-RAW peptides (50 $\mu\text{g}$ /mouse) (micro PET/CT images were taken at 4h post injection of radio tracers). The specific uptake of radiotracer in PC-3M tumors was efficiently blocked by co-injection of excess amount of cold TNYL-RAW peptide (50 $\mu\text{g}$ /mouse) (micro PET/CT images were taken at 24h post injection of radio tracers). Based on the calculations of ROI, the co-injection of cold peptides caused about 77% and 81% reduction in  $^{64}\text{Cu}$ -DOTA-TNYL-RAW uptake in CT-26 and PC-3M tumors respectively. (ROI of tumor (non-block)-ROI of tumor (block)/ ROI of tumor (non-block)).



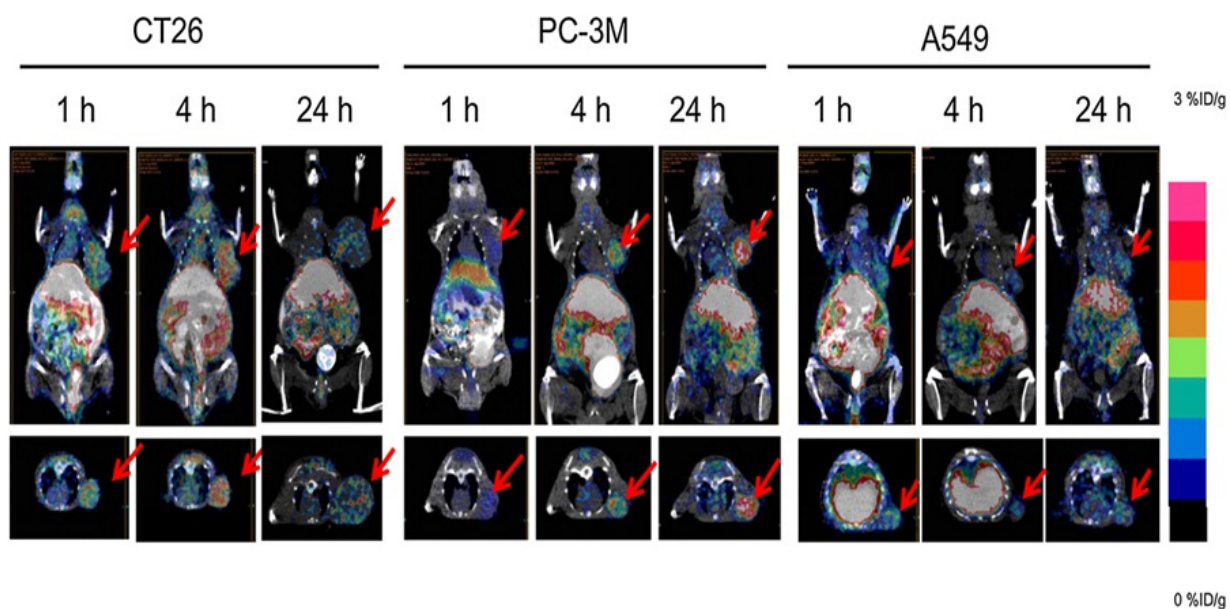


**Figure 5A.** Representative small-animal PET/CT imaging of mice bearing CT26, PC-3M, and A549 tumors after tail vein injection of  $^{64}\text{Cu}$ -DOTA-TNYL-RAW (n=4). Arrows indicate different tumors (PC-3M, CT26 and A549). (Reprinted with permission of (90))

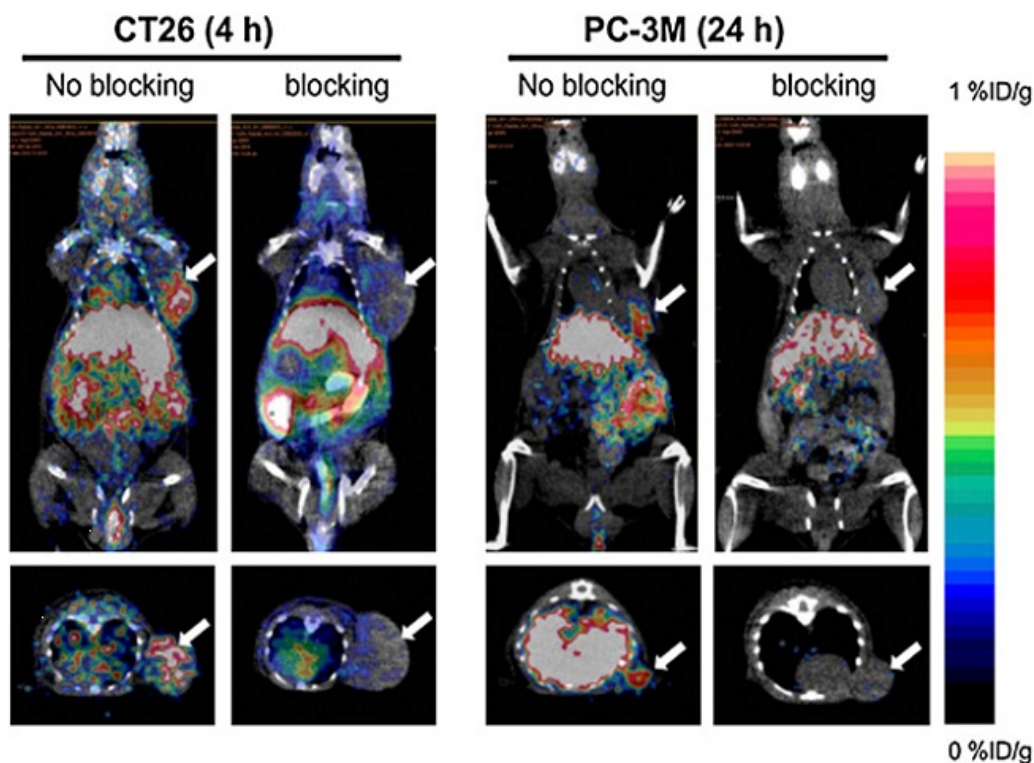


**Figure 5B.** Representative micro PET/CT images showed the uptake of  $^{64}\text{Cu}$ -DOTA-TNYL-RAW was blocked in CT26 tumors at 4 h and in PC-3M tumors at 24 h after co-injection of  $^{64}\text{Cu}$ -DOTA-TNYL-RAW with cold TNYL-RAW (50 $\mu\text{g}$ /mouse). Arrows indicate tumors. (Reprinted with permission of (90))

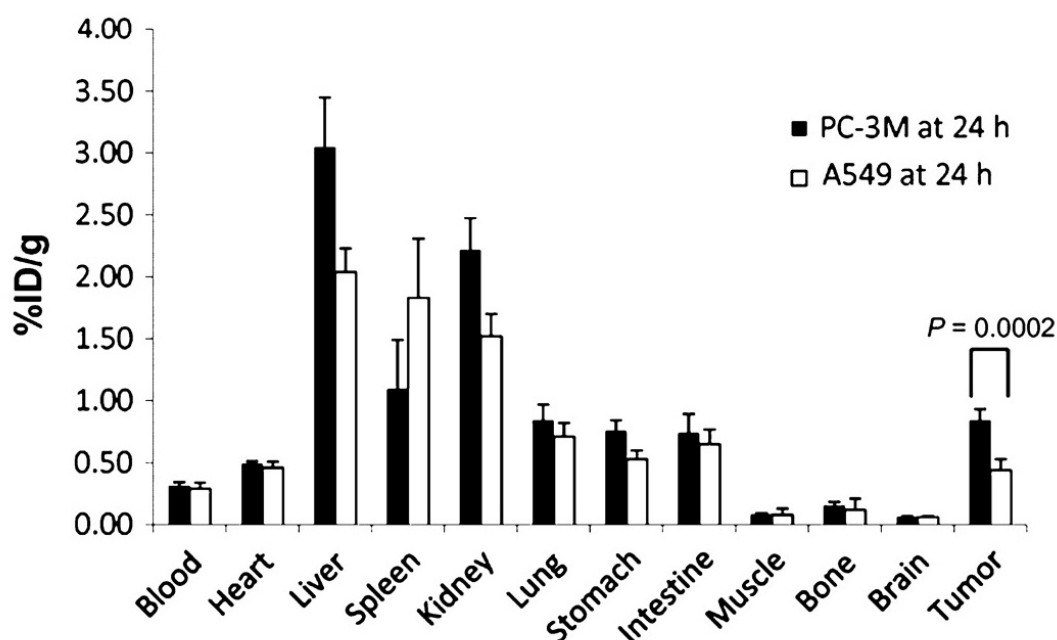
Tumor Type	1h	4h	24h
CT26	1.3%	2.6%	N/A
PC-3M	1.4%	3.2%	3.6%
A549	1.7%	1.5%	1.2%

**Table 2** Shows the summary of summary of the different uptake of  $^{64}\text{Cu}$ -DOTA-TNYL-RAW in CT26, PC-3M and A549 tumors at different time points.

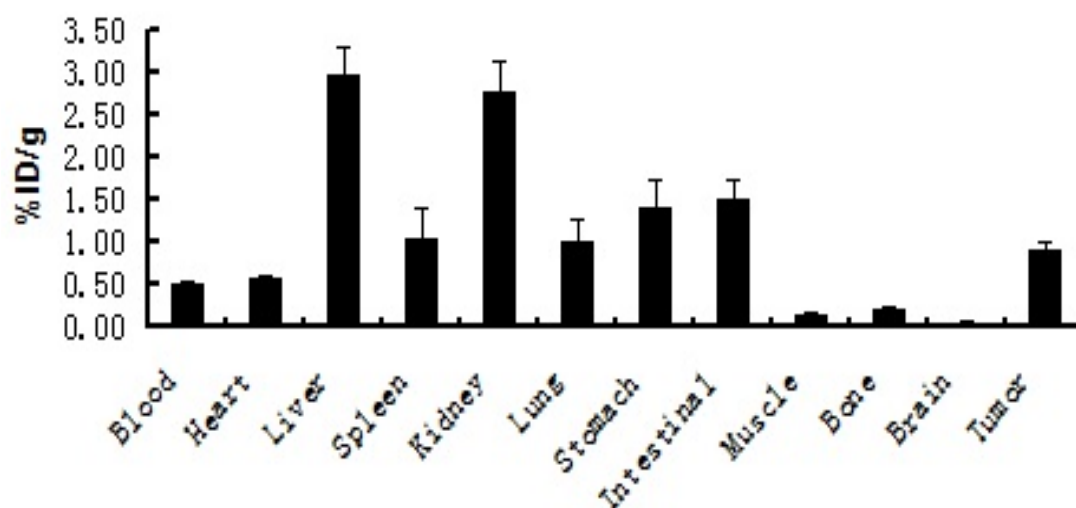
### 1.6 In vivo biodistribution

Figure 6A shows the biodistribution of  $^{64}\text{Cu}$ -DOTA-TNYL-RAW at 24 h after radiotracer administration in nude mice bearing PC-3M or A549 lung tumors. There was significantly higher uptake of  $^{64}\text{Cu}$ -DOTA-TNYL-RAW in PC-3M tumors than in A549 tumors (0.84 %ID/g vs. 0.44 %ID/g, SD 5 0.09 and 0.09, respectively,  $P < 0.000015$ ).

Figure 6B shows the biodistribution results of the mice bearing CT-26 tumor at 4 h post injection of  $^{64}\text{Cu}$ -DOTA-TNYL-RAW. The tumor The tumor-to-muscle ratio was reduced 56.7% in CT-26 tumors at 4 h and 47.6% in PC-3M tumors at 24 h after co-injected  $^{64}\text{Cu}$ -DOTA-TNYL-RAW with cold TNYL-RAW peptide compared with injection of  $^{64}\text{Cu}$ -DOTA-TNYL-RAW only (Fig. 6C).



**Figure 6A.** Biodistribution of  $^{64}\text{Cu}$ -DOTA-TNYL-RAW in mice bearing PC-3M and A549 tumors at 24 h after injection. Data are presented as %ID/g and are expressed as mean  $\pm$  SD (n =4). (Reprinted with permission of (90))



**Figure 6B.** Biodistribution of  $^{64}\text{Cu}$ -DOTA-TNYL-RAW in mice bearing CT-26 tumors at 4 h after injection. Data are presented as %ID/g and are expressed as mean  $\pm$  SD (n=4). (Reprinted with permission of (90))

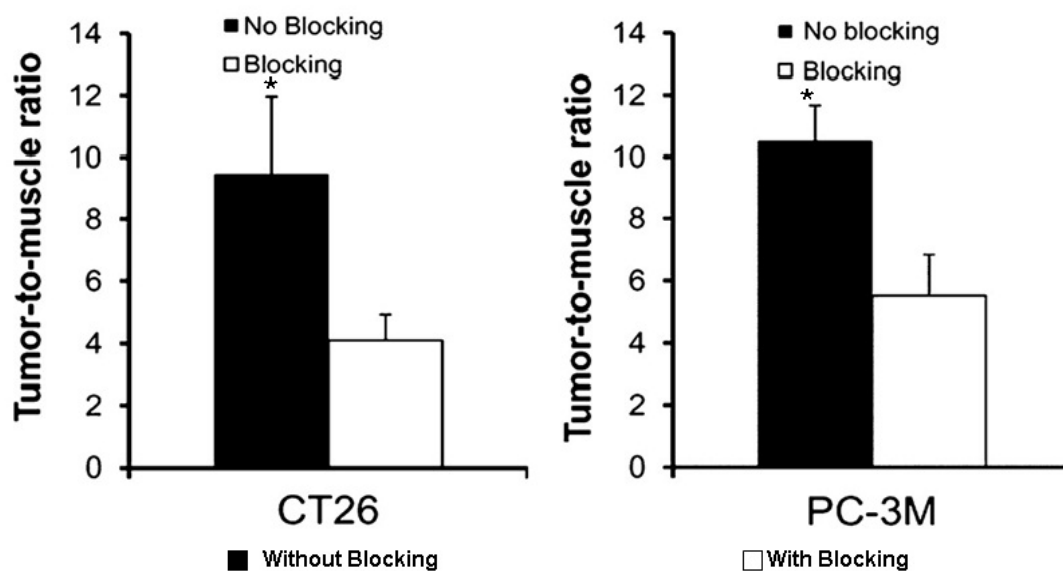


**Figure 6C.** Tumor-to-muscle-uptake ratio in mice bearing CT-26 or PC-3M tumors. In blocking group, mice were co-injected  $^{64}\text{Cu}$ -DOTA-TNYL-RAW (7.4 MBq [200  $\mu\text{Ci}$ ]) with cold TNYL-RAW peptide (20  $\mu\text{g}/\text{mouse}$ ). Data are presented as mean  $\pm$  SD (n=6). (Reprinted with permission of (90))

## 1.7 Immunofluorescence study on tumor sections

Immunofluorescence staining confirmed the expression of EphB4 on the CT26 and PC-3M tumors, but there was no expression of EphB4 receptor on A549 tumor cells. The ex vivo immunofluorescence results was similar to the pattern of *in vitro* binding study.

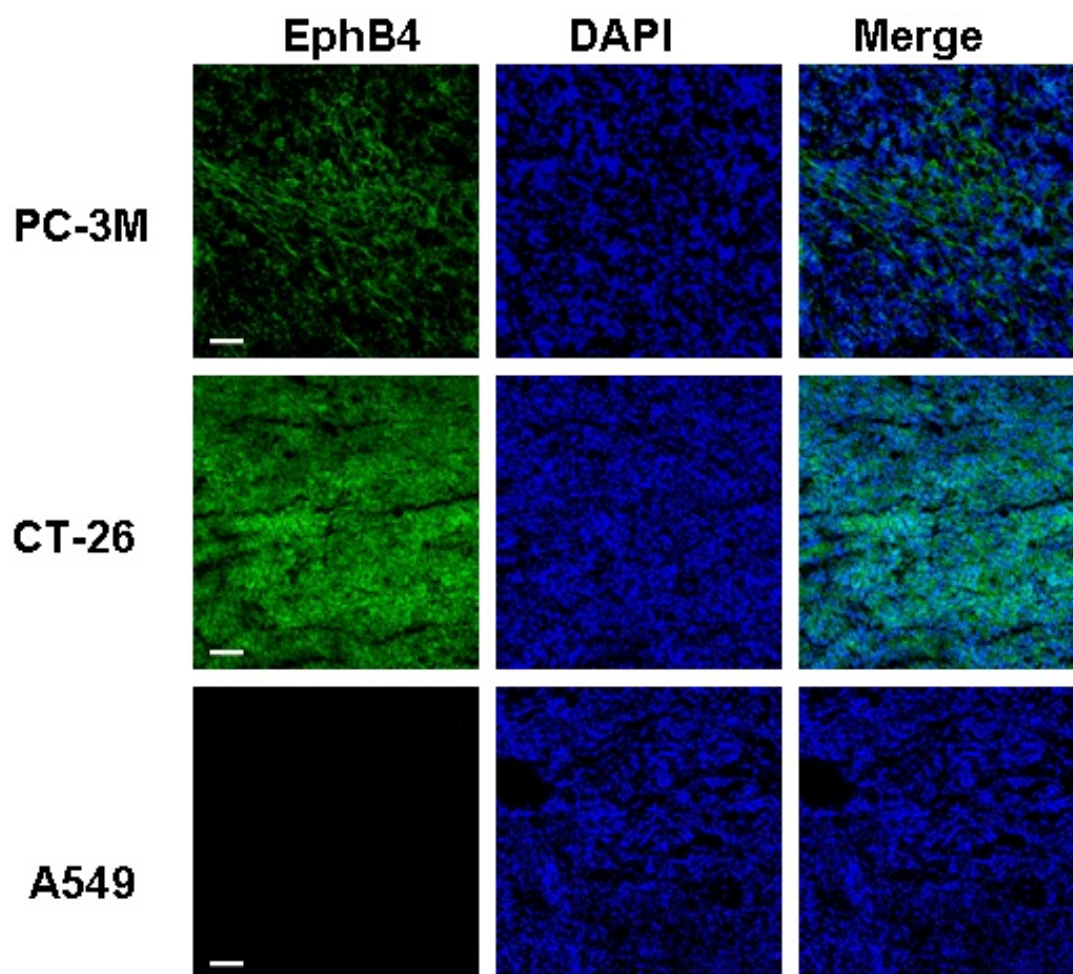


**Figure 7.** Immunofluorescence analysis of EphB4 expression in CT26, PC-3M, and A549 tumor sections excised after the imaging studies. Rabbit anti-human EphB4 antibody and goat anti-rabbit antibody conjugated with Alexa Flour 488 were used. Bar=100  $\mu$ m. (Reprinted with permission of (90))

## **2. Evaluate $^{64}\text{Cu}$ - and Cy5.5-labeled TNYL-RAW peptides for dual PET/optical imaging of EphB4 receptors in orthotopic glioma models**

### **2.1 Synthetic scheme of peptide Cy5.5-TNYL-RAW and Cy5.5-TNYL-RAWK-DOTA**

The peptide synthesis and introduction of Cy5.5 were carried out on solid phase (Figure 8A). For synthesis of Cy5.5-TNYL-RAW-DOTA, the DOTA was introduced in solution phase after cleavage of Cy5.5-TNYL-Raw peptide from the resin. After cleavage and purification of those peptide by HPLC, they were characterized by Electrospray ionization) mass spectrometry (ESI-MS).  $m/z$   $[\text{M}+\text{H}]^+ = 2604.0366$ ; calculated for Cy5.5-TNYL-RAW,  $\text{C}_{121}\text{H}_{159}\text{N}_{24}\text{O}_{33}\text{S}_4$ : 2604.0384 and  $m/z$   $[\text{M}+\text{H}]^+ = 3175.3224$ ; calculated for Cy5.5-TNYL-RAW-DOTA,  $\text{C}_{145}\text{H}_{200}\text{N}_{31}\text{O}_{42}\text{S}_4$ : 3175.3350. The radiochemical purity, defined as the ratio of the main product peak to all peaks, was determined by HPLC to be >95%. The specific activity of Cy5.5-TNYL-RAWK-DOTA- $^{64}\text{Cu}$  used in the *in vitro* and *in vivo* experiments was typically 7.4-14.8 MBq/nmol (0.2-0.4 Ci/ $\mu\text{mol}$ ) at the end of synthesis. The structure details of Cy5.5-TNYL-RAW and Cy5.5-TNYL-RAW –DOTA were shown in Fig 8B and 8C.

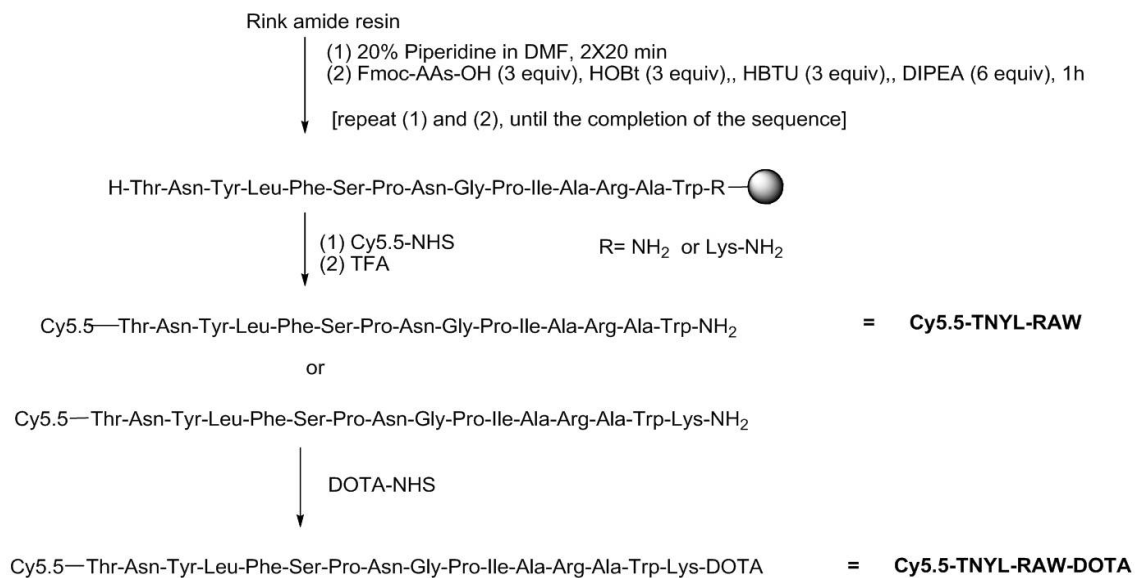


**Figure 8A.** Synthetic scheme of peptide Cy5.5-TNYL-RAW and Cy5.5-TNYL-RAWK-DOTA

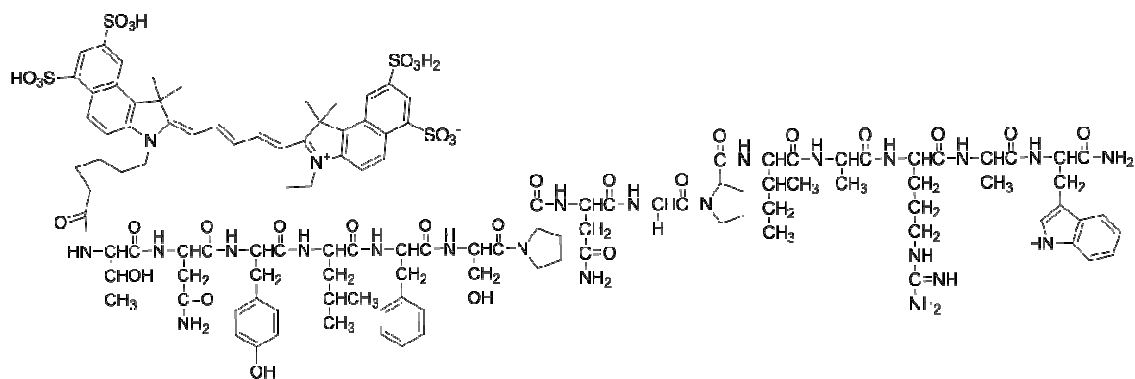


**Figure 8B.** Structure details of Cy5.5-TNYL-RAW

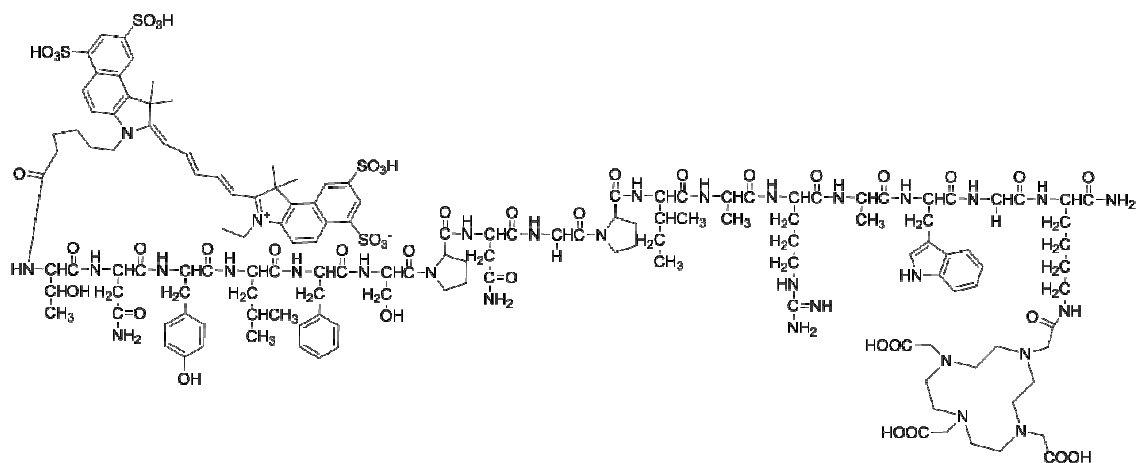


**Figure 8C.** Structure details of and Cy5.5-TNYL-RAWK-DOTA

## 2.2 Binding Affinity of Cy5.5-TNYL-RAW and Cy5.5-TNYL-RAWK-DOTA

Figure 9 shows representative sensorgrams obtained from SPR analyses of TNYL-RAW (Figure 1A), DOTA-TNYL-RAW (Figure 1A), Cy5.5-TNYL-RAW (Figure 8B), Cy5.5-TNYL-RAWK-DOTA (Figure 8C) and scrambled peptide, with fitting curves obtained using a global 1:1 mass transfer model. The corresponding binding kinetics and affinity data are summarized in Table 3. TNYL-RAW had a  $K_D$  of 3.06 nM. Conjugation of Cy5.5 to the N terminus and/or DOTA to the C terminus of the peptide didn't significantly change the  $K_D$  value of original TNYL-RAW peptide (1.27 nM and 1.01 nM respectively).



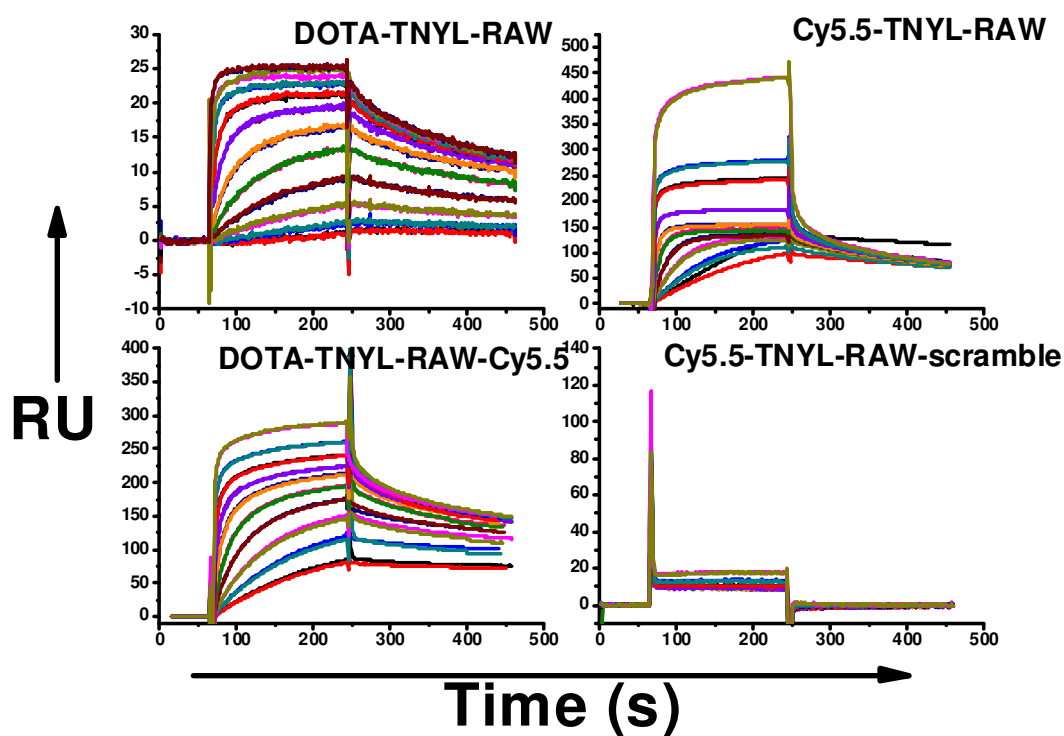


**Figure 9.** SPR sensorgrams of DOTA-TNYL-RAW, Cy5.5-TNYL-RAW, Cy5.5-TNYL-RAWK-DOTA and Cy5.5-scrambled peptide on sensor chips coated with EphB4. Peptides were injected as ten 2-fold-concentration series from 1.6 to 800 nM and were analyzed in duplicate binding cycles. Data sets (shown in black) are overlaid with curves fit to 1:1 mass transfer interaction model (red lines). Vertical axes in response units represent binding of each peptide to immobilized EphB4.

Analyte	$k_{on}$ [M <sup>-1</sup> s <sup>-1</sup> ]	$k_{off}$ [s <sup>-1</sup> ]	$K_D$ [M]	$\chi^2$
DOTA-TNYL-RAW	$1.1 \times 10^5$	$2.56 \times 10^{-3}$	$2.33^{-8}$	0.28
Cy5.5-TNYL-RAW	$4.15 \times 10^6$	$5.28 \times 10^{-3}$	$1.27^{-9}$	4.37
DOTA-TNYL- RAWK-Cy5.5	$1.86 \times 10^6$	$1.87 \times 10^{-3}$	$1.01^{-9}$	5.67
TNYL-RAW	$4.26 \times 10^5$	$1.3 \times 10^{-3}$	$3.06^{-9}$	0.155

**Table 3.** Association, Dissociation Rates and  $K_D$  of different TNYL-RAW peptides and derivatives interacting with immobilized EphB4 receptors obtained from SPR Analysis.

### 2.3 Detection of brain tumor growth by luciferase imaging

10 days after U87-Luc and U251-Luc tumor cells implanted in nude mice brain, Tumor burden as measured by luciferase activity was assessed using Xenogen IVIS-200 Optical in Vivo Imaging System. Figure 10 clearly showed the luciferase activity in the brain area of the nude mice in both tumor models, and there is no other detectable signal in spinal cord area, which confirmed that the tumors were successfully grown in the.

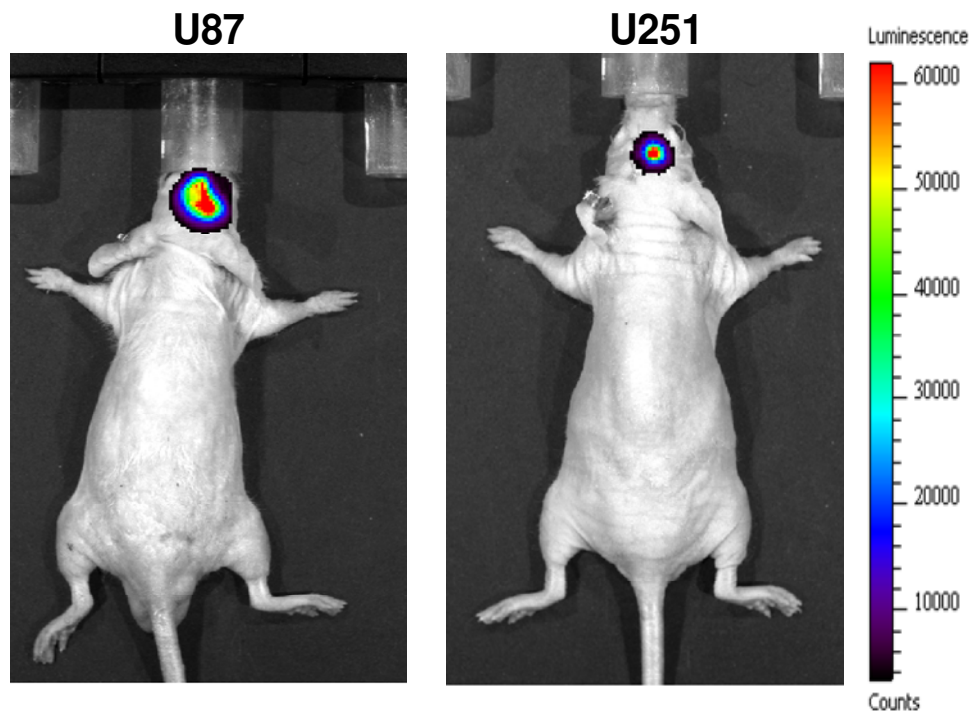


**Figure 10.** Representative Lucifase imaging of U251 and U87 glioblastoma on orthotopic mice. Figure 10 shows luciferase signal of U251 and U87 10 days after tail vein injection of luciferin.

## 2.4 Optical Imaging of U251 and U87 tumors in the brain

Figure 11A showed Cy5.5 optical imaging of U251 and U87 tumor in the brain. 24 hours after tail vein injection of Cy5.5-TNYL-RAW-DOTA, U87 or U251 tumor implanted in nude mice brain was clearly visualized. To confirm the specific uptake of Cy5.5-TNYL-RAW-DOTA to tumor, Cy5.5 conjugated scrambled peptide was used. In figure 11B, U87 tumors in the brain of nude mice were clearly seen on optical imaging at 1 h, 4 h and 24 h time point after tail vein injection of Cy5.5-TNYL-RAW-DOTA, but there was little signal being detected in the nude mice brain after tail vein injection of Cy5.5-scramble peptide at same time points.

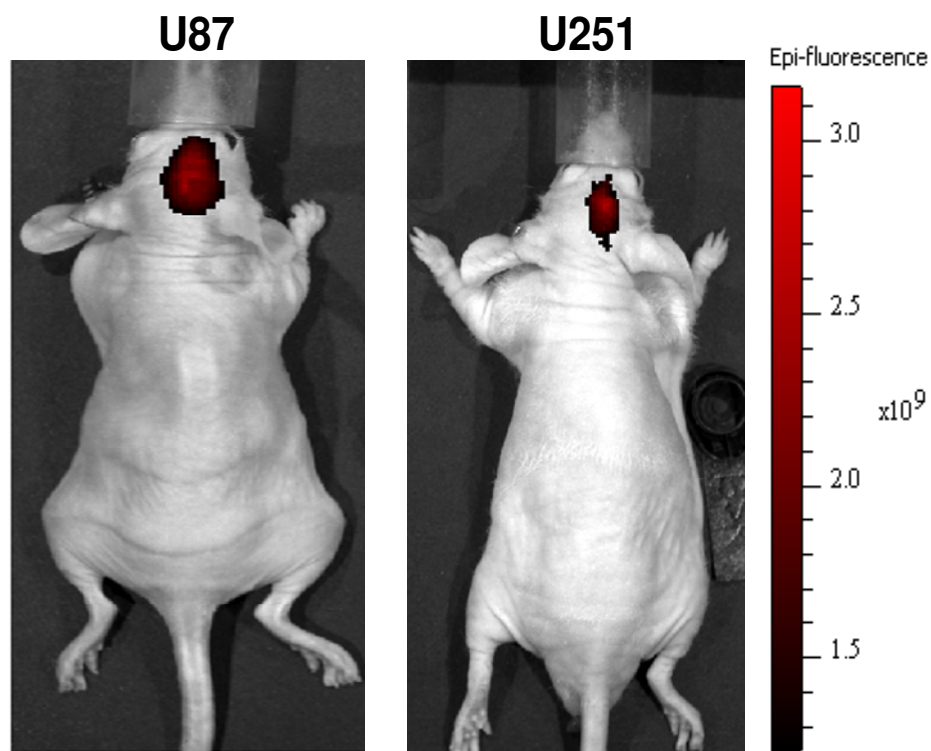


**Figure 11A.** Representative Cy5.5 optical imaging of U251 and U87 glioblastoma on orthotopic mice. Cy5.5 near-infrared fluorescence optical imaging U251 and U87 tumors 24 hours after tail vein injection of  $^{64}\text{Cu}$ -Cy5.5-TNYLRAW-DOTA.

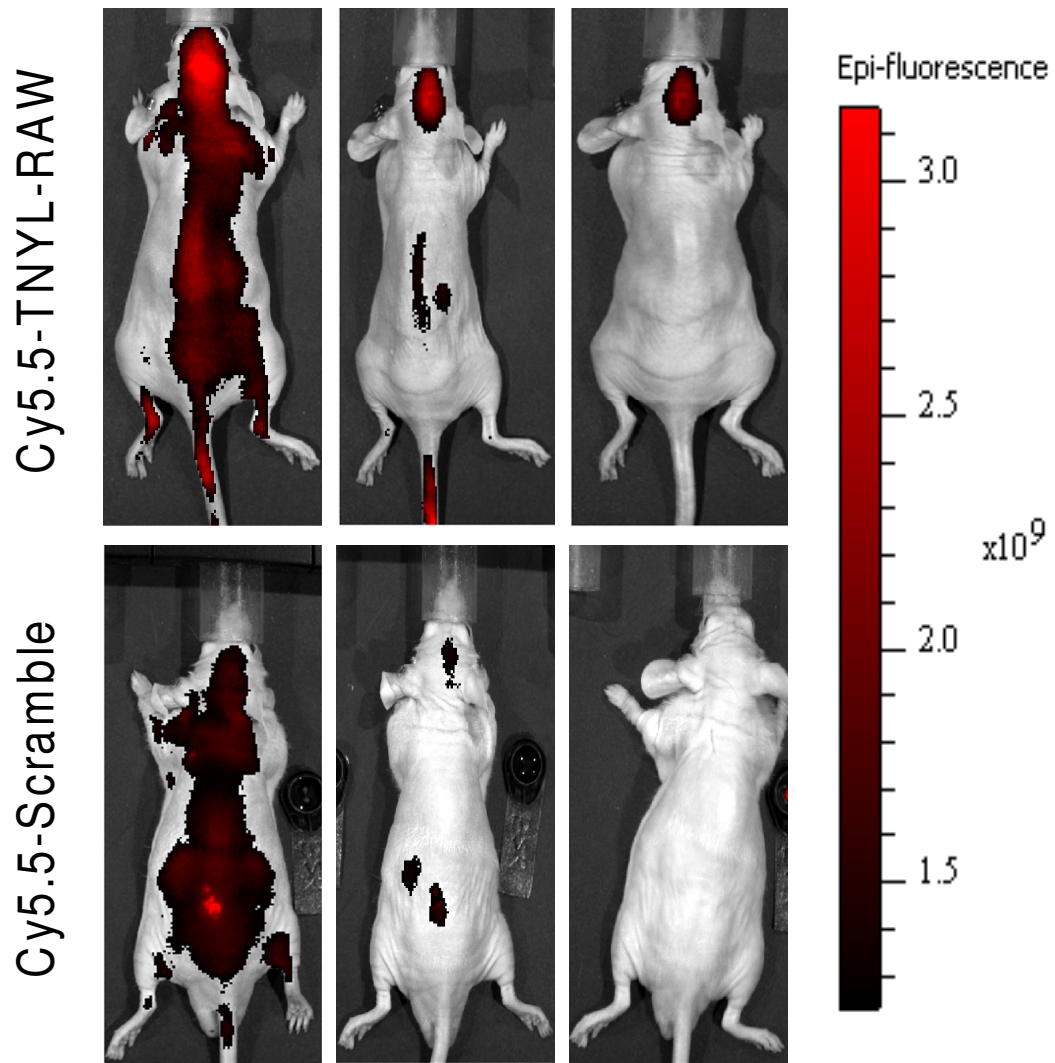


**Figure 11B.** Representative near-infrared (NIR) fluorescence optical images of U87 after tail vein injection of Cy5.5-TNYLRAW-DOTA or Cy5.5-scramble, imaging taken at various time points. Figure 11B upper panel shows the NIR optical imaging of U87 tumors at 1h, 4h and 24 hours after tail vein injection of Cy5.5-TNYLRAW-DOTA. Figure 10B lower panel shows the NIR optical imaging of U87 tumors at 1h, 4h and 24 hours after tail vein injection of Cy5.5-scramble peptides.

## **2.5 Ex vivo analysis of the fluorescence signal intensities of dissected tissues**

Figure 12A and 12B shows the biodistribution of Cy5.5-TNYL-RAW-DOTA or Cy5.5-scramble-DOTA in mice bearing U87 tumors by ex vivo analysis of the fluorescence signal intensities of dissected tissues. High fluorescence activity was found in mice liver, kidney, stomach and intestine. Compared with fluorescence densities in two groups at different time points, it clearly showed that U87 tumor has significantly higher uptake of Cy5.5-TNYL-RAW-DOTA than that of Cy5.5-scramble-DOTA did.

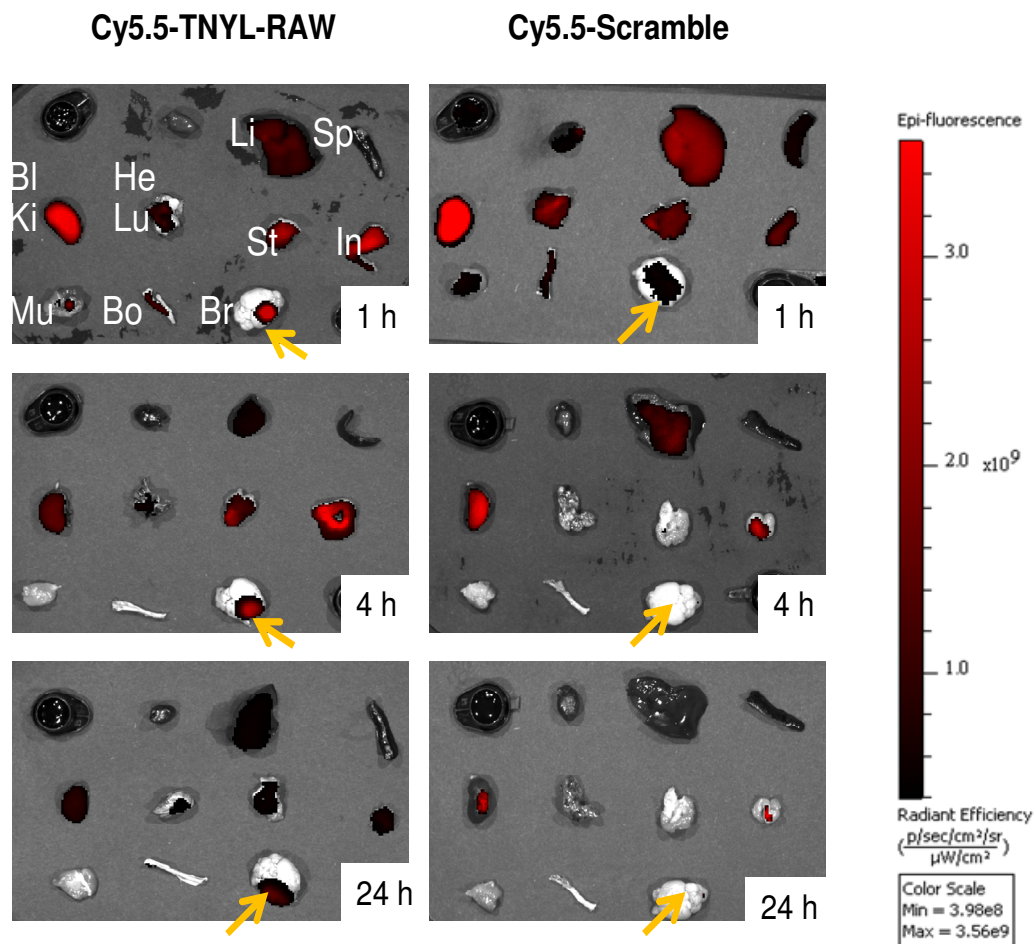


**Figure 12A.** Representative near-infrared (NIR) fluorescence optical images of various tissues obtained from the mouse at the end of the imaging sessions. Images were taken at 1h, 4h and 24 hours after *i.v.* injection of  $^{64}\text{Cu}$ -Cy5.5-TNYL-RAW-DOA or  $^{64}\text{Cu}$ -Cy5.5-scramble peptides.

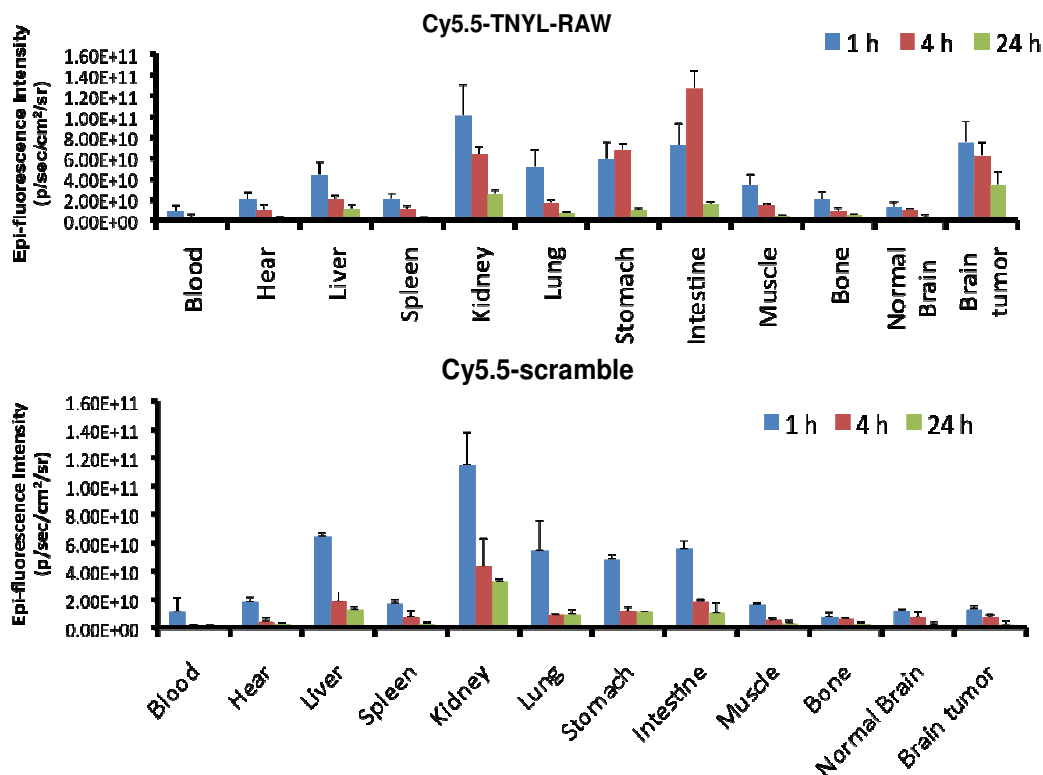


**Fig 12B.** Biodistribution at 24h after i.v. injection of different peptides, obtained using the fluorescence intensity measurement method, plotted as photon flux per gram of tissue. All data are expressed as mean  $\pm$  standard deviation (n=4).

## 2.6 Nuclear Imaging of tumors in the brain

Figure 13A shows small-animal PET/CT of both coronal and transverse slices that contain U87 tumor. Tumors were clearly visualized at 1 and 24 h after tail vein injection  $^{64}\text{Cu}$ -Cy5.5-TNYLRAW-DOTA. Figure 13B compares small-animal PET/CT images obtained in the presence and absence of a large excess of cold Cy5.5-TNYLRAW (50  $\mu\text{g}/\text{mouse}$ ) at 1h and 24h after radiotracer injection in U251 tumor bearing mice. AT 1h and 24 h after injection of radiotracer, the U251 tumors were clearly visualized compared with barely detectable signal in blocking group. In U251 tumor models, the co-administration of cold Cy5.5-TNYL-RAW-DOTA caused a 57% reduction in the



ratio of  $^{64}\text{Cu}$ -Cy5.5-TNYLRAW-DOTA accumulations in tumors versus normal brain based on tumor voxel intensity calculation from PET/CT image (Figure 13C).

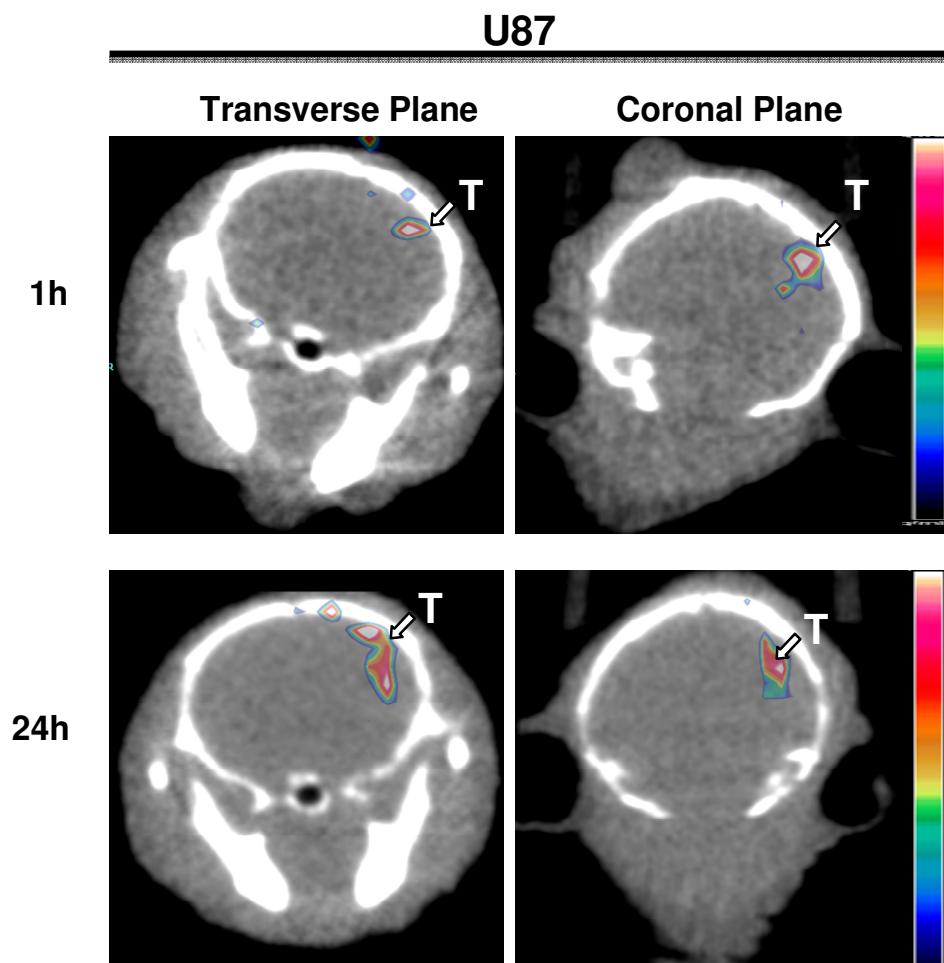


**Figure 13A.** Micro PET/CT images of mice bearing a U87 after intravenous administration of  $^{64}\text{Cu}$ -labeled Cy5.5-TNYL-RAW-DOTA. The mice bearing a U87 tumor received  $^{64}\text{Cu}$ -labeled Cy5.5-TNYL-RAW-DOTA.

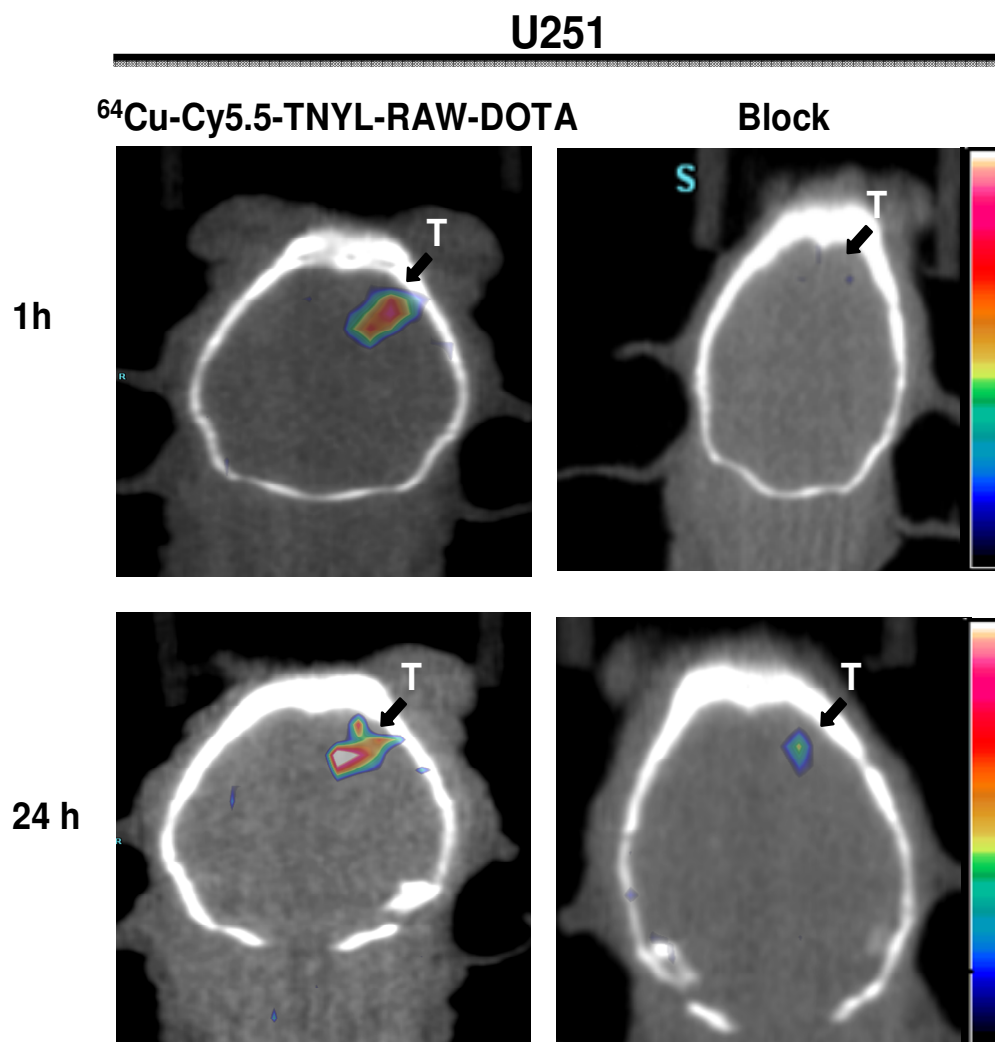


**Figure 13B.** Micro PET/CT images of mice bearing a U251 after intravenous administration of <sup>64</sup>Cu-labeled Cy5.5-TNYL-RAW-DOTA. The mice bearing a U251 tumor received <sup>64</sup>Cu-labeled Cy5.5-TNYL-RAW-DOTA or excess amount of cold Cy5.5-TNYL-RAW-DOTA peptide as blocking group.

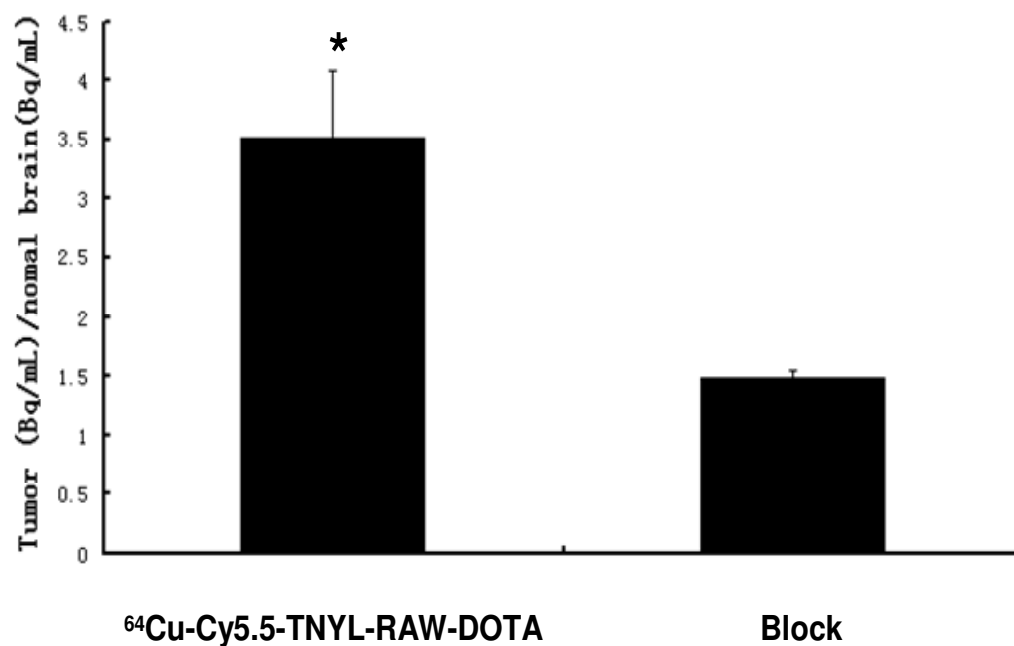


**Figure 13C.** Compared tumor voxel intensity / normal brain voxel intensity between  $^{64}\text{Cu}$ -labeled Cy5.5-TNYL-RAW-DOTA and blocking group based on calculation from an irregular 3-dimensional region of interest (ROI) manually drawn corresponding to PET images. \* Indicates p value < 0.05

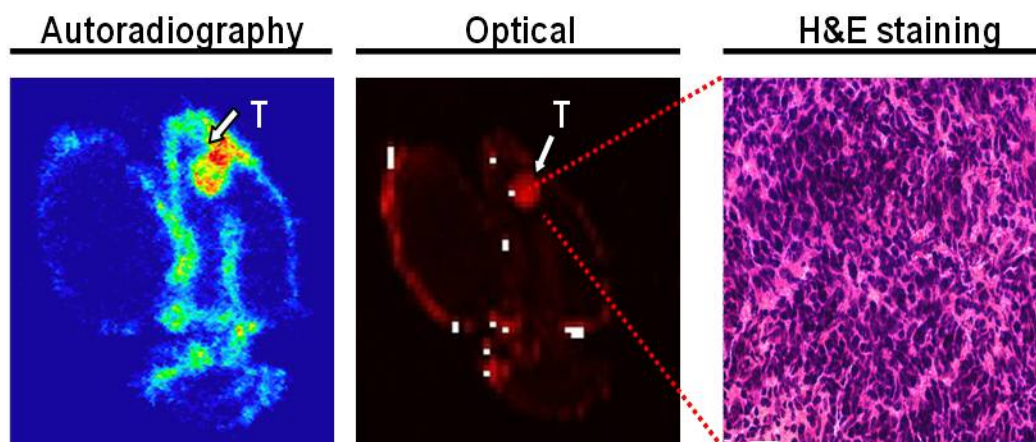


**Figure 13 D.** Representative autoradiograph, fluorescence and H&E staining images of excised brain tissue containing U251 tumors.

## 2.7 Immunohistochemistry

Figure 14 shows the immunofluorescence results of the expression of EphB4, binding site of Cy5.5 labeled TNYL-RAW peptide on mice brain section containing implanted tumor. In figure 14 upper panel, expression of EphB4 (green color) was detected on both U251 tumor cells and tumor associated blood vessel (red color CD31 staining). The binding of  $^{64}\text{Cu}$ -Cy5.5-TNYL-RAW-DOTA was also correlated with EphB4 expression on tumor section, which was also detected on both tumor cells and tumor associated vessels. From figure 14 lower panels, the expression of EphB4 was only detected on tumor-associated blood vessel but not on tumor cells, which was also corresponding to  $^{64}\text{Cu}$ -Cy5.5-TNYL-RAW-DOTA binding site on tissue sections.

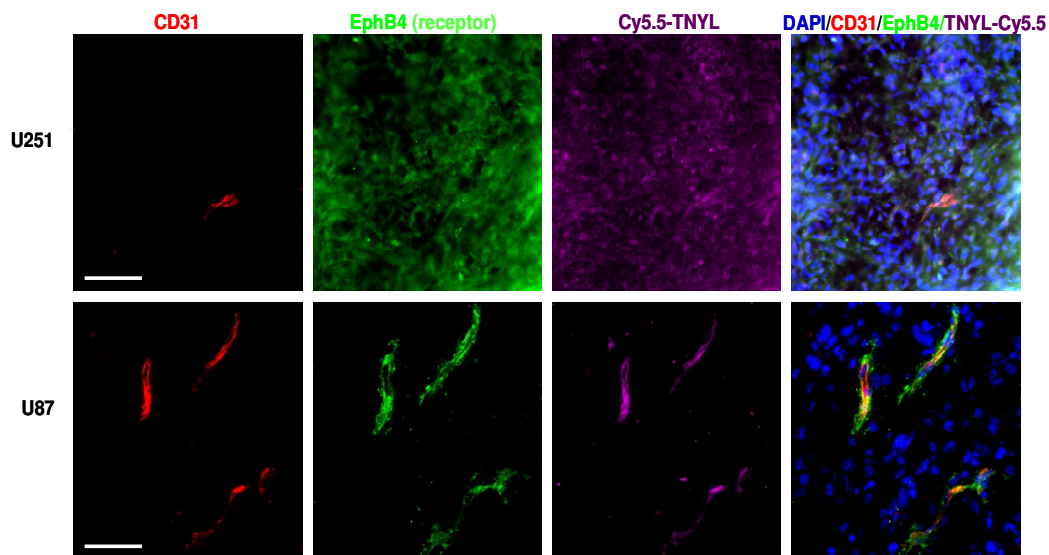


**Figure 14.** Fluorescence microscopy of mice brains including implanted U87 or U251 tumors excised after imaging studies. The mice bearing a U251 or U87 tumor were injected intravenously with  $^{64}\text{Cu}$ -labeled Cy5.5-TNYL-RAW-DOTA peptides. Signal from Cy5.5-loaded TNYL-RAW-DOTA was pseudocolored purple. EphB4 (green) was stained with rabbit anti-human EphB4 antibody and Alexa Flour 488-conjugated goat anti-rabbit immunoglobulin. CD31 (red), which is the marker of the endothelial cells of tumor associated vessel were stained with rat anti-mouse CD 31 antibody and Alexa flour 594-conjugagted donkey anti-rat antibody. Cell nuclei were counterstained with DAPI (blue). Bar=100  $\mu\text{m}$ .

### 3. To develop and evaluate EphB4 specific peptide conjugated HAuNS for photothermal ablation therapy of colon cancer *in vitro* and *vivo*

#### 3. 1 Synthesis and Characterization of TNYL-PEG-HAuNS

The structure of TNYL-PEG-SATA peptide was shown in Figure 15 A. The reaction scheme of the conjugation of TNYL-PEG-SATA peptide the surface of HAuNS is shown in Figure 15B. Figure15C is the resonance absorbance of these different AuNS particles. This data showed that there were no significant changes in the resonance absorbance of HAuNS after conjugation with TNYL-PEGS-SATA or PEG-SH. The absorbance peaks of different HAuNS solutions are still around at 800nm which is suitable for photothermal therapy at near infrared region. Calculation of the number of

peptide per particle was based on the result of amino acid analysis from the core facility in Baylor College of Medicine. Each particle has approximate 40 peptides coupling on its surface. As confirmed by instant thin-layer chromatography, the radiolabeling purity of TNYL-PEG-HAuNS was about 98% after purification by centrifuge.

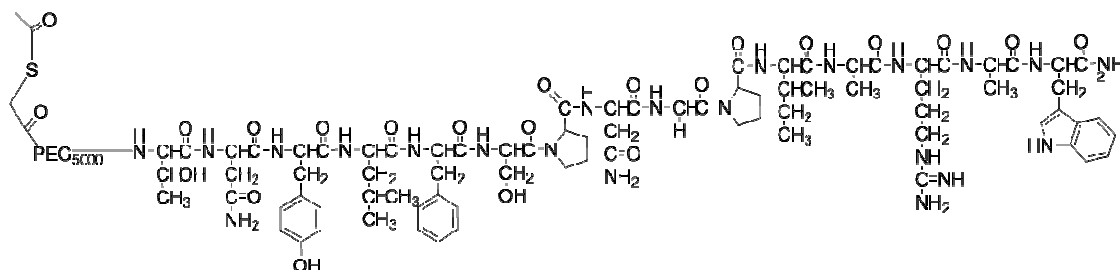


**Figure 15A.** structure details of TNYL-PEG-SATA

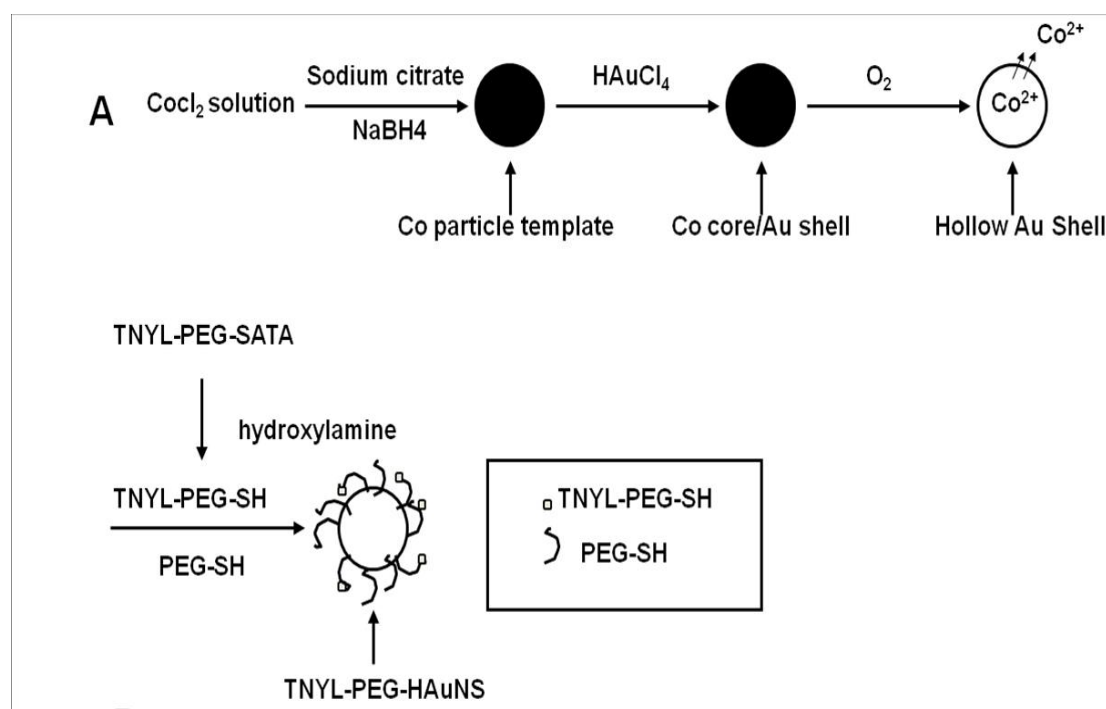


**Figure 15B.** Reaction scheme for the conjugation of TNYL-PEG-SATA to HAuNS.

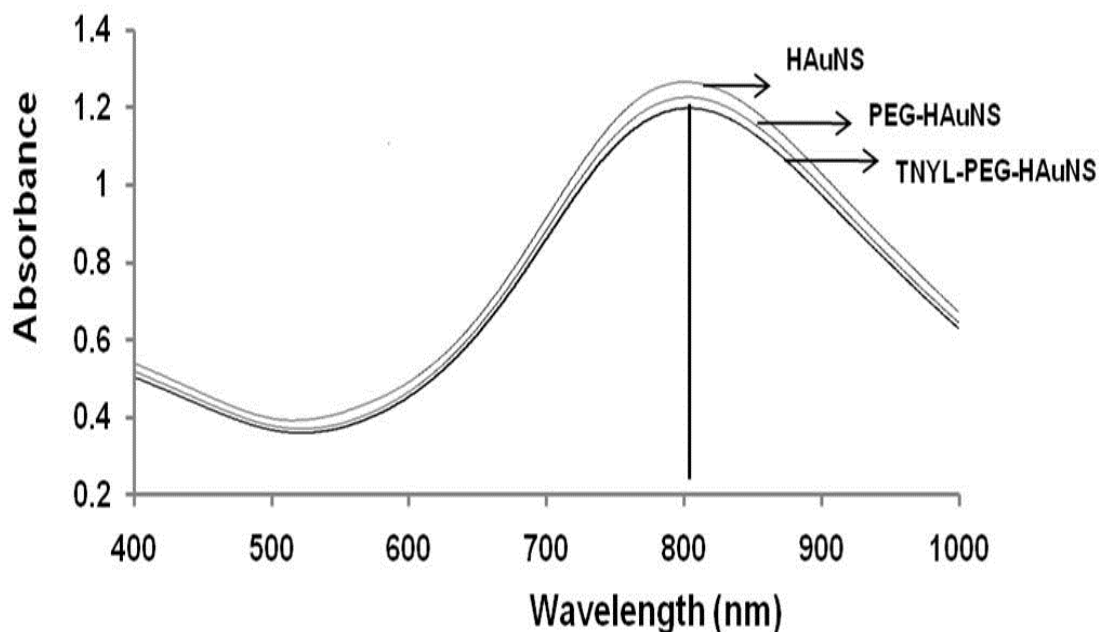


**Figure 15C.** The resonance absorbance of these different HAuNS particles (AuNS, PEG-HAuNS, TNYL-PEG-HAuNS)

## Colon and prostate cancer model for photothermal therapy

### 3.2 Fluorescence and dark field microscope

EphB4 receptors are overexpressed in PC-3M and CT-26 cells [38]. Figure 16 shows the dark field images of PC-3M human prostate cancer cells and CT26 murine colon cancer cells incubated with TNYL-PEG-HAuNS. The uptake of TNYL-PEG-HAuNS was high in EphB4-positive PC-3M and CT-26 cells, while there was very low uptake of PEG-HAuNS in both cells, suggesting that the high uptake of the TNYL-PEG-HAuNS was mediated through EphB4. Moreover, the specific uptake of TNYL-PEG-HAuNS in PC-3M and CT-26 cells could be efficiently blocked by excessive amount of TNYL-PEG-SATA peptides

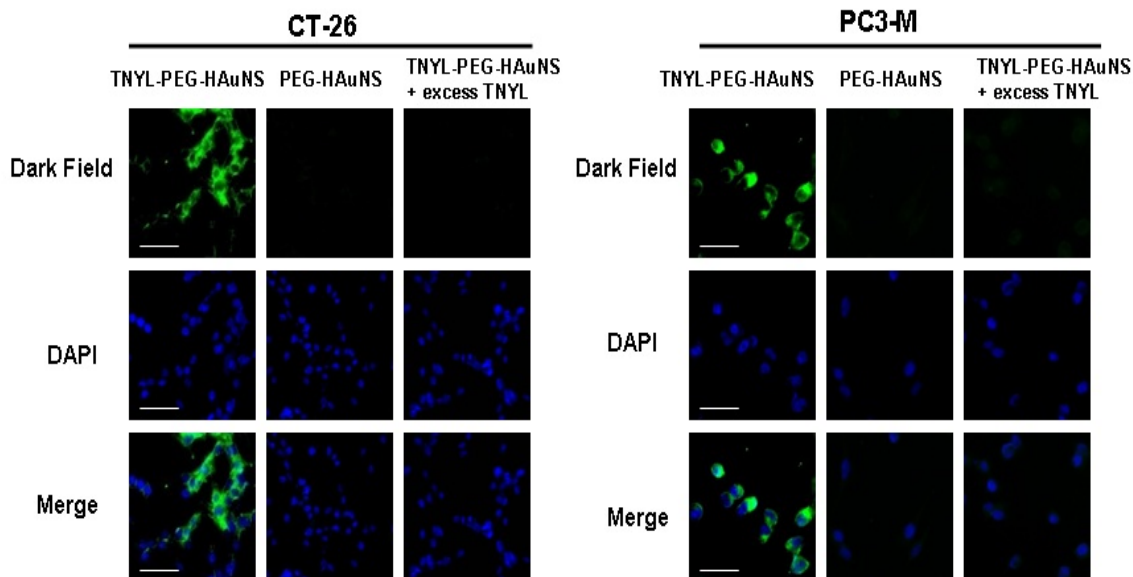


**Figure 16.** Fluorescence microphotographs (dark field) and radioactive uptake study of EphB4-positive PC-3M and CT-26 cancer cells after incubation with TNYL-PEG-HAuNS or PEG-HAuNS. Representative fluorescence and dark field microphotographic images. In right panel, PC-3M cells were incubated with TNYL-PEG-HAuNS (left upper) for 2 h; PC-3M cells were incubated with PEG-HAuNS (left middle) for 2 h; PC-3M cells were co-incubated with TNYL-PGL-HAuNS and excess amount of TNYL-PEG (Left lower) for 2 h. In left panel, CT-26 cells were incubated with TNYL-PEG-HAuNS (left upper) for 2 h; CT-26 cells were incubated with PEG-HAuNS (left middle) for 2 h; CT-26 cells were co-incubated with TNYL-PGL-HAuNS and excess amount of TNYL-PEG (Left lower) for 2 h. Signal from dark field is pseudocolored green. Cell nuclei were counterstained with DAPI (blue). Scale bar=50  $\mu$ m.



### 3.3 In vitro radioisotope binding assay

Cell uptake of TNYL-PEG-HAuNS was also evaluated by the radioactivity count method, and the result was consistent with the results obtained by dark field fluorescence microscopy. PC-3M cells and CT-26 showed significantly higher uptake of  $^{64}\text{Cu}$ -labeled TNYL-PEG-HAuNS than the uptake of  $^{64}\text{Cu}$ -labeled PEG-HAuNS (Figure 17). The above cell binding results confirmed that TNYL-PEG-HAuNS can specifically bind to EphB4 positive cancer cells.

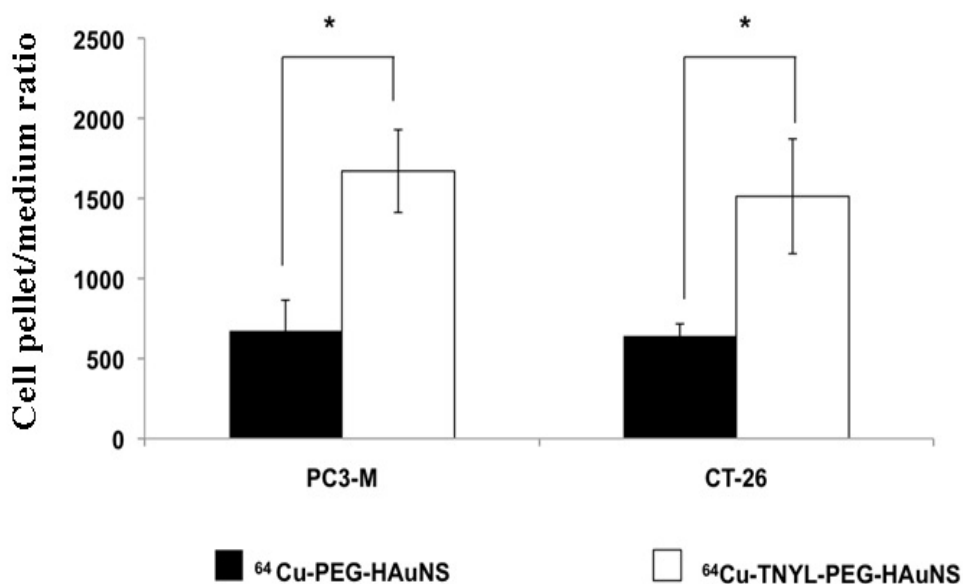


**Figure 17.** Radioactive uptake study of cells incubated with  $^{64}\text{Cu}$  labeled TNYL-PEG-HAuNS or PEG-HAuNS. PC-3M cells (left) were incubated with  $^{64}\text{Cu}$  labeled TNYL-PEG-HAuNS (dark gray) or TNYL-HAuNS (light gray) for 2 h; CT-26 cell (right) were incubated with  $^{64}\text{Cu}$  labeled TNYL-PEG-HAuNS (dark gray) or TNYL-HAuNS (light gray) for 2 h. The data were expressed as cpm/ $\mu\text{g}$  protein in cell pellet over cpm/ $\mu\text{g}$  medium and presented as mean  $\pm$  standard deviation (n=5). \* Indicates statistically significance with  $P < 0.01$

### 3.4 In vitro photothermal ablation of cancer cells

To compare the photothermal effect of TNYL-PEG-HAuNS with original HAuNS and PEG-HAuNS, above three nanoparticle solutions were exposed to an  $8 \text{ W/cm}^2$  near infrared-region laser respectively. The temperature of all solutions was increased from  $27^\circ\text{C}$  to  $75^\circ\text{C}$  at the concentration of  $4 \times 10^{11}$  particles/mL. There was no significant difference in the changes of temperature among these nanoparticles (Figure 18). These data suggested that HAuNS still can be an efficient photothermal coupling agent after conjugation with TNYL-PEG-SATA or PEG-SH. Figure 18 and 19 show that most of PC3-M and CT-26 cells treated with TNYL-PEG-HAuNS plus NIR laser irradiation ( $40 \text{ W/cm}^2$  for 5 min) were not stained by calcein AM dye but stained for Eth-D1, which suggested that majority of cells were dead after NIR laser treatment. In contrast, cell viability has no changes after treatment of PEG-HAuNS plus laser, and laser only. The photothermal killing ability of TNYL-PEG-HAuNS was significantly abolished after adding excess amount of TNYL-PEG-SATA.

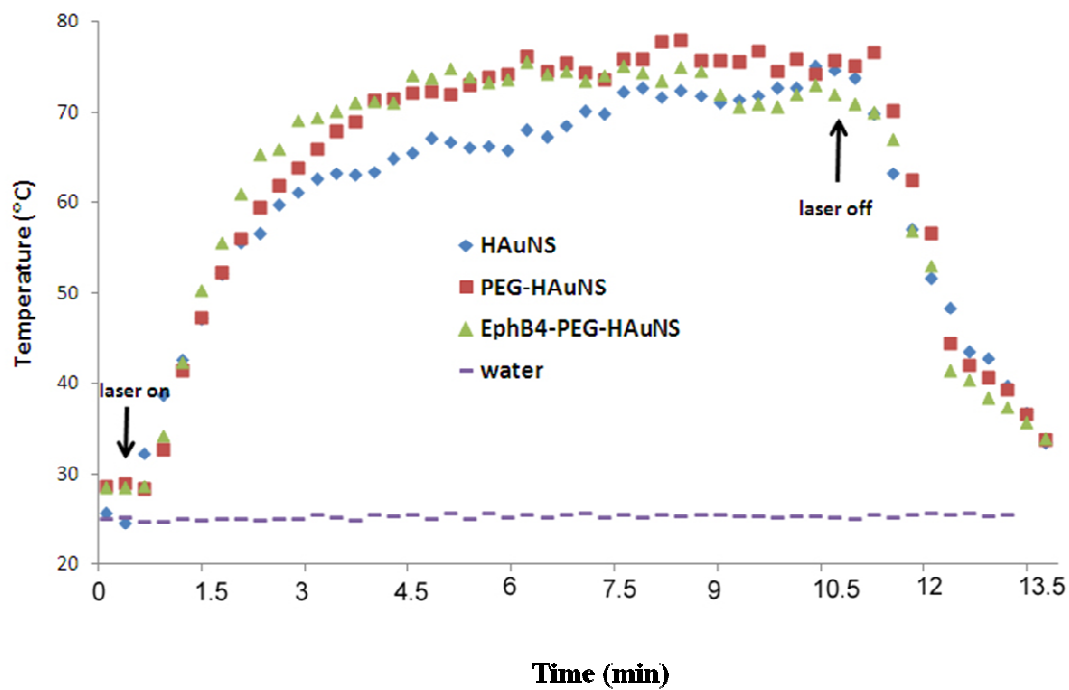


**Figure 18.** Heating of aqueous TNYL-PEG-HAuNS, PEG-HAuNS or HAuNS solutions exposed to NIR light centered at 808 nm at 8 W/cm<sup>2</sup>.

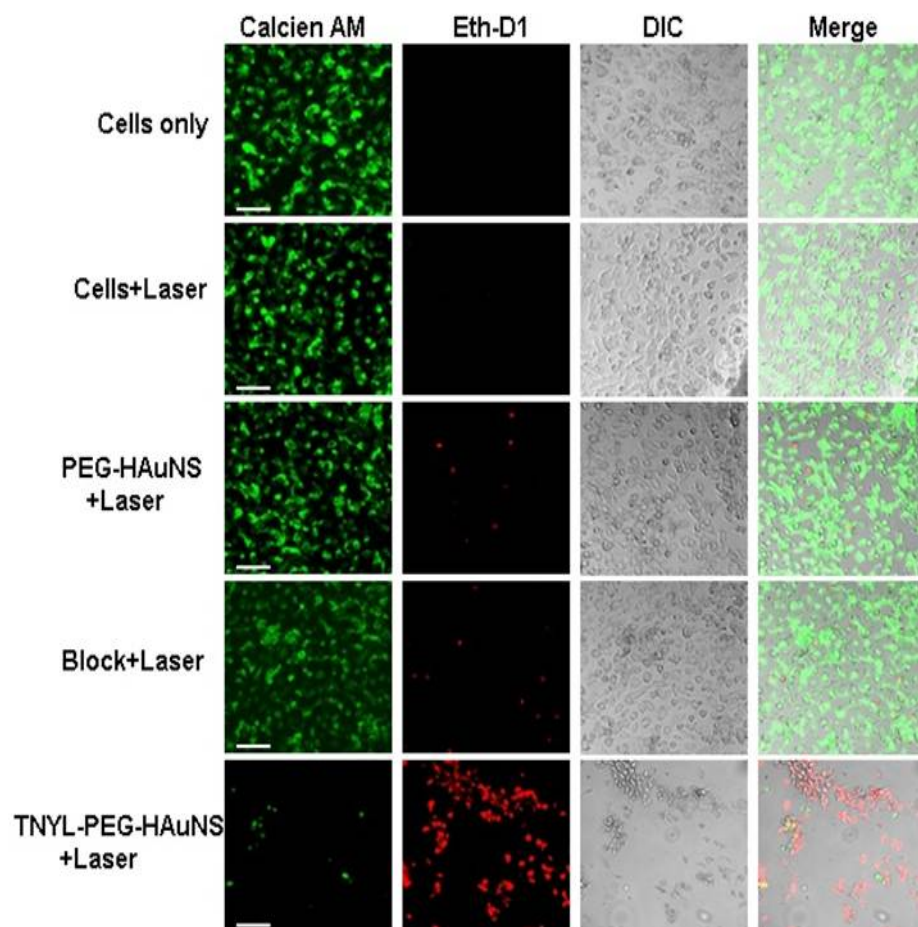


**Figure 19.** CT-26 cells viability after various treatments, most of cells were dead after treatment with TNYL-PEG-HAuNS plus NIR laser. Live cells were stained with calcein AM and dead cells were stained for Eth-D1. Scale bar=100  $\mu$ m.

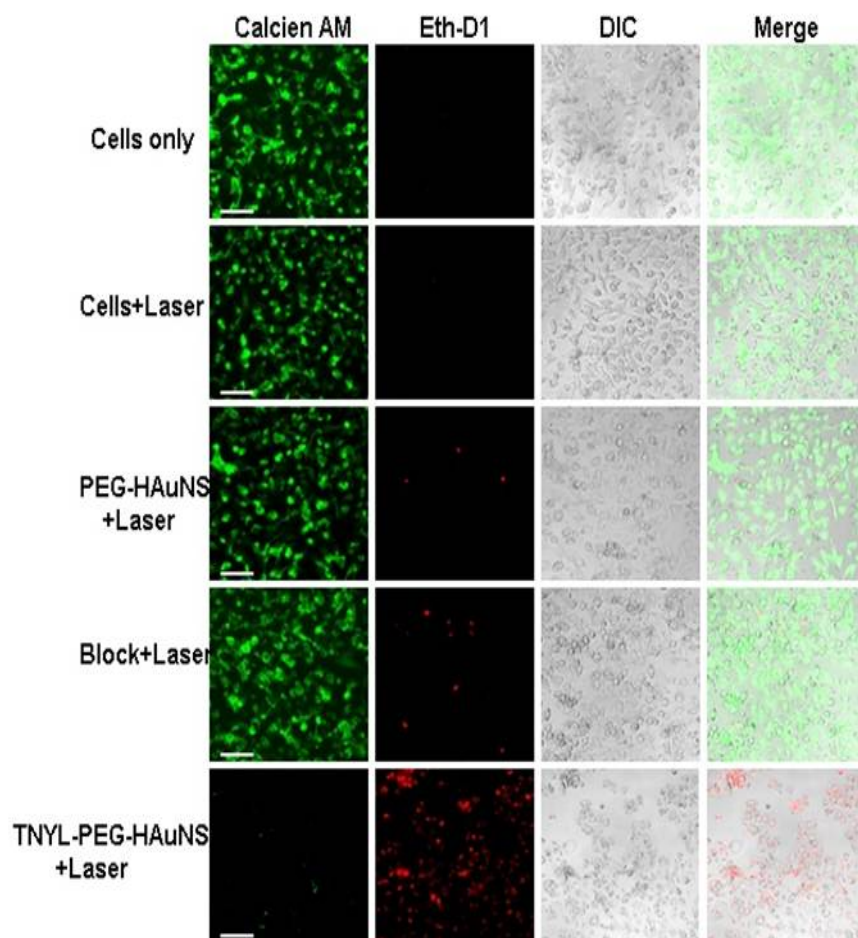


**Figure 20.** PC-3M cells viability after various treatments. Most of cells were dead after treatment with TNYL-PEG-HAuNS plus NIR laser. Live cells were stained with calcein AM and dead cells were stained for Eth-D1. Scale bar, 100  $\mu$ m.

### 3.5 Micro-PET Imaging

Figure 21 showed the micro-PET images of the mice bearing CT-26 tumors acquired at 1, 6, and 24 h after intravenous injection of  $^{64}\text{Cu}$ -TNYL-PEG-HAuNS or  $^{64}\text{Cu}$ -PEG-HAuNS. Micro-PET images revealed that the uptake of  $^{64}\text{Cu}$ -TNYL-PEG-HAuNS in the tumor was gradually accumulated from 1 h to 24 h. The tumor was clearly visualized at 24 h after the injection of  $^{64}\text{Cu}$ -TNYL-PEG-HAuNS. There were fewer signals detected in the tumors of mice injected with  $^{64}\text{Cu}$ -PEG-HAuNS.

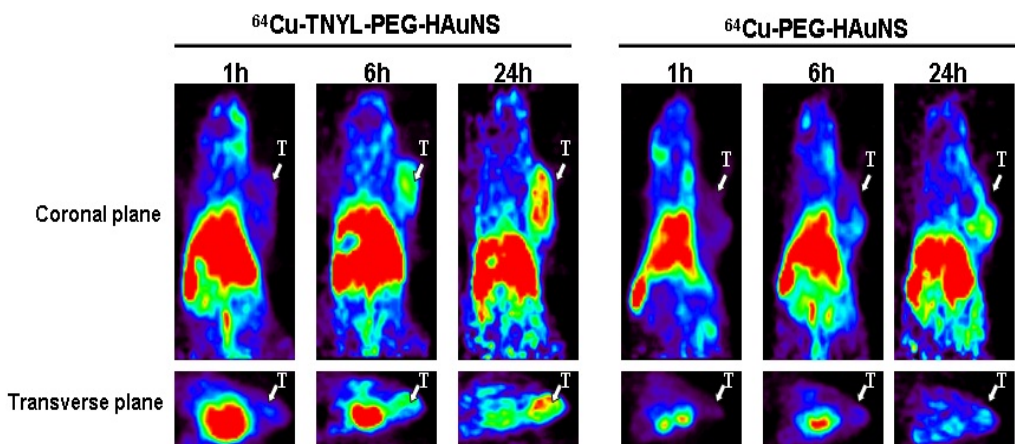


**Figure 21.** Micro PET imaging of mice bearing a CT-26 tumor after intravenous injection of  $^{64}\text{Cu}$  labeled TNYL-PEG-HAuNS or TNYL-HAuNS. The mice bearing a CT-26 tumor were administration of  $^{64}\text{Cu}$  labeled TNYL-PEG-HAuNS or PEG-HAuNS. Representative micro PET images at 1h, 6h, and 24h after tail vein i.v. injection of  $^{64}\text{Cu}$  labeled TNYL-PEG-HAuNS and Representative micro PET images at 1h, 6h, and 24h after tail vein i.v. injection of  $^{64}\text{Cu}$  labeled PEG-HAuNS.

### 3.6 In vivo biodistribution

The biodistribution data described in Figure 22 are consistent with the micro-PET imaging results. At 24 h after injection, uptake of  $^{64}\text{Cu}$ -TNYL-PEG-HAuNS (4.92% ID/g) in CT-26 tumors was significantly higher than  $^{64}\text{Cu}$ -PEG-HAuNS (1.49% ID/g) ( $P < 0.001$ ). The ratio of tumor-to-muscle in the mice injected with  $^{64}\text{Cu}$ -TNYL-PEG-HAuNS (25.9) was four times higher than that in the mice injected with  $^{64}\text{Cu}$ -PEG-HAuNS (6.2). The ratio of tumor-to-blood in the mice injected with  $^{64}\text{Cu}$ -TNYL-PEG-HAuNS (2.94) was 1.5 times higher than that in the mice injected with  $^{64}\text{Cu}$ -PEG-HAuNS (2.0).

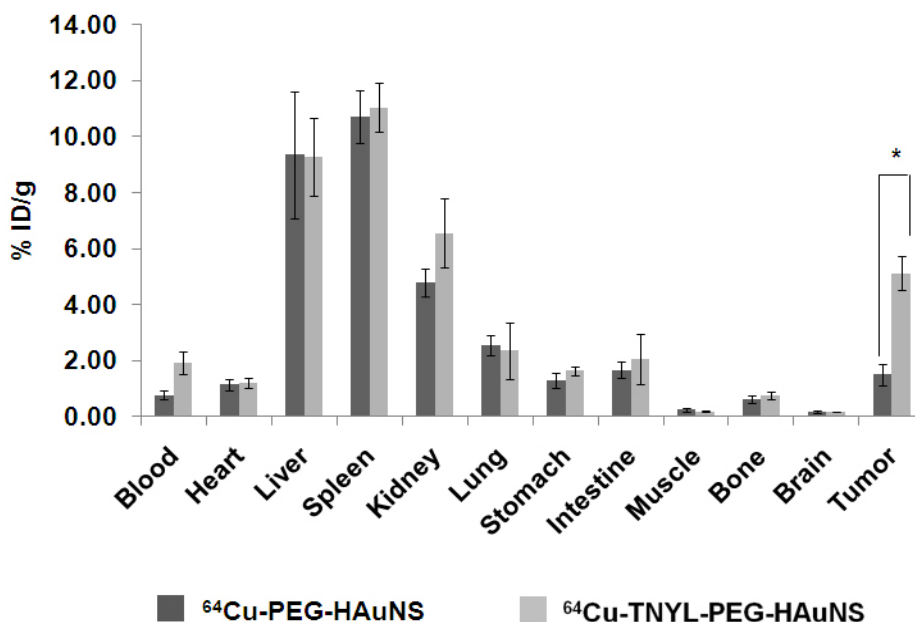


**Figure 22.** *In vivo* biodistribution and tumor uptake of  $^{64}\text{Cu}$  labeled TNYL-PEG-HAuNS or PEG-HAuNS in mice bearing a CT-26 tumor, 24 h after intravenous injection. The mice bearing CT-26 tumor received  $^{64}\text{Cu}$  labeled TNYL-PEG-HAuNS light (light gray), or  $^{64}\text{Cu}$  labeled PEG-HAuNS (dark gray).

### 3.7 In Vivo Photothermal Therapy

Mice bearing CT-26 tumor were treated with TNYL-PEG-HAuNS, PEG-HAuNS ( $2 \times 10^{12}$  per mouse, 200  $\mu$ L) or saline (as control 200  $\mu$ L). 24 h after injection, the tumors were treated with NIR irradiation. The skin at the tumor sites in mice that received intravenous injection of TNYL-PEG-HAuNS turned brownish, indicating tissue burns caused by the local photothermal effect. In contrast, there were less color changes (turned into a little white) in the skin of mice treated with PEG-HAuNS plus laser. There was no color changes in the skin of mice treated with saline plus NIR irradiation, or NIR laser alone (Figure. 23A). Histological examination of tissue slides cut from tumor confirmed that the intravenous injection of TNYL-PEG-HAuNS followed by laser treatment caused significantly greater thermonecrotic response than PEG-HAuNS plus laser treatment, saline plus laser treatment, or saline only did (Figure. 23B). In the mice treated with TNYL-PEG-HAuNS plus the laser, (Figures 23B and C), majority of tissues (82% of tissues) were necrotized, prominent features of thermonecrosis were found, such as karyolysis, cytoplasmic acidophilia, and corruption and degradation of the extracellular matrix of the tumor. Only a small fraction of the necrotic tissues (18.8% of tissues) was found in the tumor treated with PEG-HAuNS plus NIR laser (Figure 24)



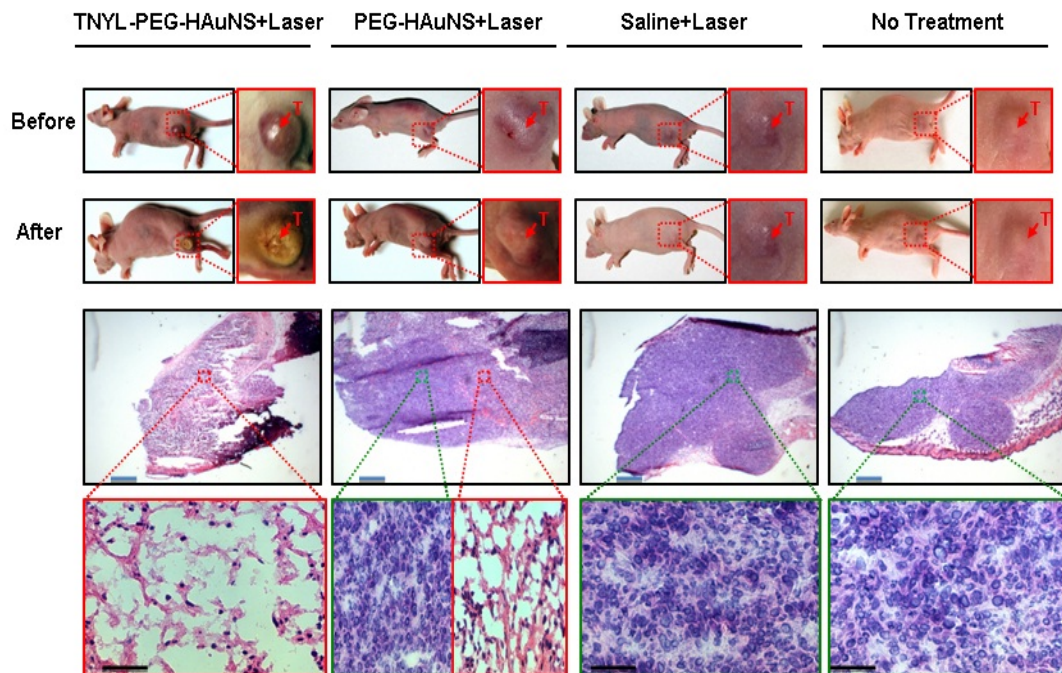


**Figure 23.** AuNS nanoparticles can induce photothermal killing of CT-26 tumors in vivo. (A) Photographs of tumor-bearing mice before and at after NIR laser irradiation ( $3\text{W}/\text{cm}^2$  at 808 nm for 5 min). (B) Representative microphotographs of tumors removed 24 h after NIR laser treatment. The tissues were cryosectioned into  $5\ \mu\text{m}$  slices and stained with hematoxylin/eosin. Scale Bar,  $500\mu\text{m}$  (C) Magnification of necrosis portion of tumor after laser treatment (red color) and normal part of tumor tissue after laser treatment (green color), Scale Bar= $50\mu\text{m}$ .

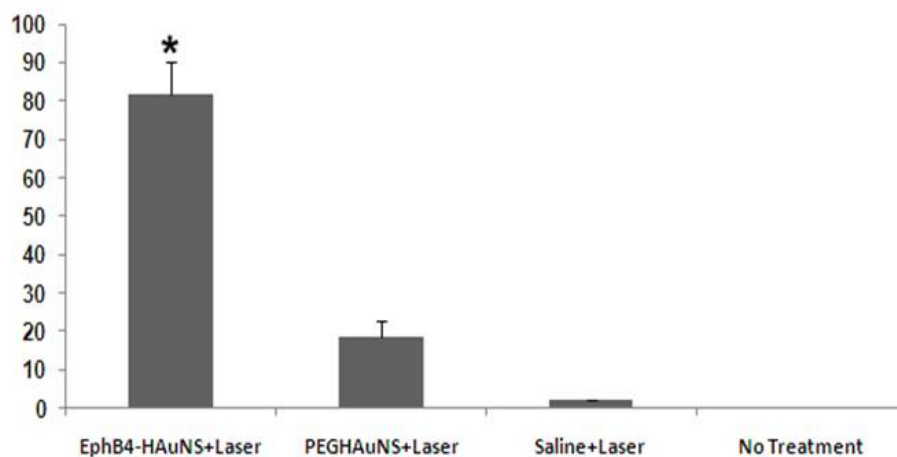


**Figure 24.** The necrotic area as a percentage of the tumor is shown in the bar graph. \*  $P < 0.005$  ( $n = 4$ ).

#### **4. Preliminary study to evaluate EphB4 specific peptide conjugated HAuNS for photothermal ablation therapy of ovarian cancer *in vitro* and *vivo***

##### **4.1 Expression of EphB4 receptors on Hey A8-Luc**

In order to confirm the expression of EphB4 receptor in the Hey A8-Luc ovarian cancer cells, *in vitro* immunofluorescence study was performed. Figure 25 shows that EphB4 is expressed on the Hey A8-Luc cells compared with IgG control group.

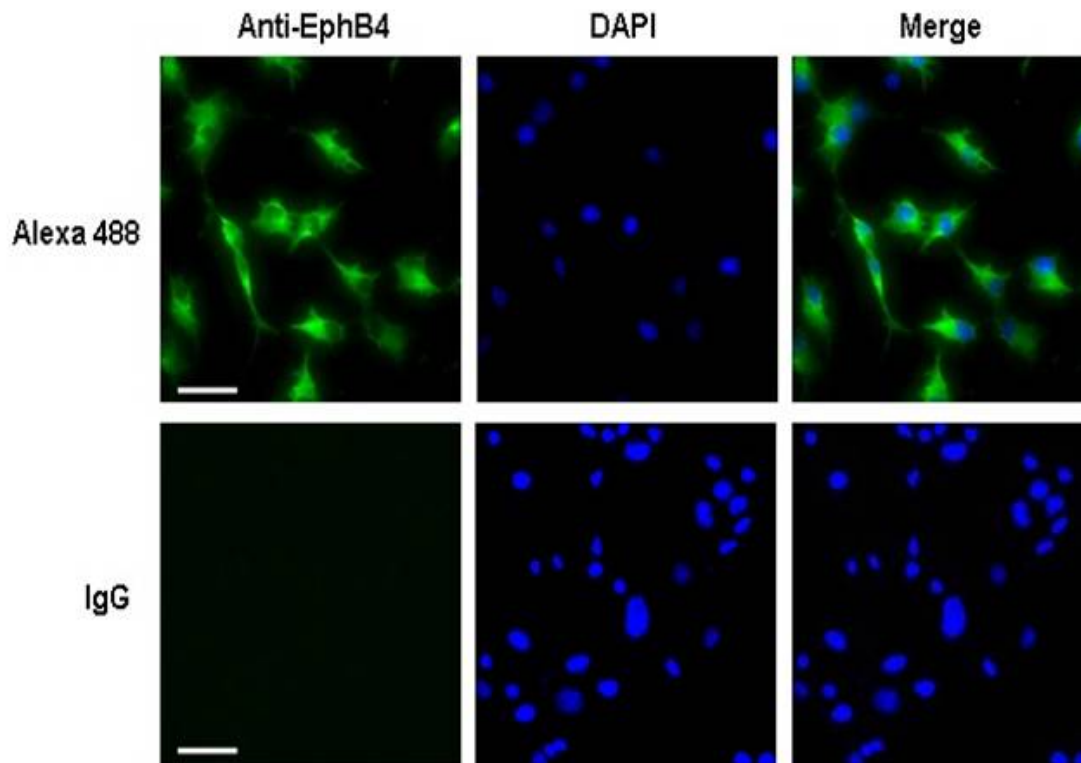


**Figure 25.** Fluorescence photomicrographs of HeyA8-Luc cells stained with rabbit anti-human EphB4 1<sup>st</sup> antibody (1:100 dilution) and goat anti-rabbit 2<sup>nd</sup> antibody conjugated with Alexa Fluor 488 (1:500 dilution). Upper panel shows cells incubated with anti-human EphB4 1<sup>st</sup> antibody and goat anti-rabbit 2<sup>nd</sup> antibody. Lower panel shows the results of IgG control group.

## 4.2 In vitro photothermal ablation of Hey-A8 cancer cells

Figure 26 shows that most of Hey A8-Luc cells treated with TNYL-PEG-HAuNS plus NIR laser irradiation ( $40 \text{ W/cm}^2$  for 5 min) were not stained by calcein AM dye but stained for Eth-D1, which suggested that majority of cells were dead after NIR laser treatment. In contrast, cell viability has no changes after treatment of PEG-HAuNS plus laser, and laser only. The photothermal killing ability of TNYL-PEG-HAuNS was significantly abolished after adding excess amount of TNYL-PEG-SATA.

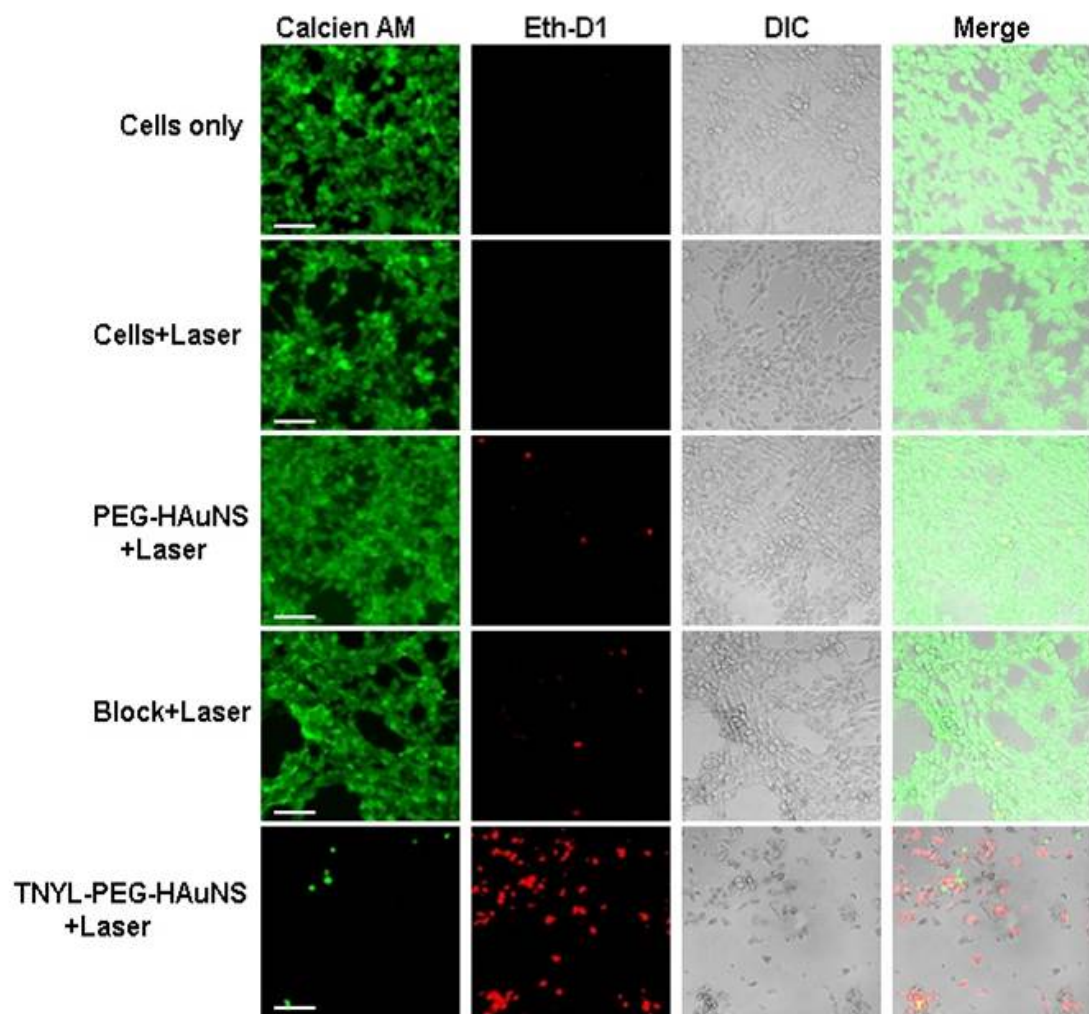


**Figure 26.** Hey A8-Luc cells viability after various treatments. Most of cells were dead after treatment with TNYL-PEG-HAuNS plus NIR laser. Live cells were stained with calcein AM and dead cells were stained for Eth-D1. Scale bar, 100  $\mu$ m.

#### 4.3 Detection of Hey-A8 tumor growth by luciferase imaging

14 days after Hey-A8-Luc tumor cells intraperitoneally implanted in nude mice, Tumor burden as measured by luciferase activity was assessed using Xenogen IVIS-200 Optical in Vivo Imaging System. Figure 27 clearly showed the luciferase activity in the belly area of the nude mice in Hey-A8 tumor models, which confirmed that the tumors were successfully grown in the nude mice.

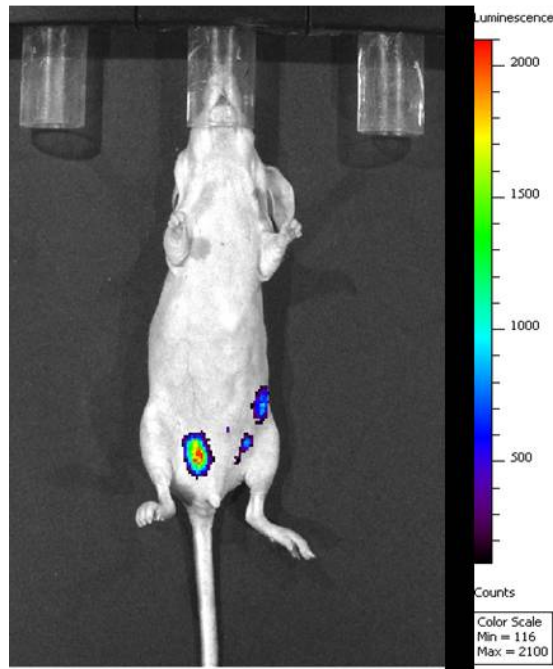


**Figure 27.** Representative Lucifasease images of Hey-A8 tumor on intraperitoneal nude mice model. Figure 10 shows luciferase signal of Hey-A8-Luc 14 days after tail vein injection of luciferin.

#### 4.4 In vivo biodistribution on intraperitoneal Hey-A8 ovarian tumor model

At 24 h after injection, uptake of  $^{64}\text{Cu}$ -TNYL-PEG-HAuNS (4.67% ID/g) in Hey-A8 tumors was higher than  $^{64}\text{Cu}$ -PEG-HAuNS (3.4% ID/g) ( $P < 0.005$ ). The ratio of tumor-to-muscle in the mice injected with  $^{64}\text{Cu}$ -TNYL-PEG-HAuNS was 11.67 compared with the mice injected with  $^{64}\text{Cu}$ -PEG-HAuNS (6.9). The ratio of tumor-to-blood in the mice injected with  $^{64}\text{Cu}$ -TNYL-PEG-HAuNS (1.5) was almost the same as that in the mice injected with  $^{64}\text{Cu}$ -PEG-HAuNS (1.8).

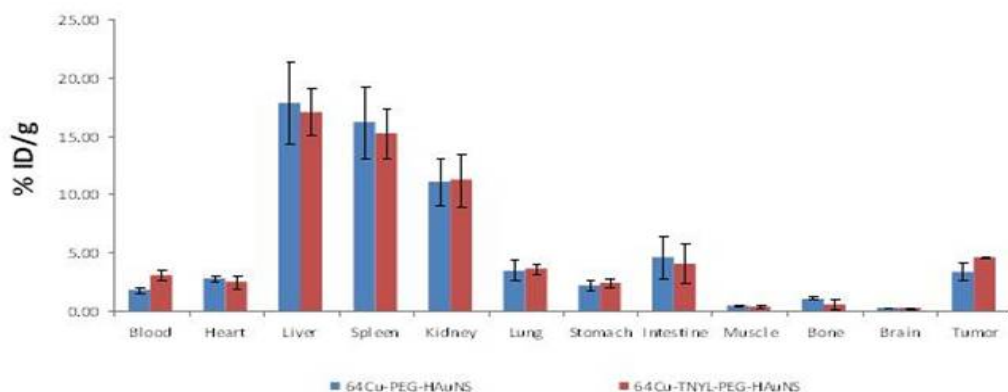


**Figure 28.** *In vivo* biodistribution and tumor uptake of  $^{64}\text{Cu}$  labeled TNYL-PEG-HAuNS or PEG-HAuNS in mice bearing Hey-A8-Luc (intraperitoneal) tumor, 24 h after intravenous injection. The mice bearing Hey-A8-Luc tumor received  $^{64}\text{Cu}$  labeled TNYL-PEG-HAuNS light (red), or  $^{64}\text{Cu}$  labeled PEG-HAuNS (blue).

#### 4.5 In Vivo Photothermal Therapy in Hey-A8 ovarian cancer model

Mice bearing Hey-A8 tumor were treated with PEG-HAuNS ( $2 \times 10^{12}$  per mouse, 200  $\mu\text{L}$ ) or saline (as control 200  $\mu\text{L}$ ). 24 h after injection, the tumors were treated with NIR irradiation. The tumor received intravenous injection of PEG-HAuNS turned brownish,



indicating tissue burns caused by the local photothermal effect. There were no color changes in the tumor treated with saline plus NIR irradiation. The tumor treated with PEG-HAuNS plus the laser, (Figure 29), majority of tissues were necrotized, prominent features of thermonecrosis were found, such as karyolysis, cytoplasmic acidophilia, and corruption and degradation of the extracellular matrix of the tumor. The structure of intestine surrounding tumors that were received photothermal treatment is intact, no significant thermal damage or necrosis was found on tissue slides.

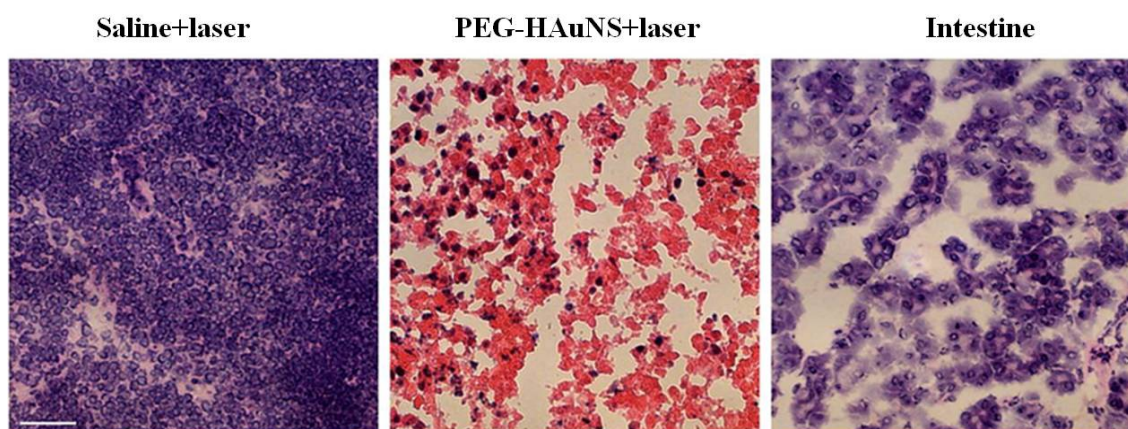


**Figure 29.** AuNS nanoparticles can induce photothermal killing of Hey-A8 tumors in vivo. (B) Representative microphotographs of tumor and intestine removed 24 h after NIR laser treatment. The tissues were cryosectioned into 5  $\mu$ m slices and stained with hematoxylin/eosin. Scale Bar, 50 $\mu$ m

## DISCUSSION

In current study, we successfully developed EphB4 specific TNYL-RAW peptide and found that tail vein injection of the  $^{64}\text{Cu}$  labeled TNYL-RAW peptide allowed ready visualization of EphB4 positive tumor in different nude mice xenograft models by PET/CT. We also synthesized the dual-labeled  $^{64}\text{Cu}$ -TNYL-RAW-Cy5.5 peptides and evaluated the potential application of this peptide for micro PET/CT imaging and near infrared optical imaging in orthotopic glioblastoma (U87 and U251) mice models. Moreover, we synthesized EphB4 specific peptide TNYL-RAW conjugated hollow gold nanoshell for targeted micro PET imaging and photothermal ablation of EphB4-overexpressing cancer cells *in vitro and vivo*.

EphB4 receptor has attracted a lot of interest in cancer imaging recently due to widespread overexpression of EphB4 receptor in lots of different tumors (93). It is possible to develop noninvasive imaging techniques to early diagnosis of patients with high expression of EphB4 receptors in their tumors or monitor the chemotherapy response of the tumors by using EphB4 receptor specific targeting agent. For this purpose, we successfully synthesized and radiolabeled ( $^{64}\text{Cu}$ ) the EphB4 specific peptide TNYL-RAW for PET imaging based on the previous paper published peptide sequence (50).

Based on the SPR analysis, the  $K_D$  value of TNYL-RAW peptide was 3.09 nM, which is similar to the previous literature published ( $K_D$ , 1–2 nM) (50). The slow dissociation rate of the TNYL-RAW peptide ( $\sim 1.3 \times 10^{-3} \text{ s}^{-1}$ ) strongly indicated that this peptide is suitable for *in vivo* molecular imaging applications due to its simple binding affinity. It has been reported that the stability of binding complex with EphB4 was not significantly



affected by modifying the N terminus of the peptide (94). However, based on our SPR analysis, it is interesting to find out that there was an 8-fold reduction in  $K_D$  value of the TNYL-RAW when the N terminus of TNYL-RAW was modified by introducing the radiometal chelator DOTA. But the coupling of  $Cu^{2+}$  to the DOTA-TNYL-RAW peptide can restore the binding affinity of TNYLRAW to 1.89 nM (Table 1). Therefore, the subtle modification of N terminus of TNYL-RAW peptide can still affect the binding affinity of the TNYL-RAW to EphB4 receptors. Because there was no significant interaction between the scramble peptide and EphB4 receptors, we concluded that this TNYL-RAW binding to EphB4 *in vitro* is sequence specific. In the literature, there has been reported that EphB4 receptors are overexpressed in most of colon cancer and prostate cancer cell lines (38, 95, 96). The CT26 (mouse colon cancer cell lines) and PC-3M (human prostate cancer cell lines) cells used in our study has been confirmed positive for EphB4 expression (Figure 3) by immunofluorescence study. FITC labeled TNYL-RAW peptide exhibits high affinity and specific binding to EphB4 receptor *in vitro* binding study. The similar binding pattern to EphB4 positive cancer cells was also found in the results of  $^{64}Cu$ -DOTA-TNYL-RAW uptake study (Fig. 3 and 4). The specific binding of peptide to EphB4 receptor was confirmed by *in vitro* blocking study. All above results indicated that  $^{64}Cu$ -DOTA-TNYL-RAW peptide is a suitable probe for noninvasive imaging of EphB4 receptors.

The uptake of  $^{64}Cu$ -DOTA-TNYL-RAW was significantly high in EphB4 positive PC-3M and CT-26 tumor xenografts in nude mice by *in vivo* micro PET/CT studies. In contrast, the radiotracer showed very low uptake in EphB4 negative A549 tumors at all time points examined (Fig. 5). To further confirm the expression status of EphB4 in

different tumors, ex vivo immunohistostaining of tumor xenografts sections was performed. The results showed that high expression level of EphB4 receptors was observed in both CT26 and PC-3M tumors but not in A549 tumors. From the micro PET/CT images, the radioactivity signal of  $^{64}\text{Cu}$ -DOTA-TNYL-RAW in CT26 tumors was significantly reduced after 4h post i.v. injection of radiotracer. In contrast, the signal of radioactivity reached highest in PC-3M tumors at 24 h post injection (Fig. 24). Because the relatively slow dissociation rate of peptide-EphB4 receptor complex, the major determinant of the difference in the signal intensity at various time points between those two tumors are the expression levels of EphB4 receptors on these two tumors. However, this different radiotracer retention time in tumor tissues between CT26 and PC-3M tumor mice models could also be explained by the difference in the degradation of  $^{64}\text{Cu}$ -DOTA-TNYL-RAW peptide-based radiotracer in different tumor microenvironments. It is very critical for maintaining the molecular integrity of the radioactive peptides *in vivo* condition in order to circulation in blood for the purpose of biodistribution and imaging studies. We tested the stability of  $^{64}\text{Cu}$ -DOTATNYL- RAW DMEM with 10% FBS and in mouse serum. We found out that it was stable in DMEM with 10% FBS for at least 24 h and in mouse serum for up to 2 h (Chiyi Xiong, *et al.* unpublished data). The slow degradation of peptide was observed in mouse serum after 2 h incubation. The above slow metabolic degradation of the radiolabeled peptide could be explained by the proteolysis of linear peptides by plasma peptidases present in mouse serum (97). In order to improve the stability of the peptide, we can introduce D-amino acid into the peptide sequence or cyclization of the peptide to make it more resistant to enzymatic degradation (98, 99). The studies of improving *in vivo* stability of TNYL-

RAW are in progress. Based on our stability data and *in vivo* PET/CT imaging results, the stability of our peptides is sufficient for *in vivo* applications of tumor imaging and biodistribution study.

In order to confirm the specificity uptake of  $^{64}\text{Cu}$ -DOTA-TNYL-RAW in EphB4 positive tumors *in vivo*, blocking studies were performed by co-administration of the radiolabeled peptides with excess amount of nonradioactive (cold) TNYL-RAW peptide. There were significant reductions in the uptake of  $^{64}\text{Cu}$ -DOTA-TNYL-RAW in both CT26 and PC-3M tumors with co-injection of radiotracer with excess amount of cold TNYL-RAW (Figure 5B) from micro PET/CT image results. Quantitative analysis of and comparison of radioactive uptake of  $^{64}\text{Cu}$ -DOTA-TNYL-RAW in different tumor tissues based on the ROI manually drawn from the micro PET/CT images showed that 77% and 81% reduction in  $^{64}\text{Cu}$ -DOTA-TNYL-RAW uptake in CT-26 and PC-3M tumors at 4h or 24h respectively (Fig. 5B). The low uptake of  $^{64}\text{Cu}$ -DOTA-TNYL-RAW (Figure. 5A) in EphB4 negative expression A549 tumors together with all above results supported conclusion that the specific uptake of  $^{64}\text{Cu}$ -DOTA-TNYL-RAW in EphB4 positive colon and prostate cancer xenografts in nude mice models was mediated by EphB4 receptors. The biodistributions of  $^{64}\text{Cu}$ -DOTA-TNYL-RAW in different tumor models obtained by both noninvasive PET/CT calculated from ROI and by *in vivo* tissue sampling indicated that the major organs for uptake and clearance of this radiopharmaceutical were in liver and the kidney. It was well known that the major organ for clearance of hydrophobic peptides is in liver (100). The high level of uptake of  $^{64}\text{Cu}$ -DOTA-TNYL-RAW in liver could be attributed to compositions of the hydrophobic amino acids (Asn, Ile, Leu, Phe, Pro, Ala, Trp) in TNYL-RAW peptides.

Also the significant uptake of the radiotracers in the nude mice kidneys was due to the degradation of the peptide by lysosome within renal cells (101). Therefore, it is important for us to optimize pharmacokinetics and *in vivo* stability of peptides for *in vivo* imaging applications.

Glioblastoma is the most malignant primary brain tumor that is resistant to most of common drug therapies. The frequent recurrence of this tumor is due to its infiltration into surrounding normal brain tissue and difficulty in complete resection of the tumors (102, 103). It is important to develop diagnostic imaging agent to monitor tumor growth in the brain and evaluate tumor responses to therapeutic drugs. Recently, lots of optical imaging using near infrared fluorescent dye labeled tumor-specific molecules has been successfully applied to imaging glioma in preclinical animal models based on the overexpression of specific marker on glioma (104-106). The characteristics of near infrared fluorescence (NIR) such as long wavelength (650–900 nm), lower light absorbance and scattering, and reduced autofluorescence of normal tissues make it great potential in clinical imaging application (107). Several recent studies have demonstrated that using fluorescence imaging to improve radical resection of GBM during surgery (108-110). Meanwhile, nuclear imaging has high detection sensitivity ability, which makes it especially suitable for tracking radiotracers used in *in vivo* molecular imaging. So, it is highly desirable to develop an imaging probe combining a radioisotope and a near-infrared fluorescent dye for dual nuclear and optical imaging of glioma. Overexpression of EphB4 receptors has been reported in a number of tumors. Up to now, there are few papers describing the applications of EphB4 as target for cancer imaging (35, 36). In high-grade glioma, EphB4 are expressed at high levels in both tumor cells

and blood vessels<sup>16</sup>. In current study, we developed dual-labeled EphB4 specific TNYL-RAW peptides for visualization of glioblastomas with micro PET/CT and near-infrared fluorescence imaging on orthotopic mice model.

SPR analysis showed that the  $K_D$  values of Cy5.5-TNYL-RAW and Cy5.5-TNYL-RAW-DOta are around 1nM which have no significant changes compared with the value of original TNYL-RAW peptide (3.07 nM). The high binding affinity of the dual labeled EphB4 specific peptide to EphB4 receptor *in vitro* makes it suitable for *in vivo* molecular imaging application. For monitor intracranial tumor growth in nude mice, we made the stable cell lines that express the luciferase gene. Ten days post injection of tumors in the mice brains, the detectable luciferase signal has been visualized on Xenogen imaging system which corresponded to the tumor growth in the mice brain. Near infrared fluorescence imaging studies revealed that Cy5.5-TNYL-RAW-DOTA has significant higher uptake in U251 and u87 tumors in orthotopic nude mice model. To confirm the specificity of uptake of EphB4 targeted peptide in tumors, Cy5.5 labeled scramble peptides have been used. From various time points of optical imaging, it clearly showed that there was low uptake of scramble peptides uptake in U87 tumors compared with that of Cy5.5-TNYL-RAW-DOTA peptides, which indicated that this high uptake of EphB4 peptides into tumors was mediated through EphB4 receptor (Figure 11B). The biodistribution data showed the same result as fluorescence optical imaging based on *ex vivo* analysis of the fluorescence signal intensities of dissected tissues. High fluorescence activity was found in mice liver, kidney, stomach and intestine. Compared with fluorescence densities in two groups at different time points, it clearly showed that U87 tumor has significantly higher uptake of Cy5.5-TNYL-RAW-

DOTA than that of Cy5.5-scramble-DOTA (Figures 12A and 12B). It is interesting to notice that the accumulation of Cy5.5-TNYL-RAW-DOTA was lower in liver than that in kidney, but the uptake of  $^{64}\text{Cu}$ -TNYL-RAW was similar in both kidney and liver in previous results. This phenomenon maybe due to the underestimation of the fluorescence signal obtained from liver. Previous paper published in our lab (111) demonstrated that *ex vivo* analysis fluorescence intensity may have underestimated the uptake of nanoparticles or compounds in organs with high blood perfusion. Because estimation of uptake of compounds in tissues based on fluorescence intensity is less accurate the radioactivity count method, our above data suggested that the biodistribution data should be corrected in different organs when fluorescence method is used.

Micro PET/CT images revealed significant high uptake of  $^{64}\text{Cu}$  labeled Cy5.5-TNYL-RAW-DOTA peptides in U251 and in U87 tumor models. The intensity of radioisotope labeled peptides was greatly reduced in U251 tumors after co-injection of excess amount of cold peptide with the  $^{64}\text{Cu}$  labeled Cy5.5-TNYL-RAW-DOTA peptides (Figures 13A and 13B). Quantitative analysis of micro PET/CT imaging revealed that In U251 tumor models, the co-administration of cold Cy5.5-TNYL-RAW-DOTA caused a 57% reduction in the ratio of  $^{64}\text{Cu}$ -Cy5.5-TNYLRAW-DOTA accumulation in tumors versus normal brain, which demonstrated the specific uptake of dual labeled TNYL-RAW-DOTA peptide in U251 tumor. Immunofluorescence microscope study showed an interesting phenomenon. For U251 tumor model, Cy5.5 labeled peptides mainly bind to tumor cells and tumor associated vessels which both express EphB4 receptor on their surface. In contrast, the Cy5.5 labeled peptides only bind to tumor associated vessel that express EphB4 but not on tumor cells that is

negative staining for the expression of EphB4 (Figure 14). It has been reported that EphB4 are overexpressed on brain tumor cells and tumor associated vessels. This is the first time we show here that the new developed dual-labeled EphB4-specific peptide could be used as a non-invasive molecular imaging agent for PET/CT and optical imaging of glioma owing to its ability to bind to EphB4-expressing angiogenic blood vessels and/ or to EphB4-expressing tumor.

HAuNS have already shown the great potential in photothermal therapy of cancer due to their unique characteristics such as small size (30-60 nm), spherical shape, and hollow interior and strong tunable (520-950nm) absorption band (74). The further application of the HANs to cancer therapy is to develop targeted delivery of nanoparticles into tumors to minimize the thermal damage to surrounding normal tissues. With this aim, we developed TNYL-conjugated HANs for selective photothermal killing of EphB4 positive cancer cells. In current study, we successfully conjugate EphB4 specific (TNTL-PEG) peptide and/or PEG-SH onto the surface of HANs without significant changes of the properties of HANs. From resonance absorbance curves, the absorption peak of the TNYL-PEG-HANs or PEG-HANs is still around 800nm compared with original HANs, which demonstrates that conjugation of peptides onto the surface of HANs has no obvious effect on the plasma resonance property. The temperature of nanoparticle solutions was increased from 27 °C to 75 °C at the concentration of  $4 \times 10^{11}$  particles/mL after exposure to near infrared-region laser light. The photothermal effect of these particles remains no changes after conjugation of peptides. The amount of peptides on the surface of HANs will also affect the specific binding affinity of HANs to EphB4 positive tumors. From our amino acid analysis of

conjugated HAuNS, the number of peptides on the surface of HAuNS is around 40, which will greatly increase the binding repertoire of original TNYL-PEG peptide. As shown in Figures 16, TNYL-PEG-HAuNS but not PEG-HAuNS binds to EphB4 positive PC-3M and CT-26 cells. Moreover, the uptake of TNYL-PEG-HAuNS to CT-26 or PC-3M cells could specifically be blocked by excess amount of free TNYL-PEG peptides, indicating that TNYL-PEG-HAuNS was taken up by the PC-3M or CT-26 cells through EphB4 receptor-mediated. After exposure CT-26, PC3-M or Hey-A8 cells treated with TNYL-PEG-HAuNS or PEG-HAuNS to NIR laser at  $40\text{W}/\text{cm}^2$  for 5 min, almost majority of cancer cells treated with TNYL-PEG-HAuNS were destroyed after exposure to laser, but this effect was not observed in cells exposed NIR laser alone or PEG-HAuNS plus laser group. This photothermal killing effect was efficiently abolished by the addition of excess amount of PEG-TNYL peptide into the reaction.

For *in vivo* active targeting nanoparticles to the tumor tissue, HAuNS must be capable of extravasating into the tumor interstitial space. Our HAuNS with small size makes it suitable for *in vivo* delivery to tumor site. The photothermal effect of HAuNS *in vivo* depends on the number of particle actively taken up by the tumor. To quantify the amount of nanoparticles specific delivery to EphB4 positive CT-26 tumors *in vivo* after systematic administration of  $^{64}\text{Cu}$ -TNYL-PEG-HAuNS or  $^{64}\text{Cu}$ -PEG-HAuNS, micro-PET and *in vivo* biodistribution experiments were performed. From Figure 21, it clearly showed that the tumor was visualized at 1 hour after the injection and the signal was strongest at 24 h post injection. But low signal in the tumors of mice injected with  $^{64}\text{Cu}$ -PEG-HAuNS was also observed, which suggested that non-specific uptake of HAuNS in the tumor tissue. This nonspecific uptake phenomenon can be explained by the EPR



(enhanced permeability and retention) effect. The EPR effect is the property by which that certain size of the molecules such as liposomes, nanoparticles and some macromolecules can accumulate into the tumor tissue much more than they do in normal tissues due to the pathophysiological changes of tumor vessels (extensive angiogenesis defective vascular architecture, and greatly increased production of permeability mediators) (112-115). The biodistribution study also showed the similar results to the micro-PET imaging study. At 24 h after injection of radiolabeled nanoparticles, uptake of  $^{64}\text{Cu}$ -TNYL-PEG-HAuNS was significantly higher (4.92% ID/g) in CT-26 tumors than that of  $^{64}\text{Cu}$ -PEG-HAuNS was. (1.49% ID/g) ( $p < 0.001$ ). The tumor-to-muscle ratio was 6.2 in the mice injected of  $^{64}\text{Cu}$ -PEG-HAuNS, while it was 25.9 in the mice treated with  $^{64}\text{Cu}$ -TNYL-PEG-HAuNS. Also the The ratio of tumor-to-blood in the mice injected with  $^{64}\text{Cu}$ -TNYL-PEG-HAuNS (2.94) was 1.5 times higher than that in the mice injected with  $^{64}\text{Cu}$ -PEG-HAuNS (2.0) ( $p < 0.005$ ). Taken together, all above data demonstrate that TNYL-PEG-HAuNS can be specifically uptake into EphB4 positive CT-26 tumors compared with control PEG-HAuNS. (Figure 22). *In vivo* photothermal therapy study confirmed that tumor with intravenous injection of TNYL-PEG-HAuNS plus laser treatment caused significantly greater thermonecrotic response than that of mice treated with PEG-HAuNS plus laser treatment, saline plus laser treatment, or saline only (Figs. 23B and 23C). In the mice treated with TNYL-PEG-HAuNS plus the laser, (Figures 23B and C), majority of tissues (82% of tissues) were necrotized, prominent features of thermonecrosis were found, such as karyolysis, cytoplasmic acidophilia, and corruption and degradation of the extracellular matrix of the tumor. Only a small fraction of the necrotic tissues (18.8% of tissues) was found in the tumor treated with PEG-

HAuNS plus NIR laser (Figure 24). From histological results, we still can observe some necrosis response in PEG-HAuNS plus laser treatment group, which also can be explained by EPR effect which corresponding to the result of micro-PET and biodistribution data. Our current study clearly shows the selective killing tumor cells after intravenously injection of TNYL-PEG-HAuNS plus near infrared-region laser light treatment. But the tumor model we choose here is subcutaneous tumor model which may not reflect the real situation due to the local blood flow difference between subcutaneous of the mouse skins and orthotopic sites.

Therefore, further studies will focus on the application of TNYL-PEG-HAuNS in orthotopic tumor models for further investigation of their photothermal killing effect *in vivo*. But the study of biodistribution of  $^{64}\text{Cu}$ -TNYL-PEG-HAuNS or  $^{64}\text{Cu}$ -PEG-HAuNS on Hey-A8-Luc ovarian cancer intraperitoneal nude mice models showed that the uptake of  $^{64}\text{Cu}$ -TNYL-PEG-HAuNS was statistically higher (4.67% ID/g) in Hey-A8 tumors than that of  $^{64}\text{Cu}$ -PEG-HAuNS was (3.4% ID/g) ( $P < 0.005$ ). But the ratio of tumor-to-blood in the mice injected with  $^{64}\text{Cu}$ -TNYL-PEG-HAuNS (1.5) was almost the same as that in the mice injected with  $^{64}\text{Cu}$ -PEG-HAuNS (1.8), which suggested that the different uptake of  $^{64}\text{Cu}$ -TNYL-PEG-HAuNS and  $^{64}\text{Cu}$ -PEG-HAuNS in the Hey-A8 tumors may be due to the EPR effect. Although we didn't get promising data from orthotopic ovarian cancer models, it still provided us useful information. In clinical situation, it is very difficult to treat metastatic spread of ovarian cancer in pelvic of patients. Because we didn't find good targeting effect of TNYL-PEG-HAuNS on Hey-A8 nude mice model, we want to study the photothermal killing effect of PEG-HAuNS on tumors after intravenously injection of the nanoparticles due to the high uptake of

the  $^{64}\text{Cu}$ -PEG-HAuNS (3.4%) in tumor. After treating the tumor with laser at  $2\text{W}/\text{cm}^2$ , the color of the tumor of the mice injected with PEG-HAuNS turned into brown color, but there is no color change of the tumor with saline injected or with no treatment. H&E staining results showed that majority of tissues were necrotized, prominent features of thermonecrosis were found, such as karyolysis, cytoplasmic acidophilia, and corruption and degradation of the extracellular matrix of the tumor. For saline control or no treatment group, there was no thermonecrosis area in the tumor section. To check whether the laser treatment will damage the local normal tissue surrounding the tumor, the intestine tissues around the tumor were also taken out and cut into sections. We can see that the structure of intestine was still intact and there is no photothermal damage to the normal intestine tissues so far. It is still preliminary data for investigation of photothermal effect on Hey-A8 intraperitoneal ovarian cancer model. In the future, we need test this killing effect on more mice to collect data to figure out whether this local photothermal effect will kill tumor cells but cause no or minimum damage to the tissue surrounding it. Because we only tested our nanoparticles on one ovarian orthotopic model, we still need check other orthotopic ovarian cancer models such as transgenic mice models to further investigate the targeting effect of TNYL-PEG-HAuNS *in vivo*.

Though TNYL-RAW showed a great potential in the application of imaging tumor in mice and cancer thermal therapy when conjugated with HAuNS, there is a still long way to go before we apply it in clinical use. First, the slowly degradation of TNYL-RAW in mouse serum indicates that the detection sensitivity will decrease after long time circulation in the body. It is important to improve the stability of this peptide for its clinical application. Introduction of D-amino acid or cyclization of peptide can make it

more resistant to proteolytic degradation of peptide. Now we have already synthesized the second generation of the peptides to optimize the stability of the peptide. Our SPR analysis confirmed that introduction of D-amino acid into peptide sequence or cyclization of the peptide did not significantly change the binding affinity of the peptide to EphB4 receptor. In the future, we will evaluate its application in tumor imaging *in vivo* by micro PET/CT or optical imaging. Secondly, it is obvious that the major organ for the clearance of the peptide is liver. So it is highly desirable to modify the structure of the peptide to reduce the liver clearance. Literature has been reported that pegylation of the peptide can significantly reduce the liver nonspecific uptake of the peptide (116, 117). Synthesis and evaluation of the PEG conjugated TNYL-RAW *in vivo* PET/CT imaging of tumor on nude mice is ongoing right now. Third, the tumor model we used in this study for evaluate the peptide is subcutaneously model and brain orthotopic models, which is not the most ideal models for evaluation of peptide *in vivo* applications due to difference in the local blood flow and microenvironment for tumor growth. There are lots of transgenic mice tumor models available for prostate, colon and glioma cancers. We will evaluate our peptide in these transgenic mice models for *in vivo* molecular imaging applications. Conjugation of TNYL-RAW peptide onto the surface of the HANs makes it suitable for targeting photothermal therapy. In this study we only use microscopic study to evaluate necrotic response of photothermal therapy, which is not very accurate. So it is highly desirable use other methods to evaluate tumor necrosis induced by photothermal therapy. Our lab has developed  $^{64}\text{Cu}$ -DOTA-hypericin for evaluation of the tumor necrosis induced by photothermal therapy by PET/CT (118). Also  $^{18}\text{F}$ -FDG can also be used to monitor the changes of metabolic activity of the tumors by micro

PET/CT (85). We can use above methods to monitor tumor response to the photothermal therapy for EphB4 conjugated HAuNS. To monitor the tumor response to the photothermal therapy, we can also monitor the tumor growth in long term after treatment to see whether tumor growth can be inhibited by photothermal therapy. Because in clinical settings, it is very difficult to remove all of the metastatic nodules in the pelvic of ovarian cancer patients by surgery, it is very desirable to find alternative way to treat this advanced stage disease to avoid using aggressive surgery treatment. Using photothermal ablation therapy, the tumor can shrink and necrotized. So it is important for us to study the photothermal effect of HAuNS on more ovarian cancer nude mice models in future.

## CONCLUSIONS

In the current study, it is the first time to visualize tumor by *in vivo* noninvasive micro PET/CT using EphB4 specific radiotracer  $^{64}\text{Cu}$ -DOTA-TNYL-RAW. This radiolabeled peptide could be used for early diagnosis of patients with high expression of EphB4 receptors in their tumors or monitoring the chemotherapy response of the tumors. To demonstrate the future potential of this radiotracer, it is important for us to evaluate it in additional animal models and *ex vivo* human specimens. We also evaluated the potential applications of  $^{64}\text{Cu}$  and Cy5.5 dual labeled TNYL-RAW-DOTA peptides for micro PET/CT imaging and near infrared optical imaging in orthotopic glioblastoma mice model.  $\mu\text{PET/CT}$  and near-infrared optical imaging clearly showed the uptake of the dual labeled TNYL-RAW peptide in both U251 and U87 tumors in the brains of nude mice after intravenous injection. The specific uptake of dual labeled peptide in both tumors was confirmed by blocking experiments. In U87 tumors, Cy5.5-labeled peptide was found co-localized only with CD31- and EphB4-expressing tumor blood vessels. Dual-labeled EphB4-specific peptide could be used as a non-invasive molecular imaging agent for PET/CT and optical imaging of glioma owing to its ability to bind to EphB4-expressing angiogenic blood vessels and to EphB4-expressing tumor. We developed the EphB4 specific peptide conjugated HAU NS for micro PET imaging and photothermal ablation of EphB4-overexpressing cancer cells *in vitro and vivo*. TNYL-PEG-HAU NS targeted to EphB4 receptor have been shown to selectively bind to EphB4-positive cancer cells (PC-3M and CT-26) and destroy these cells via a photothermal effect *in vitro*. EphB4-positive CT-26 tumors were clearly visualized with  $^{64}\text{Cu}$ -labeled TNYL-PEG-HAU NS. *In vivo* biodistribution study, up to 4.9.%ID/g of  $^{64}\text{Cu}$ -labeled TNYL-

PEG-HAuNS was taken up by CT-26 tumor compared to TNYL-HAuNS. EphB4 targeted TNYL-PEG-HAuNS shows more photothermal killing effect on CT26 tumor models than PEG-HAuNS do, which suggests that TNYL-PEG-HAuNS targeting to EphB4 receptor may have future applications in photothermal ablation therapy in clinical.

## REFERENCES

1. Hirai, H., Y. Maru, K. Hagiwara, J. Nishida, and F. Takaku. 1987. A novel putative tyrosine kinase receptor encoded by the eph gene. *Science* 238:1717-1720.
2. Maru, Y., H. Hirai, and F. Takaku. 1990. Overexpression confers an oncogenic potential upon the eph gene. *Oncogene* 5:445-447.
3. Bartley, T. D., R. W. Hunt, A. A. Welcher, W. J. Boyle, V. P. Parker, R. A. Lindberg, H. S. Lu, A. M. Colombero, R. L. Elliott, B. A. Guthrie. 1994. B61 is a ligand for the ECK receptor protein-tyrosine kinase. *Nature* 368:558-560.
4. Pasquale, E. B. 2005. EPH receptor signalling casts a wide net on cell behaviour. *Nat Rev Mol Cell Bio* 6:462-475.
5. Gu, C., and S. Park. 2001. The EphA8 receptor regulates integrin activity through p110gamma phosphatidylinositol-3 kinase in a tyrosine kinase activity-independent manner. *Mol Cell Biol* 21:4579-4597.
6. Matsuoka, H., H. Obama, M. L. Kelly, T. Matsui, and M. Nakamoto. 2005. Biphasic functions of the kinase-defective Ephb6 receptor in cell adhesion and migration. *J Biol Chem* 280:29355-29363.
7. Miao, H., K. Strebhardt, E. B. Pasquale, T. L. Shen, J. L. Guan, and B. Wang. 2005. Inhibition of integrin-mediated cell adhesion but not directional cell migration requires catalytic activity of EphB3 receptor tyrosine kinase. Role of Rho family small GTPases. *J Biol Chem* 280:923-932.



8. Stein, E., A. A. Lane, D. P. Cerretti, H. O. Schoecklmann, A. D. Schroff, R. L. Van Etten, and T. O. Daniel. 1998. Eph receptors discriminate specific ligand oligomers to determine alternative signaling complexes, attachment, and assembly responses. *Genes Dev* 12:667-678.
9. Davis, S., N. W. Gale, T. H. Aldrich, P. C. Maisonpierre, V. Lhotak, T. Pawson, M. Goldfarb, and G. D. Yancopoulos. 1994. Ligands for EPH-related receptor tyrosine kinases that require membrane attachment or clustering for activity. *Science* 266:816-819.
10. Kullander, K., and R. Klein. 2002. Mechanisms and functions of Eph and ephrin signalling. *Nat Rev Mol Cell Biol* 3:475-486.
11. Ip, N. Y., K. O. Lai, Y. Chen, H. M. Po, K. C. Lok, and K. Gong. 2004. Identification of the Jak/Stat proteins as novel downstream targets of EphA4 signaling in muscle - Implications in the regulation of acetylcholinesterase expression. *Journal of Biological Chemistry* 279:13383-13392.
12. Carpenter, C. L., and L. C. Cantley. 1996. Phosphoinositide 3-kinase and the regulation of cell growth. *Bba-Rev Cancer* 1288:M11-M16.
13. Flanagan, J. G., and P. Vanderhaeghen. 1998. The ephrins and Eph receptors in neural development. *Annu Rev Neurosci* 21:309-345.
14. Pasquale, E. B., and K. K. Murai. 2003. 'Eph'ective signaling: forward, reverse and crosstalk. *J Cell Sci* 116:2823-2832.
15. Pasquale, E. B. 2008. Eph-ephrin bidirectional signaling in physiology and disease. *Cell* 133:38-52.

16. Anderson, D. J., H. U. Wang, and Z. F. Chen. 1998. Molecular distinction and angiogenic interaction between embryonic arteries and veins revealed by ephrin-B2 and its receptor Eph-B4. *Cell* 93:741-753.
17. Arango, D., J. Castano, V. Davalos, and S. Schwartz. 2008. EPH receptors in cancer. *Histol Histopathol* 23:1011-1023.
18. Ireton, R. C., and J. Chen. 2005. EphA2 receptor tyrosine kinase as a promising target for cancer therapeutics. *Curr Cancer Drug Targets* 5:149-157.
19. Landen, C. N., M. S. Kinch, and A. K. Sood. 2005. EphA2 as a target for ovarian cancer therapy. *Expert Opin Ther Targets* 9:1179-1187.
20. Wykosky, J., and W. Debinski. 2008. The EphA2 receptor and ephrinA1 ligand in solid tumors: function and therapeutic targeting. *Mol Cancer Res* 6:1795-1806.
21. Zhuang, G., D. M. Brantley-Sieders, D. Vaught, J. Yu, L. Xie, S. Wells, D. Jackson, R. Muraoka-Cook, C. Arteaga, and J. Chen. 2010. Elevation of receptor tyrosine kinase EphA2 mediates resistance to trastuzumab therapy. *Cancer Res* 70:299-308.
22. Huang, F., K. Reeves, X. Han, C. Fairchild, S. Platero, T. W. Wong, F. Lee, P. Shaw, and E. Clark. 2007. Identification of candidate molecular markers predicting sensitivity in solid tumors to dasatinib: rationale for patient selection. *Cancer Res* 67:2226-2238.
23. Wang, X. D., K. Reeves, F. R. Luo, L. A. Xu, F. Lee, E. Clark, and F. Huang. 2007. Identification of candidate predictive and surrogate molecular markers for dasatinib in prostate cancer: rationale for patient selection and efficacy monitoring. *Genome Biol* 8:R255.

24. Kandpal, R. P., and B. P. Fox. 2004. Invasiveness of breast carcinoma cells and transcript profile: Eph receptors and ephrin ligands as molecular markers of potential diagnostic and prognostic application. *Biochem Bioph Res Co* 318:882-892.
25. Lawrenson, I. D., S. H. Wimmer-Kleikamp, P. Lock, S. M. Schoenwaelder, M. Down, A. W. Boyd, P. F. Alewood, and M. Lackmann. 2002. Ephrin-A5 induces rounding, blebbing and de-adhesion of EphA3-expressing 293T and melanoma cells by CrkII and Rho-mediated signalling. *J Cell Sci* 115:1059-1072.
26. Easty, D. J., S. P. Hill, M. Y. Hsu, M. E. Fallowfield, V. A. Florenes, M. Herlyn, and D. C. Bennett. 1999. Up-regulation of ephrin-A1 during melanoma progression. *Int J Cancer* 84:494-501.
27. Kinch, M. S., J. Walker-Daniels, K. Coffman, M. Azimi, J. S. Rhim, D. G. Bostwick, P. Snyder, B. J. Kerns, and D. J. Waters. 1999. Overexpression of the EphA2 tyrosine kinase in prostate cancer. *Prostate* 41:275-280.
28. Boyd, A. W., and M. Lackmann. 2001. Signals from Eph and ephrin proteins: a developmental tool kit. *Sci STKE* 2001:re20.
29. Holder, N., L. Durbin, C. Brennan, K. Shiomi, J. Cooke, A. Barrios, S. Shanmugalingam, B. Guthrie, and R. Lindberg. 1998. Eph signaling is required for segmentation and differentiation of the somites. *Gene Dev* 12:3096-3109.
30. Cheng, H. J., M. Nakamoto, A. D. Bergemann, and J. G. Flanagan. 1995. Complementary Gradients in Expression and Binding of Elf-1 and Mek4 in Development of the Topographic Retinotectal Projection Map. *Cell* 82:371-381.

31. Chen, J., N. Cheng, and D. M. Brantley. 2002. The ephrins and Eph receptors in angiogenesis. *Cytokine Growth F R* 13:75-85.
32. Kumar, S. R., J. S. Seehnet, E. J. Ley, J. Singh, V. Krasnoperov, R. Liu, P. K. Manchanda, R. D. Ladner, D. Hawes, F. A. Weaver, R. W. Beart, G. Singh, C. Nguyen, M. Kahn, and P. S. Gill. 2009. Preferential induction of EphB4 over EphB2 and its implication in colorectal cancer progression (vol 69, pg 3736, 2009). *Cancer Research* 69:4554-4554.
33. Gill, P. S., S. R. Kumar, J. Singh, G. B. Xia, V. Krasnoperov, L. Hassanieh, E. J. Ley, J. Seehnet, N. G. Kumar, D. Hawes, M. F. Press, and F. A. Weaver. 2006. Receptor tyrosine kinase EphB4 is a survival factor in breast cancer. *Am J Pathol* 169:279-293.
34. Bergemann, A. D., and M. Nakamoto. 2002. Diverse roles for the Eph family of receptor tyrosine kinases in carcinogenesis. *Microsc Res Techniq* 59:58-67.
35. Xiong, C., M. Huang, R. Zhang, S. Song, W. Lu, L. Flores, 2nd, J. Gelovani, and C. Li. 2011. In vivo small-animal PET/CT of EphB4 receptors using <sup>64</sup>Cu-labeled peptide. *J Nucl Med* 52:241-248.
36. Zhang, R., C. Xiong, M. Huang, M. Zhou, Q. Huang, X. Wen, D. Liang, and C. Li. 2011. Peptide-conjugated polymeric micellar nanoparticles for Dual SPECT and optical imaging of EphB4 receptors in prostate cancer xenografts. *Biomaterials* 32:5872-5879.
37. Pasquale, E. B., N. K. Noren, M. Lu, A. L. Freeman, and M. Koolpe. 2004. Interplay between EphB4 on tumor cells and vascular ephrin-B2 regulates tumor growth. *P Natl Acad Sci USA* 101:5583-5588.

38. Xia, G., S. R. Kumar, R. Masood, S. Zhu, R. Reddy, V. Krasnoperov, D. I. Quinn, S. M. Henshall, R. L. Sutherland, J. K. Pinski, S. Daneshmand, M. Buscarini, J. P. Stein, C. Zhong, D. Broek, P. Roy-Burman, and P. S. Gill. 2005. EphB4 expression and biological significance in prostate cancer. *Cancer Res* 65:4623-4632.
39. Lee, Y. C., J. R. Perren, E. L. Douglas, M. P. Raynor, M. A. Bartley, P. G. Bardy, and S. A. Stephenson. 2005. Investigation of the expression of the EphB4 receptor tyrosine kinase in prostate carcinoma. *Bmc Cancer* 5:119.
40. Stephenson, S. A., S. Slomka, E. L. Douglas, P. J. Hewett, and J. E. Hardingham. 2001. Receptor protein tyrosine kinase EphB4 is up-regulated in colon cancer. *BMC Mol Biol* 2:15.
41. Vajkoczy, P., R. Erber, U. Eichelsbacher, V. Powajbo, T. Korn, V. Djonov, J. H. Lin, H. P. Hammes, R. Grobholz, and A. Ullrich. 2006. EphB4 controls blood vascular morphogenesis during postnatal angiogenesis. *Embo J* 25:628-641.
42. Bakker, W. H., E. P. Krenning, J. C. Reubi, W. A. Breeman, B. Setyono-Han, M. de Jong, P. P. Kooij, C. Bruns, P. M. van Hagen, P. Marbach. 1991. In vivo application of [<sup>111</sup>In-DTPA-D-Phe1]-octreotide for detection of somatostatin receptor-positive tumors in rats. *Life Sci* 49:1593-1601.
43. Hammond, P. J., A. F. Wade, M. E. Gwilliam, A. M. Peters, M. J. Myers, S. G. Gilbey, S. R. Bloom, and J. Calam. 1993. Amino acid infusion blocks renal tubular uptake of an indium-labelled somatostatin analogue. *Br J Cancer* 67:1437-1439.

44. Haubner, R., and C. Decristoforo. 2009. Radiolabelled RGD peptides and peptidomimetics for tumour targeting. *Front Biosci* 14:872-886.
45. Hargreaves, R. 2002. Imaging substance P receptors (NK1) in the living human brain using positron emission tomography. *J Clin Psychiatry* 63 Suppl 11:18-24.
46. Chen, J., Z. Cheng, T. J. Hoffman, S. S. Jurisson, and T. P. Quinn. 2000. Melanoma-targeting properties of (99m)technetium-labeled cyclic alpha-melanocyte-stimulating hormone peptide analogues. *Cancer Res* 60:5649-5658.
47. Blower, P. J., M. R. Puncher, A. G. Kettle, S. George, S. Dorsch, A. Leak, L. H. Naylor, and M. J. O'Doherty. 1998. Iodine-123 salmon calcitonin, an imaging agent for calcitonin receptors: synthesis, biodistribution, metabolism and dosimetry in humans. *Eur J Nucl Med* 25:101-108.
48. Liu, Y., D. Abendschein, G. E. Woodard, R. Rossin, K. McCommis, J. Zheng, M. J. Welch, and P. K. Woodard. 2010. Molecular imaging of atherosclerotic plaque with (64)Cu-labeled natriuretic peptide and PET. *J Nucl Med* 51:85-91.
49. Schottelius, M., and H. J. Wester. 2009. Molecular imaging targeting peptide receptors. *Methods* 48:161-177.
50. Koolpe, M., R. Burgess, M. Dail, and E. B. Pasquale. 2005. EphB receptor-binding peptides identified by phage display enable design of an antagonist with ephrin-like affinity. *J Biol Chem* 280:17301-17311.
51. Wester, H. J. 2007. Nuclear imaging probes: from bench to bedside. *Clin Cancer Res* 13:3470-3481.
52. Blankenberg, F. G., and H. W. Strauss. 2002. Nuclear medicine applications in molecular imaging. *J Magn Reson Imaging* 16:352-361.

53. Blankenberg, F. G., and H. W. Strauss. 2007. Nuclear medicine applications in molecular imaging: 2007 update. *Q J Nucl Med Mol Imaging* 51:99-110.
54. Weissleder, R., and U. Mahmood. 2001. Molecular imaging. *Radiology* 219:316-333.
55. Wang, W., S. Ke, S. Kwon, S. Yallampalli, A. G. Cameron, K. E. Adams, M. E. Mawad, and E. M. Sevick-Muraca. 2007. A new optical and nuclear dual-labeled imaging agent targeting interleukin 11 receptor alpha-chain. *Bioconjug Chem* 18:397-402.
56. Weissleder, R., and V. Ntziachristos. 2003. Shedding light onto live molecular targets. *Nat Med* 9:123-128.
57. Dzik-Jurasz, A. S. 2003. Molecular imaging in vivo: an introduction. *Br J Radiol* 76 Spec No 2:S98-109.
58. Grinvald, A., R. D. Frostig, E. Lieke, and R. Hildesheim. 1988. Optical imaging of neuronal activity. *Physiol Rev* 68:1285-1366.
59. Gibson, A. P., J. C. Hebden, and S. R. Arridge. 2005. Recent advances in diffuse optical imaging. *Phys Med Biol* 50:R1-43.
60. Bremer, C., V. Ntziachristos, and R. Weissleder. 2003. Optical-based molecular imaging: contrast agents and potential medical applications. *Eur Radiol* 13:231-243.
61. Hielscher, A. H. 2005. Optical tomographic imaging of small animals. *Curr Opin Biotechnol* 16:79-88.
62. Licha, K., and C. Olbrich. 2005. Optical imaging in drug discovery and diagnostic applications. *Adv Drug Deliv Rev* 57:1087-1108.

63. Niell, C. M., and S. J. Smith. 2004. Live optical imaging of nervous system development. *Annu Rev Physiol* 66:771-798.
64. Luker, G. D., and K. E. Luker. 2008. Optical imaging: current applications and future directions. *J Nucl Med* 49:1-4.
65. Cerussi, A., D. Hsiang, N. Shah, R. Mehta, A. Durkin, J. Butler, and B. J. Tromberg. 2007. Predicting response to breast cancer neoadjuvant chemotherapy using diffuse optical spectroscopy. *Proc Natl Acad Sci U S A* 104:4014-4019.
66. Rao, J., A. Dragulescu-Andrasi, and H. Yao. 2007. Fluorescence imaging in vivo: recent advances. *Curr Opin Biotechnol* 18:17-25.
67. Frangioni, J. V. 2003. In vivo near-infrared fluorescence imaging. *Curr Opin Chem Biol* 7:626-634.
68. Ntziachristos, V., C. Bremer, and R. Weissleder. 2003. Fluorescence imaging with near-infrared light: new technological advances that enable in vivo molecular imaging. *Eur Radiol* 13:195-208.
69. Reich, G. 2005. Near-infrared spectroscopy and imaging: basic principles and pharmaceutical applications. *Adv Drug Deliv Rev* 57:1109-1143.
70. Mahmood, U., and R. Weissleder. 2003. Near-infrared optical imaging of proteases in cancer. *Mol Cancer Ther* 2:489-496.
71. Massoud, T. F., and S. S. Gambhir. 2003. Molecular imaging in living subjects: seeing fundamental biological processes in a new light. *Genes & Development* 17:545-580.
72. Louie, A. Multimodality imaging probes: design and challenges. *Chem Rev* 110:3146-3195.



73. Melancon, M. P., W. Lu, Z. Yang, R. Zhang, Z. Cheng, A. M. Elliot, J. Stafford, T. Olson, J. Z. Zhang, and C. Li. 2008. In vitro and in vivo targeting of hollow gold nanoshells directed at epidermal growth factor receptor for photothermal ablation therapy. *Mol Cancer Ther* 7:1730-1739.
74. Schwartzberg, A. M., T. Y. Olson, C. E. Talley, and J. Z. Zhang. 2006. Synthesis, characterization, and tunable optical properties of hollow gold nanospheres. *J Phys Chem B* 110:19935-19944.
75. Liang, H. P., L. J. Wan, C. L. Bai, and L. Jiang. 2005. Gold hollow nanospheres: tunable surface plasmon resonance controlled by interior-cavity sizes. *J Phys Chem B* 109:7795-7800.
76. Vogel, A., and V. Venugopalan. 2003. Mechanisms of pulsed laser ablation of biological tissues. *Chem Rev* 103:577-644.
77. Amin, Z., J. J. Donald, A. Masters, R. Kant, A. C. Steger, S. G. Bown, and W. R. Lees. 1993. Hepatic metastases: interstitial laser photocoagulation with real-time US monitoring and dynamic CT evaluation of treatment. *Radiology* 187:339-347.
78. Fiedler, V. U., H. J. Schwarzmaier, F. Eickmeyer, F. P. Muller, C. Schoepp, and P. R. Verreet. 2001. Laser-induced interstitial thermotherapy of liver metastases in an interventional 0.5 Tesla MRI system: technique and first clinical experiences. *J Magn Reson Imaging* 13:729-737.
79. Nolsoe, C. P., S. Torp-Pedersen, F. Burcharth, T. Horn, S. Pedersen, N. E. Christensen, E. S. Olldag, P. H. Andersen, S. Karstrup, T. Lorentzen. 1993. Interstitial hyperthermia of colorectal liver metastases with a US-guided Nd-YAG laser with a diffuser tip: a pilot clinical study. *Radiology* 187:333-337.

80. Au, L., D. Zheng, F. Zhou, Z. Y. Li, X. Li, and Y. Xia. 2008. A quantitative study on the photothermal effect of immuno gold nanocages targeted to breast cancer cells. *ACS Nano* 2:1645-1652.
81. Chen, J., D. Wang, J. Xi, L. Au, A. Siekkinen, A. Warsen, Z. Y. Li, H. Zhang, Y. Xia, and X. Li. 2007. Immuno gold nanocages with tailored optical properties for targeted photothermal destruction of cancer cells. *Nano Lett* 7:1318-1322.
82. Dickerson, E. B., E. C. Dreaden, X. Huang, I. H. El-Sayed, H. Chu, S. Pushpanketh, J. F. McDonald, and M. A. El-Sayed. 2008. Gold nanorod assisted near-infrared plasmonic photothermal therapy (PPTT) of squamous cell carcinoma in mice. *Cancer Lett* 269:57-66.
83. Hirsch, L. R., R. J. Stafford, J. A. Bankson, S. R. Sershen, B. Rivera, R. E. Price, J. D. Hazle, N. J. Halas, and J. L. West. 2003. Nanoshell-mediated near-infrared thermal therapy of tumors under magnetic resonance guidance. *Proc Natl Acad Sci U S A* 100:13549-13554.
84. Loo, C., A. Lowery, N. Halas, J. West, and R. Drezek. 2005. Immunotargeted nanoshells for integrated cancer imaging and therapy. *Nano Lett* 5:709-711.
85. Lu, W., C. Xiong, G. Zhang, Q. Huang, R. Zhang, J. Z. Zhang, and C. Li. 2009. Targeted photothermal ablation of murine melanomas with melanocyte-stimulating hormone analog-conjugated hollow gold nanospheres. *Clin Cancer Res* 15:876-886.
86. Park, J. H., G. von Maltzahn, M. J. Xu, V. Fogal, V. R. Kotamraju, E. Ruoslahti, S. N. Bhatia, and M. J. Sailor. 2009. Cooperative nanomaterial system to sensitize, target, and treat tumors. *Proc Natl Acad Sci U S A* 107:981-986.

87. Park, J. H., G. von Maltzahn, M. J. Xu, V. Fogal, V. R. Kotamraju, E. Ruoslahti, S. N. Bhatia, and M. J. Sailor. 2010. Cooperative nanomaterial system to sensitize, target, and treat tumors. *Proc Natl Acad Sci U S A* 107:981-986.
88. Lowery, A. R., A. M. Gobin, E. S. Day, N. J. Halas, and J. L. West. 2006. Immunonanoshells for targeted photothermal ablation of tumor cells. *Int J Nanomedicine* 1:149-154.
89. Bernardi, R. J., A. R. Lowery, P. A. Thompson, S. M. Blaney, and J. L. West. 2008. Immunonanoshells for targeted photothermal ablation in medulloblastoma and glioma: an in vitro evaluation using human cell lines. *J Neurooncol* 86:165-172.
90. Xiong, C., M. Huang, R. Zhang, S. Song, W. Lu, L. Flores, 2nd, J. Gelovani, and C. Li. In vivo small-animal PET/CT of EphB4 receptors using <sup>64</sup>Cu-labeled peptide. *J Nucl Med* 52:241-248.
91. Zhang, R., C. Xiong, M. Huang, M. Zhou, Q. Huang, X. Wen, D. Liang, and C. Li. Peptide-conjugated polymeric micellar nanoparticles for Dual SPECT and optical imaging of EphB4 receptors in prostate cancer xenografts. *Biomaterials* 32:5872-5879.
92. Cooper, M. A. 2002. Optical biosensors in drug discovery. *Nature Reviews Drug Discovery* 1:515.
93. Pasquale, E. B., and N. K. Noren. 2007. Paradoxes of the EphB4 receptor in cancer. *Cancer Research* 67:3994-3997.
94. Kuhn, P., J. E. Chrencik, A. Brooun, M. I. Recht, M. L. Kraus, M. Koolpe, A. R. Kolatkar, R. H. Bruce, G. Martiny-Baron, H. Widmer, and E. B. Pasquale. 2006.

- Structure and thermodynamic characterization of the EphB4/ephrin-B2 antagonist peptide complex reveals the determinants for receptor specificity. *Structure* 14:321-330.
95. Ellis, L. M., W. B. Liu, S. A. Ahmad, Y. D. Jung, N. Reinmuth, F. Fan, and C. D. Bucana. 2002. Coexpression of ephrin-Bs and their receptors in colon carcinoma. *Cancer* 94:934-939.
  96. Takakura, N., X. Huang, Y. Yamada, H. Kidoya, H. Naito, Y. Nagahama, L. Kong, S. Y. Katoh, W. F. Li, and M. Ueno. 2007. EphB4 overexpression in B16 melanoma cells affects arterial-venous patterning in tumor angiogenesis. *Cancer Research* 67:9800-9808.
  97. Jain, R. K. 1998. Delivery of molecular and cellular medicine to solid tumors. *J Control Release* 53:49-67.
  98. Hong, S. Y., J. E. Oh, and K. H. Lee. 1999. Effect of D-amino acid substitution on the stability, the secondary structure, and the activity of membrane-active peptide. *Biochem Pharmacol* 58:1775-1780.
  99. Yamasaki, M., K. Shibata, T. Suzawa, S. Soga, T. Mizukami, K. Yamada, and N. Hanai. 2003. Improvement of biological activity and proteolytic stability of peptides by coupling with a cyclic peptide. *Bioorg Med Chem Lett* 13:2583-2586.
  100. Rusckowski, M., T. Qu, S. Gupta, A. Ley, and D. J. Hnatowich. 2001. A comparison in monkeys of (<sup>99m</sup>Tc) labeled to a peptide by 4 methods. *J Nucl Med* 42:1870-1877.

101. Tsai, S. W., L. Li, L. E. Williams, A. L. Anderson, A. A. Raubitschek, and J. E. Shively. 2001. Metabolism and renal clearance of <sup>111</sup>In-labeled DOTA-conjugated antibody fragments. *Bioconjug Chem* 12:264-270.
102. DePinho, R. A., F. B. Furnari, T. Fenton, R. M. Bachoo, A. Mukasa, J. M. Stommel, A. Stegh, W. C. Hahn, K. L. Ligon, D. N. Louis, C. Brennan, L. Chin, and W. K. Cavenee. 2007. Malignant astrocytic glioma: genetics, biology, and paths to treatment. *Gene Dev* 21:2683-2710.
103. Wen, P. Y., and S. Kesari. 2008. Malignant gliomas in adults. *New Engl J Med* 359:492-507.
104. Hsu, A. R., W. Cai, A. Veeravagu, K. A. Mohamedali, K. Chen, S. Kim, H. Vogel, L. C. Hou, V. Tse, M. G. Rosenblum, and X. Chen. 2007. Multimodality molecular imaging of glioblastoma growth inhibition with vasculature-targeting fusion toxin VEGF121/rGel. *J Nucl Med* 48:445-454.
105. Hsu, A. R., L. C. Hou, A. Veeravagu, J. M. Greve, H. Vogel, V. Tse, and X. Chen. 2006. In vivo near-infrared fluorescence imaging of integrin  $\alpha v \beta 3$  in an orthotopic glioblastoma model. *Mol Imaging Biol* 8:315-323.
106. McCann, C. M., P. Waterman, J. L. Figueiredo, E. Aikawa, R. Weissleder, and J. W. Chen. 2009. Combined magnetic resonance and fluorescence imaging of the living mouse brain reveals glioma response to chemotherapy. *Neuroimage* 45:360-369.
107. Adams, K. E., S. Ke, S. Kwon, F. Liang, Z. Fan, Y. Lu, K. Hirschi, M. E. Mawad, M. A. Barry, and E. M. Sevick-Muraca. 2007. Comparison of visible and near-

- infrared wavelength-excitabile fluorescent dyes for molecular imaging of cancer. *J Biomed Opt* 12:024017.
108. Barker, F. G., 2nd, and S. M. Chang. 2006. Improving resection of malignant glioma. *Lancet Oncol* 7:359-360.
  109. Laws, E. R., I. F. Parney, W. Huang, F. Anderson, A. M. Morris, A. Asher, K. O. Lillehei, M. Bernstein, H. Brem, A. Sloan, M. S. Berger, and S. Chang. 2003. Survival following surgery and prognostic factors for recently diagnosed malignant glioma: data from the Glioma Outcomes Project. *J Neurosurg* 99:467-473.
  110. Stummer, W., U. Pichlmeier, T. Meinel, O. D. Wiestler, F. Zanella, and H. J. Reulen. 2006. Fluorescence-guided surgery with 5-aminolevulinic acid for resection of malignant glioma: a randomised controlled multicentre phase III trial. *Lancet Oncol* 7:392-401.
  111. Yang, Z., S. Zheng, W. J. Harrison, J. Harder, X. Wen, J. G. Gelovani, A. Qiao, and C. Li. 2007. Long-circulating near-infrared fluorescence core-cross-linked polymeric micelles: synthesis, characterization, and dual nuclear/optical imaging. *Biomacromolecules* 8:3422-3428.
  112. Maeda, H. 2001. The enhanced permeability and retention (EPR) effect in tumor vasculature: the key role of tumor-selective macromolecular drug targeting. *Adv Enzyme Regul* 41:189-207.
  113. Matsumura, Y., and H. Maeda. 1986. A new concept for macromolecular therapeutics in cancer chemotherapy: mechanism of tumoritropic accumulation of proteins and the antitumor agent smancs. *Cancer Res* 46:6387-6392.

114. Poon, R. T., and N. Borys. 2009. Lyso-thermosensitive liposomal doxorubicin: a novel approach to enhance efficacy of thermal ablation of liver cancer. *Expert Opin Pharmacother* 10:333-343.
115. Vasey, P. A., S. B. Kaye, R. Morrison, C. Twelves, P. Wilson, R. Duncan, A. H. Thomson, L. S. Murray, T. E. Hilditch, T. Murray, S. Burtles, D. Fraier, E. Frigerio, and J. Cassidy. 1999. Phase I clinical and pharmacokinetic study of PK1 [N-(2-hydroxypropyl)methacrylamide copolymer doxorubicin]: first member of a new class of chemotherapeutic agents-drug-polymer conjugates. Cancer Research Campaign Phase I/II Committee. *Clin Cancer Res* 5:83-94.
116. DeNardo, S. J., Z. S. Yao, K. S. Lam, A. M. Song, P. A. Burke, G. R. Mirick, K. R. Lamborn, R. T. O'Donnell, and G. L. DeNardo. 2003. Effect of molecular size of pegylated peptide on the pharmacokinetics and tumor targeting in lymphoma-bearing mice. *Clinical Cancer Research* 9:3854s-3864s.
117. DeNardo, S. J., Z. Yao, G. L. DeNardo, A. Song, D. L. Kukis, G. R. Mirick, K. R. Lamborn, R. T. O'Donnell, and K. S. Lam. 2002. Effect of molecular size of pegylated peptide on the pharmacokinetics and tumor targeting in lymphoma bearing mice. *Journal of Nuclear Medicine* 43:93p-93p.
118. Song, S., C. Xiong, M. Zhou, W. Lu, Q. Huang, G. Ku, J. Zhao, L. G. Flores, Jr., Y. Ni, and C. Li. 2011. Small-animal PET of tumor damage induced by photothermal ablation with <sup>64</sup>Cu-bis-DOTA-hypericin. *J Nucl Med* 52:792-799.

## **VITA**

Miao Huang was born at Suzhou, China on May 15th, 1976, the son of Zhicai Huang and Ji Hu. After completing his high school at the Suzhou High School, JiangSu, China in 1994, he entered Suzhou Medical College in Suzhou, China. He received the degree of Bachelor of Medicine with a major in clinical medicine from Suzhou medical college in July, 1999. In September 2004, he entered Dr. Feng Wang-Johanning's lab to study and received the degree of Master of Science with a major in Cancer Biology from University of Texas health Science Center at Houston in July, 2006. Then he admitted into Ph.D program in the same school (Advisor, Chun Li, Ph.D.).

Permanent address:

zhong Jun xin cun building 14, Apt 205

Suzhou

JiangSu, China, 215000.